Double Differential Neutron Yields Produced by Proton, Helium, and Iron Interactions in Thick Aluminum Targets

A Dissertation Presented for the
Doctor of Philosophy
Degree
The University of Tennessee, Knoxville

Natalie Ann McGirl
December 2017

Copyright © 2017 by Natalie Ann McGirl
All rights reserved.

To my family, for their unconditional support and encouragement throughout my eight and a half years at the University of Tennessee. Mom, Dad, Lindsey, and Nick, I couldn't have done it without you.

To Luis. I couldn't ask for a better partner.

ACKNOWLEDGEMENTS

I'd first like to acknowledge the support provided by the University of Tennessee through a Chancellor's Fellowship award. I never thought I'd be an official Volunteer for so long, but I'm sincerely grateful for the opportunity. This work was also supported by NASA grants NNX12AL51A, NNX15AD89A, and NNX17AI10A.

Next, I would like to express my sincere gratitude to Dr. Lawrence Heilbronn for serving as my advisor for the past five years. Dr. Heilbronn has played an integral role in both my academic and professional development, and he is a thoughtful and irreplaceable mentor. I can't thank him enough for his support and advice. I would also like to thank the members of my graduate committee, Dr. Lawrence Townsend, Dr. Jason Hayward, and Dr. Kate Jones from the University of Tennessee, and Dr. Martha Clowdsley from NASA Langley Research Center. I appreciate your insightful feedback on this dissertation and your patience and advice throughout my academic career.

Huge thanks to Hui-Chen Wang and Luis Castellanos for allowing me to use their PHITS and MCNP simulations, and for their assistance. Thanks to Dr. Tony Slaba for running my PHITS simulations on the NASA Langley cluster. Additional thanks to Dr. Matthew Beach for answering countless emails about ROOT and its annoying quirks. Special thanks to Ashwin Srikrishna for sitting through endless practice presentations and paper reviews over the years, and for laughing at my stupid jokes.

Finally, special thanks to the other members of this research collaboration. Dr. Michael Sivertz, Dr. Adam Rusek, and Rory Rosselot from Brookhaven National Laboratory; Dr. Chiara La Tessa from the University of Trento, Italy; Dr. Cary Zeitlin from Leidos; Dr. Steve Blattnig, Dr. John Norbury, Dr. Ryan Norman, Dr. Charlie Werneth, and David Moore from NASA Langley Research Center; and Hunter Ratliff from the University of Tennessee. I appreciate your assistance and friendship over the past few years and it was a pleasure working with all of you. Shout out to those who brought food to the break room during the experiments.

ABSTRACT

Recent calculations of galactic cosmic ray (GCR) transport in enclosed, shielded space environments indicate that a minimum dose equivalent is achieved with aluminum shielding thicknesses near 20 g/cm^2 [grams per centimeter squared]. Increases in the absorbed dose and dose equivalent with shielding thicknesses above 20 g/cm^2 are believed to be caused by the production of light ions and neutrons in the thick shielding. However, uncertainties surround these calculations due to limited cross section and yield data for high-energy projectiles incident on thick targets. Thick-target neutron yields are particularly valuable measurements since they are produced over a wide range of energies by primary and secondary particles and include neutrons modified by transport through a material. Thus, a database of thick-target neutron yield measurements will help validate transport code calculations and quantify uncertainties between experimental and simulated data.

In March 2016, secondary neutron yields from GCR-like projectiles impinging upon thick targets were measured at Brookhaven National Laboratory's NASA Space Radiation Laboratory. 400 and 800 AMeV [megaelectron volt per nucleon] iron and proton, and 400 AMeV helium projectiles were set incident upon 20, 40, and 60 g/cm^2-thick aluminum targets, and a second 60 g/cm^2 aluminum target was centered downstream to study backscattered neutrons at a later date. Upstream target neutron yields were measured with liquid scintillators at 10° [degrees], 30°, 45°, 60°, 80°, and 135° off the beam axis using the time-of-flight technique. Measurements were converted to double differential thick-target yields and compared with PHITS and MCNP transport model calculations.

Comparisons with PHITS and MCNP revealed inconsistencies at low to intermediate energies, in addition to overestimations of the experimental yields at the 10° high-energy peak. Wide-angle yields at the shoulder energies were fairly well modeled for most systems, and yields at 135° were underestimated for the 400 AMeV projectile beams. Overall, both codes would benefit from improvements in their neutron production models, particularly below the peak or shoulder energies. This systematic study on secondary neutrons produced by thick-target interactions will

be incorporated by NASA into a rigorous uncertainty quantification procedure, which will ultimately help determine optimal shielding thicknesses for future space applications.

TABLE OF CONTENTS

I. Introduction 1
I.1 Dissertation Overview 1
I.2 Original Contribution 2
I.3 Dissertation Goals 2
I.4 Outline 3

II. General Information 4
II.1 Space Environment 4
II.2 Creation of Secondary Radiation Field 6
II.2.1 Overview 6
II.2.2 GCR-Target Atomic Interactions 6
II.2.3 GCR-Target Nuclear Interactions 7
II.2.4 Neutron Yields as a Function of Energy 8
II.2.5 Neutron Interaction Mechanisms 9
II.2.6 Neutron Importance in Secondary Radiation Fields 10
II.3 Transport Models 10
II.4 Secondary Radiation Fields Behind a Single Shield 12
II.5 Influence of a Second Shield 13
II.6 Thick GCR Shielding Project 14

III. Literature Review 18
III.1 Existing Double Differential Thick-Target Neutron Yield Measurements 18

IV. Experimental Setup and Analysis Techniques 21
IV.1 Experimental Setup 21
IV.1.1 Overview 21
IV.1.2 Projectile Beams 21
IV.1.3 Targets 23
IV.1.4 Start Scintillators 25
IV.1.5 Veto Detectors 25
IV.1.6 Liquid Scintillators 27
IV.1.7 Shadow Bar System 29
IV.2 Electronic Equipment and Data Acquisition 30
IV.2.1 Trigger Logic 30
IV.2.2 TDC and QDC Data Acquisition 34
IV.2.3 Issues with the Acquisition Trigger 35
IV.2.4 QDC Calibration 35
IV.2.5 TDC Calibration 37
IV.3 Data Filtering 39
IV.3.1 Overview 39
IV.3.2 Good Beam Gate 39
IV.3.3 Self-Time Gate 41
IV.3.4 Neutral and Charged Particle Separation 42
IV.3.5 Neutron – Gamma Discrimination 43
IV.3.6 Pulse Height Gate 47
IV.4 Source Particle Adjustment 47
IV.5 Background Subtraction 48
IV.6 Prompt Gamma Peak Identification 48

IV.7 Time-of-Flight Calculation....48
IV.8 Correction Factors....51
IV.8.1 Efficiency Correction....51
IV.8.2 Solid Angle and Energy Bin Width Corrections....53
IV.9 Monte Carlo Simulations....53
IV.9.1 PHITS Overview....53
IV.9.2 Design of PHITS Benchmarking Simulations....55
IV.9.3 MCNP Overview....56
IV.9.4 Design of MCNP Benchmarking Simulations....58
V. Results and Discussion....61
V.1 Prompt Gamma Peak Identification....61
V.2 Uncertainty Calculations for Experimentally Calculated Yields....66
V.2.1 Statistical Uncertainties....66
V.2.2 Systematic Uncertainties....69
V.2.3 Energy Resolution....70
V.2.4 High-Energy Correction Factor....73
V.3 Experimental and Simulated Double Differential Thick-Target Neutron Yields....80
V.3.1 Experimental DDTT Yield Spectra....80
V.3.2 Comparison with PHITS and MCNP Simulations....85
V.3.3 Angular Distribution of DDTT Neutron Yields....89
VI. Conclusions And Future Work....95
References....97
Appendices....104
Appendix I....105
Appendix II....108
Appendix III....121
Vita....134

LIST OF TABLES

Table 1. Projectile-target matrix for "Thick GCR Shielding Project." Blue, green, and gray boxes indicate data collected in Mar. 2016, Nov./Dec. 2016, and Nov./Dec. 2017, respectively. 15
Table 2. Existing measurements of proton-induced thick-target neutron yields. 19
Table 3. Existing measurements of helium-induced thick-target neutron yields..... 19
Table 4. Existing measurements of heavy-ion (2<Z<28)-induced thick-target neutron yields. 20
Table 5. Incident beams that stopped (Y) or did not stop (N) in the 20, 40, and 60 g/cm^2 upstream or the 60 g/cm^2 downstream aluminum targets..... 24
Table 6. Operating voltages and flight paths for liquid scintillators..... 28
Table 7. TDC calibration for liquid scintillators..... 38
Table 8. Lowest resolvable neutron energy with PSD in liquid scintillators..... 46
Table 9. Prompt gamma peak centroids and FWHMs for all beams on 20 g/cm^2 aluminum target. 64
Table 10. Prompt gamma peak centroids and FWHMs for all beams on 40 g/cm^2 aluminum target. 65
Table 11. Prompt gamma peak centroids and FWHMs for all beams on 60 g/cm^2 aluminum target. 65
Table 12. Systematic uncertainties for liquid scintillators..... 69
Table 13. Timing resolutions and fractional flight path resolutions for liquid scintillators.72
Table 14. List of logic unit manufacturer and applicable settings..... 106
Table 15. Button source information from BNL. 106
Table 16. Adjusted flight paths for high-energy neutrons originating from 400 or 800 AMeV iron, or 400 AMeV helium beams incident on aluminum. 107

LIST OF FIGURES

Figure 1. Relative abundance of GCR (black) with a dose contribution estimate (white) [6]. 5
Figure 2. Selection of GCR energy spectra as observed near Earth. The solid line extrapolates the H spectrum to interstellar space after "unfolding the effects of solar modulation [9]." 5
Figure 3. Schematic of a peripheral abrasion-ablation reaction mechanism, adapted from [18]. Resulting momentum (*p*) shown for each stage. 8
Figure 4. Representative primary and secondary radiation fields for (a) single shield and (b) fully-enclosed shielded geometry. 13
Figure 5. Total dose equivalent for GCR on varying thicknesses of aluminum (left) and HDPE (right). Statistics show maximum Monte Carlo result minus the 3DHZETRN result, divided by the average of the values [35]. 14
Figure 6. BNL accelerator facilities schematic [43]. 17
Figure 7. NSRL target room schematic. Listed flight paths are from the center of the upstream target to the center of the detectors. 22
Figure 8. Experimental setup in NSRL target room. 22
Figure 9. 60 g/cm^2 upstream and downstream aluminum targets. 24
Figure 10. (a) BNL start scintillator tube with upstream aluminum target and (b) liquid scintillator array on custom cart. 26
Figure 11. 182 cm iron shadow bar, target room hallway. 29
Figure 12. Shadow bar alignment for liquid scintillators at 10° and 60°, configuration B.30
Figure 13. Electronic logic map. 31
Figure 14. Physics room with logic equipment at NSRL. 32
Figure 15. Coincidence between (OLS or CS) AND *s1.s2* setting the acquisition gate and trigger. 32
Figure 16. 30° OLS TDC spectra for all beam-target systems gated on all triggers, 30° OLS self-time, remaining five OLS self-times, and CS paddle self-times. 36
Figure 17. Gamma calibrations for liquid scintillators at operating voltages. 38
Figure 18. Charge deposited in S1 and S2 scintillators for 800 AMeV iron on all targets.40
Figure 19. Charge deposited in S1 and S2 scintillators for 400 MeV protons on all targets.40
Figure 20. Charge deposited in S1 and S2 scintillators for 400 AMeV helium on all targets. 41
Figure 21. Liquid scintillator self-time peaks and gate widths for an 800-AMeV iron beam on 20 g/cm^2 aluminum target, no shadow bars. 42
Figure 22. Front veto paddle QDC spectra with neutral particle pedestal cuts for an 800-AMeV iron beam on 20 g/cm^2 aluminum target, no shadow bars. 43
Figure 23. (a) Un-attenuated neutron and gamma PSD at 45° for 400 AMeV iron, pileup region excluded, in (b) the low energy separation region with (c) Y axis-projection of the neutron-gamma separation threshold at channel 84. Neutron and gamma peaks are fitted with Gaussian distributions and are well-separated at 2σ. 44
Figure 24. Attenuated neutron and gamma PSD at 45° for 400 AMeV iron gated on the pileup region of the un-attenuated signals. 46

Figure 25. Neutron and gamma TOF spectra at 135° for 400 AMeV iron on 60 g/cm^2 aluminum. Neutron events 3σ to the left of the prompt gamma peak centroid and above are eliminated in the TOF analysis. Time increases right to left. 50
Figure 26. SCINFUL-QMD computational process [90]. 52
Figure 27. Neutron detection efficiency as a function of energy for a 12.7 cm by 12.7 cm cylindrical liquid scintillator at 10° and 135°, with pulse height thresholds of 4 and 2 MeV, respectively. Listed flight paths are to front surface of active volume.... 54
Figure 28. PHITS physics models for different particle species and energy ranges [29]. 54
Figure 29. 3-dimensional representation of PHITS ring configuration with aluminum targets and six liquid scintillator rings [95]. 57
Figure 30. (a) Neutron time of flight versus energy for 800 AMeV iron projectiles incident on 20 g/cm^2 aluminum at 10°, (b) excluding all neutrons with k<0.97. Results calculated using MCNP. 1 shake is equivalent to 10 ns. 59
Figure 31. Un-shadowed and background-subtracted gamma TOF spectra for 400 AMeV iron beam on 20 g/cm^2 aluminum at 135°. 62
Figure 32. Possible source of smallest gamma peak observed at 135° with 400 AMeV iron projectile (beam profile monitor, 1), located between the beam exit window (off-camera, 2) and the start scintillators (3). 62
Figure 33. Un-shadowed and background-subtracted gamma TOF spectra for 800 AMeV iron beam on 20 g/cm^2 aluminum at 135°. 63
Figure 34. Un-shadowed and background-subtracted gamma TOF spectra for 400 MeV proton beam on 20 g/cm^2 aluminum at 10°. 64
Figure 35. FWHM linear fit for 800 AMeV iron on aluminum targets at 60°. 72
Figure 36. Fractional energy resolutions for 400 AMeV iron beam on 20 g/cm^2 aluminum at 10° and 135°. Listed flight paths are from upstream target center to scintillator active volume center. 74
Figure 37. Neutrons produced in 20, 40, and 60 g/cm^2 aluminum with 400 AMeV iron projectiles. 74
Figure 38. Neutrons produced in 20, 40, and 60 g/cm^2 aluminum with 800 AMeV iron projectiles. 75
Figure 39. Neutrons produced in 20, 40, and 60 g/cm^2 aluminum with 400 MeV proton projectiles. 75
Figure 40. Neutrons produced in 20, 40, and 60 g/cm^2 aluminum with 800 MeV proton projectiles. 76
Figure 41. Neutrons produced in 20, 40, and 60 g/cm^2 aluminum with 400 AMeV helium projectiles. 76
Figure 42. Flight path adjustment for high-energy neutrons schematic. 79
Figure 43. Pulse height stitching at 30º for 400 AMeV iron projectiles incident on 20 g/cm^2 aluminum. 84
Figure 44. Angular yield spectra for the 400 and 800 AMeV iron systems. 90
Figure 45. Angular yield spectra for the 400 and 800 MeV proton systems. 91
Figure 46. Angular yield spectra for the 400 AMeV helium systems. 92
Figure 47. DDTT neutron yields for 400 AMeV iron projectiles on aluminum; PHITS and MCNP room geometries. 110

Figure 48. DDTT neutron yields for 800 AMeV iron projectiles on aluminum; PHITS and MCNP room geometries. 111
Figure 49. DDTT neutron yields for 400 MeV proton projectiles on aluminum; PHITS and MCNP room geometries. 112
Figure 50. DDTT neutron yields for 800 MeV proton projectiles on aluminum; PHITS and MCNP room geometries. 113
Figure 51. DDTT neutron yields for 400 AMeV helium projectiles on aluminum; PHITS and MCNP room geometries. 114
Figure 52. DDTT neutron yields for 400 AMeV iron projectiles on aluminum; PHITS ring geometry and MCNP neutron directionality correction..... 116
Figure 53. DDTT neutron yields for 800 AMeV iron projectiles on aluminum; PHITS ring geometry and MCNP neutron directionality correction..... 117
Figure 54. DDTT neutron yields for 400 MeV proton projectiles on aluminum; PHITS ring geometry and MCNP neutron directionality correction..... 118
Figure 55. DDTT neutron yields for 800 MeV proton projectiles on aluminum; PHITS ring geometry and MCNP neutron directionality correction..... 119
Figure 56. DDTT neutron yields for 400 AMeV helium projectiles on aluminum; PHITS ring geometry and MCNP neutron directionality correction..... 120
Figure 57. DDTT neutron yields for 400 AMeV iron projectiles on aluminum; PHITS room and ring geometries..... 123
Figure 58. DDTT neutron yields for 800 AMeV iron projectiles on aluminum; PHITS room and ring geometries..... 124
Figure 59. DDTT neutron yields for 400 MeV proton projectiles on aluminum; PHITS room and ring geometries..... 125
Figure 60. DDTT neutron yields for 800 MeV proton projectiles on aluminum; PHITS room and ring geometries..... 126
Figure 61. DDTT neutron yields for 400 AMeV helium projectiles on aluminum; PHITS room and ring geometries..... 127
Figure 62. DDTT neutron yields for 400 AMeV iron projectiles on aluminum; MCNP room geometry and neutron directionality correction. 129
Figure 63. DDTT neutron yields for 800 AMeV iron projectiles on aluminum; MCNP room geometry and neutron directionality correction. 130
Figure 64. DDTT neutron yields for 400 MeV proton projectiles on aluminum; MCNP room geometry and neutron directionality correction. 131
Figure 65. DDTT neutron yields for 800 MeV proton projectiles on aluminum; MCNP room geometry and neutron directionality correction. 132
Figure 66. DDTT neutron yields for 400 AMeV helium projectiles on aluminum; MCNP room geometry and neutron directionality correction. 133

I. INTRODUCTION

I.1 Dissertation Overview

One of the major challenges that must be addressed before long-term space exploration missions are undertaken involves developing effective shielding strategies to protect astronauts from the harsh radiation environment. In space, astronauts are exposed to a large range of energetic neutral and charged particles. Because the full space radiation environment is impossible to replicate on Earth, a variety of computer codes are used to model the radiation environment and transport it through different shielding materials and thicknesses. This allows researchers to make informed decisions when it comes to spacecraft and habitat design. However, the accuracy and usefulness of these transport code results are reliant on the accuracy and availability of the data the codes are based on. To validate the transport code outputs, accelerator facility experiments are conducted to replicate a sampling of the projectile-target interactions that might occur in space. Thick-target neutron yields are particularly valuable measurements due to their significance in secondary radiation fields, in addition to the production and transport information that they contain.

The work presented in this dissertation includes a series of neutron measurements taken in March 2016 at Brookhaven National Laboratory's (BNL) NASA Space Radiation Laboratory (NSRL) during a joint BNL, NASA Langley Research Center (LaRC), and University of Tennessee, Knoxville (UTK) experiment. Double differential thick-target neutron yields at six angular locations were calculated from the experimental measurements using the time-of-flight technique. Results were then compared to a series of simulations executed with the Monte Carlo N-Particle Transport code (MCNP) and the Particle and Heavy Ion Transport Code System (PHITS). Eventually, the experimental double differential thick-target neutron yields will be incorporated in LaRC's rigorous uncertainty quantification procedure to validate the output of various radiation transport codes.

I.2 Original Contribution

Double differential thick-target neutron yields produced by 400 and 800 MeV/nucleon (AMeV) iron, 400 and 800 MeV proton, and 400 AMeV helium projectiles incident upon 20, 40, and 60 g/cm^2-thick aluminum targets have never been calculated before at forward and back angles between 10º and 135º off beam axis. Additionally, the placement of a second, 60 g/cm^2 downstream aluminum target in the beamline is a novel target arrangement not seen in the literature. Furthermore, the comparison between MCNP and PHITS simulations and the experimental data described here will advance the discussion on physics model assumptions and secondary neutron production in Monte Carlo and deterministic transport codes. A comparison between two geometry configurations in PHITS, and between two sets of results from a single MCNP simulation, will also provide insight into how low-energy neutron scattering affects thick-target yields, particularly at forward angles. Overall, this work serves as a benchmark dataset for comparison to a variety of radiation transport codes, which will ultimately help optimize future spacecraft and shielding designs for long-term missions to Mars.

I.3 Dissertation Goals

The overall goal of this dissertation is to generate a comprehensive double differential yield database for neutrons produced in GCR-like projectile and thick-target interactions, specifically for a dual-target geometry similar to what is observed in a spacecraft. The database will then be used by NASA LaRC to validate thick-target transport code outputs. In this work, the author will describe how to:

1. Convert liquid scintillator measurements for fifteen beam-target systems at various angles to double differential thick-target neutron yields using the time-of-flight technique.

2. Calculate all associated statistical and systematic uncertainties.

3. Replicate the experimental setup with PHITS and MCNP Monte Carlo benchmarking simulations. For PHITS, utilize two different geometry configurations to explore the yield contributions from neutrons produced by room scatter and the downstream target. Within

MCNP, use particle tracking techniques to include or exclude neutrons not produced in the upstream target.

4. Compare the experimental and simulated double differential thick-target neutron yields.

5. Calculate angular neutron yield distributions.

I.4 Outline

The remaining dissertation is arranged as follows:

- **Chapter II** provides general background information. The galactic cosmic ray (GCR) environment is described, along with the secondary radiation fields produced by GCR interactions with thick targets. This chapter also discusses transport modeling, the difference between single and dual-shield geometries, and the design of the overarching project this work is derived from.

- **Chapter III** lists all existing double differential neutron yields produced by proton through nickel interactions with thick, single targets.

- **Chapter IV** explores the experimental setup and data analysis techniques utilized in this work.

- **Chapter V** presents and discusses the experimental and Monte Carlo-simulated double differential thick-target neutron yields and their associated statistical and systematic uncertainties. Angular neutron yield distributions are also calculated and examined here.

- **Chapter VI** includes conclusions and future work.

II. GENERAL INFORMATION

II.1 Space Environment

The radiation environment experienced by astronauts is highly complex and dependent upon many factors including location in the heliosphere, timing in the solar cycle, and the amount or type of passive shielding. For humans participating in long-duration missions, exposures during the transit periods are of particular concern due to the relatively low level of shielding provided by the spacecraft when compared to the shielding provided by the bulk of the Moon or Mars during a surface operation [1], [2]. In free space, humans will experience both acute solar energetic particle (SEP) and chronic galactic cosmic ray (GCR) exposures. If acute exposures are high enough, astronauts may suffer from radiation sickness, while chronic exposures would have a latent effect such as an increased risk of exposure-induced death (REID) [3].

Transient SEP events originate from the Sun and consist of mostly protons that vary widely in energy and intensity. It is difficult to predict the strength and occurrence of SEP events, increasing an astronaut's risk of exposure [4]. While exceptions exist, SEP acute effects are usually mitigated by taking cover in shielding-fortified storm shelters [3]. Contrastingly, GCR's high energies make them difficult to fully shield, presenting unique challenges [4].

GCR originate from supernovae and reach the solar system isotropically with energies ranging from 10 AMeV to several ATeV [5]. Their hadron component (98%) is fully stripped of electrons and consists of protons (87%), alpha particles (12%), and heavy ions (1%), with the heavy ion component extending to nickel (Z=28) before a significant drop in fluence [5]. Despite the low abundance of heavy ions, they are significant GCR dose and dose equivalent contributors and must be taken into consideration when modeling the space environment (Figure 1) [6]. The remaining 2% of GCR include electrons and positrons [7]. Maximum GCR fluences occur in the 100 to 1000 AMeV region, depending upon the ion species and solar activity (Figure 2) [8], [9]. Free neutrons are not a component of GCR because they decay into a proton, electron, and antineutrino with a half-life of approximately 10.6 minutes [10]. However, they are produced upon GCR interactions with materials in space.

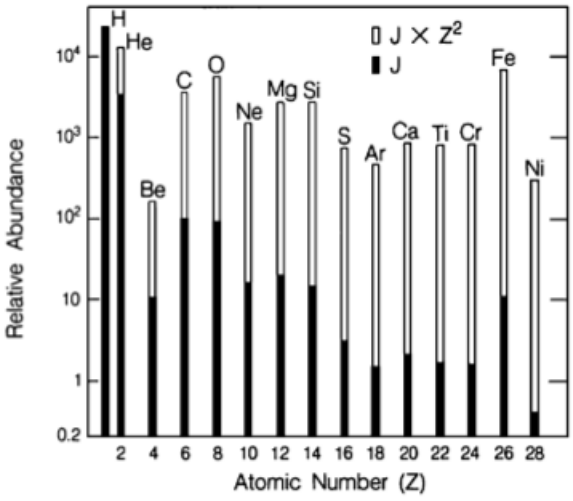


Figure 1. Relative abundance of GCR (black) with a dose contribution estimate (white) [6].

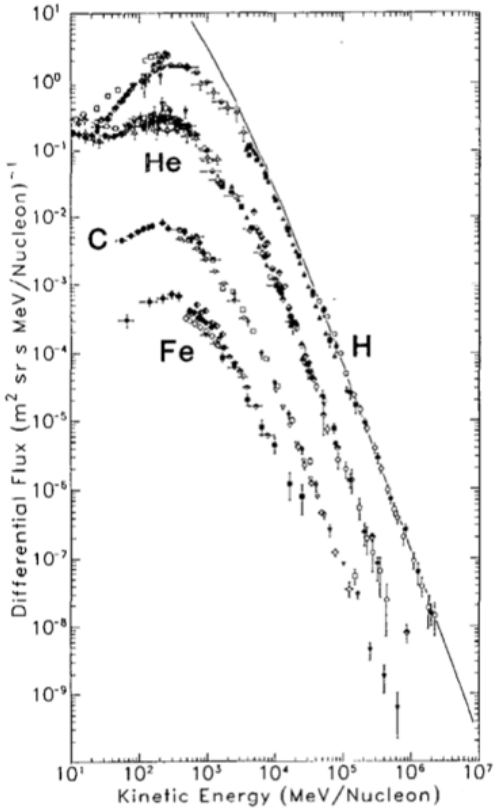


Figure 2. Selection of GCR energy spectra as observed near Earth. The solid line extrapolates the H spectrum to interstellar space after "unfolding the effects of solar modulation [9]."

II.2 Creation of Secondary Radiation Field

II.2.1 Overview

For recent spacecraft design, average shielding thicknesses vary from 10 g/cm^2 (space shuttle) to approximately 20 g/cm^2 (International Space Station [ISS] and Orion) [11]. However, thicker shielding regions (>20 g/cm^2) may exist within these vehicles and projectiles incident at wide angles will see more material than the transverse thickness [11]. When incident projectiles interact in thick shields, a variety of atomic and nuclear interactions may occur, creating a secondary radiation field. Knowledge of the secondary field's makeup is necessary to accurately calculate dose and dose equivalent in a shielded environment, but it can be difficult to determine [4]. Primary GCR may enter the shielding material and slow down or stop via atomic interactions. This process is considered well-understood and well-modeled. A GCR ion may also enter the shielding and undergo a fragmentation reaction, producing a variety of secondary particles that are dependent upon the projectile and target compositions. These neutral or charged fragments vary in mass and energy and may penetrate the thick shielding, while also producing additional particles [12]. GCR-target interactions are modeled using radiation transport codes which have a variety of associated uncertainties. Transport code validation and uncertainty quantification may be achieved by directly comparing simulation outputs to databases of experimental measurements.

II.2.2 GCR-Target Atomic Interactions

As described by Turner [10], atomic interactions are the primary mode of heavy charged particle energy loss. In these interactions, incident charged particles ionize or excite orbital electrons in the target material, losing energy continuously through small-angle, small-energy loss collisions. The free electrons may be decelerated by the electric field of a nucleus and create bremsstrahlung photons, or they may ionize or excite other orbital electrons. Additionally, the excited electrons may also release photons to de-excite. The energy loss of a heavy charged particle is described by the Bethe formula for stopping power (equation 1) [10], [13].

$$-\frac{\mathrm{dE}}{\mathrm{dx}} = 4\pi r_0^2 m_e c^2 \left(\frac{z^2}{\beta^2}\right) \cdot \frac{Z N_A \rho}{M_m} \cdot \left[\ln\left(\frac{2 m_e c^2 \beta^2}{I(1-\beta^2)}\right) - \beta^2 - \frac{\delta}{2} - \lambda\right] \quad (1)$$

Stopping power (dE/dx), or the linear energy transfer (LET), is a "measure of the average linear rate of energy loss of a heavy charged particle in a material [10]." Constants include the classical electron radius (r_0), the electron rest mass ($m_e c^2$), and Avogadro's number (N_A). β ($\beta = v_n / c$) and z refer to the speed of the incident projectile (v_n) relative to the speed of light (c) and the atomic number of the projectile. Z (number of electrons), ρ (density), M_m (molar mass), and I (mean excitation energy) are all properties of the target material. This formula demonstrates that as the energy of the incident projectile increases, the resulting stopping power decreases [10], [13]. As described by Anderson [13], the Bethe formula breaks down at low energies, when the charged projectile velocity approaches the orbital electron velocity, and at relativistic energies (~1 AGeV). The electronic shell correction (λ) reduces stopping power at low energies because tightly bound inner shell electrons are less likely to ionize, and because the interaction probability decreases between a projectile and orbital electron with similar velocities. Additionally, the density correction (δ) increases the stopping power at relativistic energies, accounting for the "flattening" of the electric field which reduces the screening effect for orbital electrons [13].

II.2.3 GCR-Target Nuclear Interactions

High-energy (>15 AMeV) GCR ions have a significant probability of undergoing nuclear fragmentation reactions, especially when traversing thick targets. In these reactions, a relativistic projectile nucleus (P) collides with a stationary target nucleus (T), releasing secondary particles with a range of charges, masses, and energies. In the abrasion-ablation model (Figure 3), the projectile travels along a straight-line trajectory with a pre-collision velocity and momentum (p_p), interacting with a stationary target [14]–[19]. During the abrasion stage, the projectile and target collide and the overlap volume shears off. The nucleons contained within the overlap region are called the participants, and their makeup is dependent upon the overlap volume [14]. Nucleons in this region may move away from the main region of interaction, collide with each other, or even coalesce to form larger mass particles. The remaining portions of the projectile and target are called the pre-fragments. The pre-fragment projectile continues along its path with almost the same momentum ($p_{PF,\,p}$), while the pre-fragment target recoils with momentum $p_{PF,\,t}$ [14]–[18].

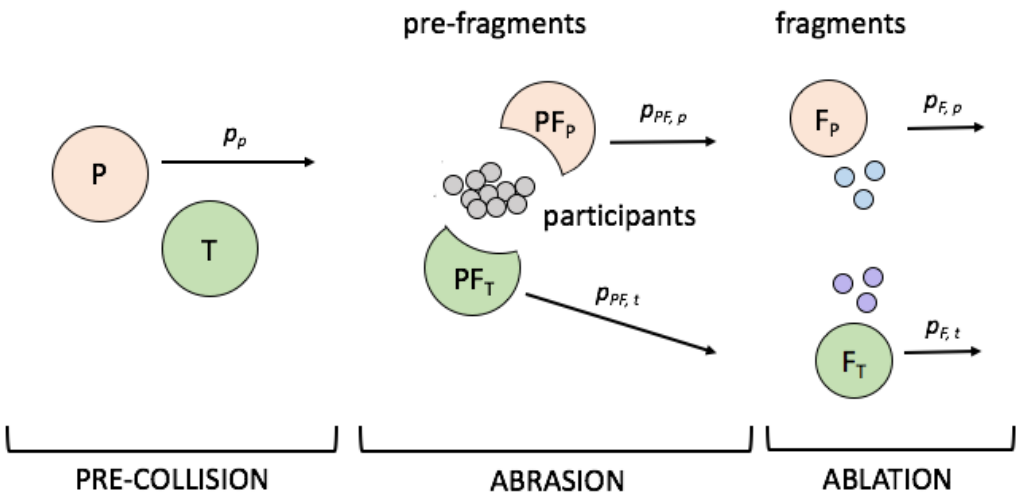


Figure 3. Schematic of a peripheral abrasion-ablation reaction mechanism, adapted from [18]. Resulting momentum (p) shown for each stage.

In the ablation stage, the highly-energetic and unstable pre-fragments decay by emitting nucleons and/or photons to form stable fragments. The number and makeup of the ablated particles is dependent upon the area of the sheared off region. The resulting fragments and ablated particles are the secondary particles produced during fragmentation [14]–[18]. Abrasion-ablation is over in 10^{-14} s [18]. In approximately 10% of fragmentation events, the projectile and target collide head-on. This nearly destroys the nuclei, releasing many high-energy secondary particles over a range of angles [16]. No projectile ablation occurs with this scenario because the nucleus is destroyed by abrasion [17]. In a peripheral event, the projectile and target volumes do not completely overlap, resulting in fewer secondary particles [16].

II.2.4 Neutron Yields as a Function of Energy

Neutrons are a prevalent secondary particle produced in fragmentation reactions and released over a wide range of angles. At all angles, neutrons below 20 MeV are emitted isotropically from the target spectator. As the neutron energy increases, the yields decrease exponentially. Intermediate energies and angles are populated by neutrons originating from evaporation and nucleon-nucleon collisions of the overlap participants [12], [20].

At the forward-most angles, neutrons form a broad plateau and peak at approximately 70% of the incident projectile energy (in AMeV). The broad peak is characteristic of thick targets because the projectile energy may range between nuclear reaction thresholds and the beam energy, depending upon the target thickness [21], [22]. Yields rapidly decrease as the neutron energies increase to up to two times the incident projectile energy. As the angle of detection increases, the forward-angle peak disappears and the spectra are characterized only by an exponential fall-off, which increases with angle [12], [20]. Secondary neutron contributions at forward angles may be formed by several different production methods. Forward angle neutron yields contain evaporation neutrons formed during the ablation of an excited pre-fragment or from the direct knock-out process [23], [24]. In the knock-out process, the individual projectile nucleons receive a momentum boost from their internal Fermi motion during a projectile-target interaction [21].

II.2.5 Neutron Interaction Mechanisms

Neutrons are neutral particles that only lose energy via nuclear interactions like absorption, inelastic scattering, or elastic scattering. In absorption reactions, a neutron is captured by a nucleus which leads to the ejection of other particles or energy. An example of a neutron capture reaction is $^{3}He(n, p)^{3}H$. In this reaction, a helium-3 ion captures a thermal neutron (0.025 eV), resulting in the release of a hydrogen-3 ion, a proton, and 765 keV of energy. In the case of fission, a fissile material captures a neutron, causing the isotope to break up into various fission fragments and release other neutrons and a large amount of energy. Uranium-235 and plutonium-239 are examples of fissile isotopes [10]. Additionally, inelastic scattering is often considered a neutron capture reaction with a neutron serving as the emitted secondary particle. Inelastic scattering interactions may be represented as $X(n, n')X^{*}$, where the resulting nucleus (X^{*}) is an excited, bound state of the original target nucleus (X). Photon emission accompanies secondary neutron expulsion [13].

As described by Turner [10], elastic scattering is a significant energy loss mode for high-energy neutrons. When a neutron scatters elastically off a target nucleus, the neutron loses energy but the total kinetic energy of the interaction is conserved. The energized target nucleus then recoils at an

angle and interacts with the target material. The maximum amount of energy (Q_{max}) that may be transferred from an incident neutron (mass m, kinetic energy E_n) to a target nucleus (mass M) in a single, head-on collision is given by equation 2 [10]. This equation shows that incident neutrons have the potential to lose a larger fraction of energy when striking lower-mass targets. Additionally, an incident neutron may lose all its energy in a single collision with a hydrogen target. This is known as neutron-proton (*n-p*) scattering. *N-p* scattering is the main pathway for fast neutron dose contributions in soft tissue because of the high hydrogen content. As a neutron loses energy in the target material through a series of elastic scattering events, the probability of an absorption reaction increases [10].

$$Q_{max} = \frac{4mME_n}{(m+M)^2} \tag{2}$$

II.2.6 Neutron Importance in Secondary Radiation Fields

When examining the radiation field produced by GCR-thick target interactions, secondary neutrons are a large concern because of their highly penetrative ability, relatively high abundance, and large dose equivalent conversion factors [25]. Since neutrons only lose energy via nuclear interactions, they often penetrate deeply into a material without undergoing any interaction. Additionally, neutrons are produced from a wide variety of projectile-target interactions [25]. As a result, they make up a large component of the secondary radiation field measured on the back side of a thick shield, and they are the second largest source of radiation damage and material activation in a target room outside of the incident beam [26], [22]. The dose equivalent conversion factors and thus the resulting neutron biological damage, are also high, depending upon the neutron energy [27].

II.3 Transport Models

As previously mentioned, the full space radiation environment is impractical to replicate on Earth, indicating that researchers need to utilize radiation transport codes when designing shielding for space applications. To model GCR-target interactions, the GCR environment is input into a

radiation transport code and set incident upon a geometry and material of interest. As the primary GCR field enters the target material, the codes predict the interaction point, interaction partner, reaction mechanism, and secondary particle yields and characteristics using total reaction cross sections from either a library of experimental measurements or predictive models [28]–[30]. Total reaction cross sections measure the relative probability of a nuclear interaction occurring between a given projectile and target [30]. Additionally, the codes model the transport processes undertaken by the primary and secondary particles before and after a collision, such as the ionization of the material by the moving charged particles. This cycle is repeated until all interactions are complete or the cutoff energies are reached [28], [29].

Despite their extensive use, transport code results are not always reliable or accurate due to limited cross section data. Additionally, the physics models utilized in transport codes may have large associated uncertainties, especially when modeling complex processes important to GCR transport like nuclear fragmentation [31]. These uncertainties propagate during transport and affect the accuracy of the final calculations. Transport uncertainties must be fully understood to accurately predict the biological effects of transported radiation on humans during long-term space exploration missions [31].

Often, comprehensive databases of cross section and yield measurements are helpful to validate transport code outputs [31]. With thick-target experiments, yields, not cross sections, are measured because the incident GCR or secondary particles have a high probability of multiple interactions in the target. While cross sections are an integral component of transport codes, yield measurements are also important because of the breadth of production information they contain. Thick-target neutron yields measure neutrons produced over a range of projectile energies up to the incident energy, while cross sections only measure neutrons produced by projectiles close to the incident energy [22]. Additionally, thick-target yields include neutrons modified by transport through the material or neutrons produced by secondary particles [32]. Thus, thick-target yields are important measurements needed to validate transport codes.

II.4 Secondary Radiation Fields Behind a Single Shield

Radiation transport through a single thick shield is a simple geometry often used to explore the creation of secondary radiation fields, like when designing an accelerator facility's shielding. For space radiation studies, primary GCR are incident upon thick slabs to simulate the shielding provided by one wall in a transit vehicle or habitat (Figure 4a). In some studies, the radiation environment is also transported through a layer of water to mimic the self-shielding effect of human tissue to calculate the total or organ dose equivalents [11]. Both values are a measurement of the biological damage inflicted by incident radiation. Total dose equivalent (equation 3) was found by multiplying the total absorbed dose (D) by a LET-dependent quality factor (Q). Similarly, the organ dose equivalents were found by multiplying the absorbed dose in specific organs of interest by the quality factor [10].

$$H_T = D \cdot Q(LET) \tag{3}$$

A series of GCR-induced dose equivalent calculations were conducted in [33] for a single slab of aluminum or high-density polyethylene (HDPE) with varying thicknesses. The results demonstrated that neutron and light ion (protons, deuterons, tritons, helium-3, and helium-4) contributions dominated the total dose equivalent when the target thicknesses were greater than 20 g/cm^2. This meant that the heavy ion component (Z>2) decreased with an increase in target thickness as they fragmented into lighter mass particles and lost energy due to atomic collisions [33]. Additional calculations by Walker *et al.* [34] were performed at realistic locations in the ISS, using the free space 1977 solar minimum GCR environment incident on thick (30 g/cm^2) aluminum shielding. 75 to 85% or more of the organ dose equivalents measured with thick shields were from neutrons and light ion contributions, compared to <50% with thin shields (1 or 5 g/cm^2). This study also demonstrated that secondary neutron contributions to organ dose equivalents were similar to, or greater than, the sum of all heavy ion contributions for most of the thickly-shielded ISS locations. Overall, these experiments demonstrate neutron and light ion importance when calculating biological endpoints behind thick shields. Unfortunately, neutron and light ion cross section and yield measurements are not well-represented in the literature, which contributes significantly to the uncertainty associated with long-term GCR exposure calculations [11].

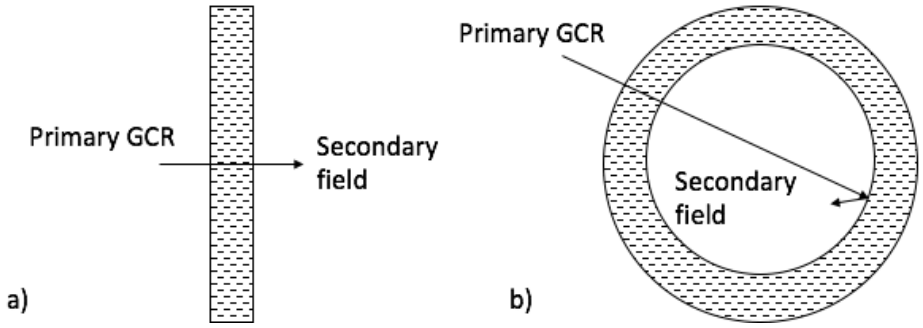


Figure 4. Representative primary and secondary radiation fields for (a) single shield and (b) fully-enclosed shielded geometry.

II.5 Influence of a Second Shield

Additional calculations were performed by Slaba *et al.* [35] for GCR incident on a dual-slab geometry with a water target measurement point between the two identical shields. This geometry more closely modeled the projectile-target interactions observed in a fully enclosed environment, such as in a spacecraft (Figure 4b). In an enclosed environment, primary GCR may interact first in the "front" shield and then a second time in the "back" shield. Similarly, the secondary radiation produced by the primary GCR interactions in the "front" shield may also interact in the "back" shield. Monte Carlo codes considered in this study included FLUKA [36], Geant4 [37] with two physics model packages, MCNP6 [28], and PHITS [29]. Three versions of the deterministic code HZETRN were also studied using the straight-ahead (N=1), bi-directional (N=2), and three-dimensional (N=34) neutron and light ion transport approximations [38], [39].

For a dual-slab geometry of varying aluminum thicknesses, a minimum in the total dose equivalent was calculated near 20 g/cm^2 (Figure 5, left) [35]. As the aluminum thickness increased above 20 g/cm^2, the total dose equivalent between the shields also increased, mostly due to the production of secondary neutrons and light ions. Approximately 70% of the total dose equivalent above 20 g/cm^2 was attributed to protons, while about half of those contributions originated from *n-p* scattering reactions. It was also noted that the total dose equivalents calculated by the transport codes varied as the aluminum thickness increased. This variance in dose equivalents at large aluminum thicknesses was due to the uncertainties in the secondary light ion production models [35].

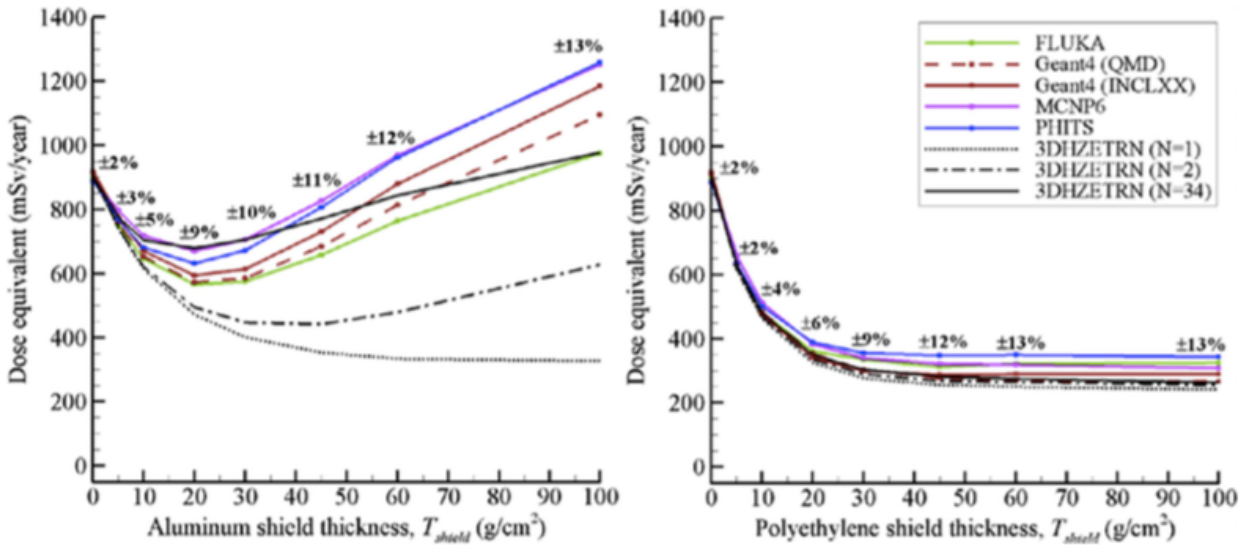


Figure 5. Total dose equivalent for GCR on varying thicknesses of aluminum (left) and HDPE (right). Statistics show maximum Monte Carlo result minus the 3DHZETRN result, divided by the average of the values [35].

Contrastingly, a total dose equivalent minimum was not observed with dual shields of HDPE (Figure 5, right) [35]. This was because the hydrogen-rich HDPE elastically scattered with and moderated neutrons below 10 MeV, decreasing the number of neutron-produced target fragments at the measurement point. Additionally, non-elastic projectile-target interactions generated less HDPE target fragments when compared with aluminum [35].

II.6 Thick GCR Shielding Project

If accurate, the existence of a range of optimal shielding thicknesses has vast implications for the future cost and duration of space travel. In spacecraft and habitat design, an optimal shielding thickness would curb the expenses incurred by launching additional unnecessary, and even harmful, shielding materials. Researchers may also shift focus to the development of novel shielding materials that improves astronaut protection while working within thickness restraints [35]. Furthermore, an optimal shielding thickness indicates that astronauts on long-term missions

will acquire a minimum dose equivalent that cannot be reduced, possibly restricting mission durations or leading to changes in the radiation limits.

Before any of these topics may be addressed, it is important to validate the accuracy and reliability of the calculations using experimentally-measured data [31]. To do this, a dual-target, accelerator-based experiment was designed to help rigorously quantify the uncertainty in neutron and light ion production in typical GCR interactions with thick targets [40]. Due to the large variety of possible GCR ion and shielding interactions, projectile-target systems that represented the range of charges prominently observed in the GCR environment were selected (Table 1). Neutrons and light ions were measured for each listed beam-target system at six angular locations. Upon completion of the measurements campaign, thick-target neutron and light ion yields will be passed to NASA LaRC to quantify the uncertainty in transport code outputs [31], [40].

Projectile species were chosen to represent the major components of the GCR spectrum. Proton and helium projectiles contribute largely to the total GCR fluences, while iron is a significant dose contributor. Carbon and silicon were added to explore the mid-mass GCR ions. Projectile energies varied from 400 to 1500 AMeV (or 2500 MeV for protons) and were selected because they fell within or above the observed range of maximum GCR fluences.

Table 1. Projectile-target matrix for "Thick GCR Shielding Project." Blue, green, and gray boxes indicate data collected in Mar. 2016, Nov./Dec. 2016, and Nov./Dec. 2017, respectively.

Beam Energy (AMeV)	**Projectile Species**														
	H			**He**			**C**			**Si**			**Fe**		
400	Al	CH_2	Al / CH_2	Al	CH_2	Al / CH_2	Al	CH_2	Al / CH_2	Al	CH_2	Al / CH_2	Al	CH_2	Al / CH_2
800	Al	CH_2	Al / CH_2	Al	CH_2	Al / CH_2	Al	CH_2	Al / CH_2	Al	CH_2	Al / CH_2	Al	CH_2	Al / CH_2
1500 (2500 for H)	Al	CH_2	Al / CH_2	Al	CH_2	Al / CH_2	Al	CH_2	Al / CH_2	Al	CH_2	Al / CH_2	Al	CH_2	Al / CH_2

Aluminum targets were selected due to their common use in spacecraft construction. Additionally, HDPE (i.e. CH_2) targets served as a representative hydrogenous shielding material, which were favorable neutron moderators. All upstream single-material targets were 20, 40, and 60 g/cm^2 thick to sample the region at and above the calculated dose equivalent minimum in a fully enclosed environment. It should be noted that not all projectiles were fully stopped by the target. Layered aluminum and HDPE targets were also considered, though not in this study, to replicate a more realistic shielding environment (10 g/cm^2 of aluminum in front of either 10 or 50 g/cm^2 HDPE). In addition to the upstream target, a second, downstream 60 g/cm^2 aluminum or HDPE target was added to mimic an enclosed environment. This target allowed for the study of neutrons and light ions produced in the "back" shield, similar to the calculations described in Section II.5. Neutrons and light charged ions were measured for the 135 projectile-target systems at six angular locations (10°, 30°, 45°, 60°, 80°, and 135°) to fully cover the production regions for the various types of projectile-target interactions.

The 500 hours of beam-time measurements shown in Table 1 will be conducted at NSRL and completed in November 2017. NSRL is a NASA-funded and BNL-managed accelerator facility devoted to space radiation research. Most experiments conducted at NSRL are funded by NASA or are related to NASA's research portfolio, covering areas of study such as radiobiology, electronics testing, or nuclear physics [41]. Experiments are set up in the 37 m^2 shielded target room adjacent to a 424 m^2 support and laboratory facility. The target room is located at the end of a 100-m beam transport tunnel which is connected to the Booster Synchrotron (Figure 6). The Booster also services BNL's Alternating Gradient Synchrotron and the Relativistic Heavy Ion Collider, and may deliver ion species from protons to uranium with ion-dependent energies ranging from 50 to 2500 AMeV [42].

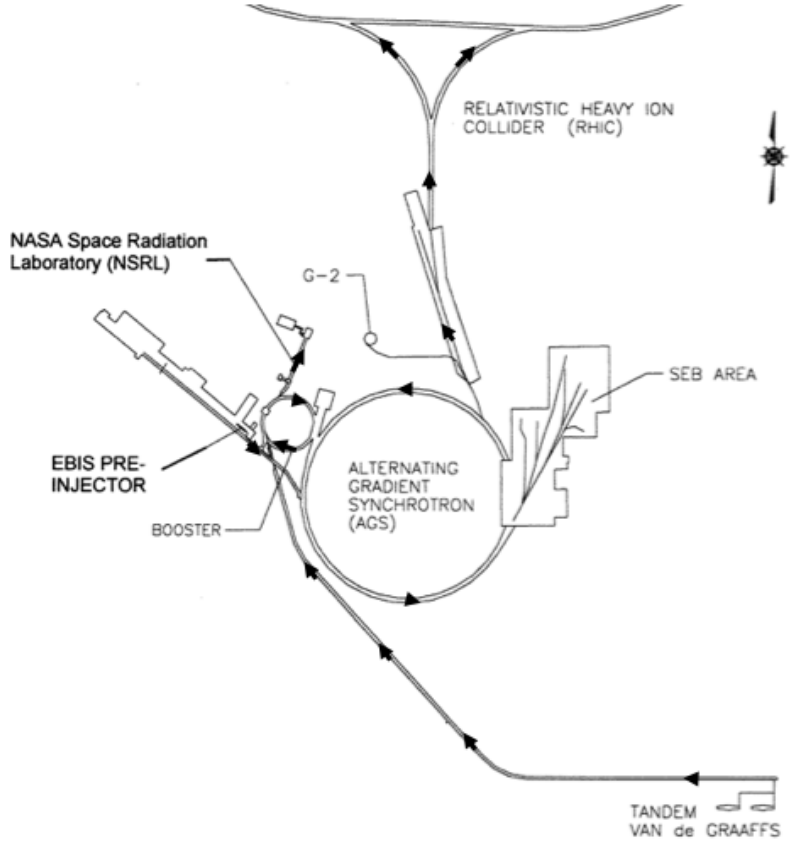


Figure 6. BNL accelerator facilities schematic [43].

III. LITERATURE REVIEW

III.1 Existing Double Differential Thick-Target Neutron Yield Measurements

As previously mentioned, double differential thick-target (DDTT) neutron yields are necessary to validate the accuracy of radiation transport code outputs. Despite their importance, reported thick-target neutron yields are scarce in the literature, especially for GCR-like projectile-target interactions in the energy (400 – 800 AMeV) or thickness (20 – 60 g/cm^2) ranges of interest for this work. Furthermore, no literature data exists for thick-target neutron yields produced by a dual-target geometry. As a result, the yields presented in this work may not be directly compared to experiments in the literature. However, these results may be carefully compared to similar single target systems at forward angles to explore general trends in the measurements. Great care should be taken due to the uncertainties introduced during background subtraction at low energies, particularly for angles closest to the downstream target and beam dump.

A review was conducted for proton, helium, and heavy ion ($2< Z \leq 28$) projectiles above 100 AMeV, incident upon any single thick target. Unless otherwise noted, the targets were thick enough to fully stop the incident projectile. DDTT neutron yields were reported in units of neutrons per source particle per steradian per energy ($\# \, neutrons \, / \, S. \, P. \, / \, \Omega \, / \, MeV$).

As the most abundant ion in the GCR spectrum, proton-induced thick-target neutron yields represent a highly-desired dataset (Table 2). While thin-target cross section data were prevalent, the existing thick-target neutron yield data were typically measured at lower projectile energies than desired. For proton interactions with single targets in the desired energy range, many of the target materials were not useful for GCR shielding design. Similarly, the energies of incident helium projectiles were lower than desired (Table 3), although many of the selected targets were of interest (e.g. water, Al, acrylic). The heavy-ion-induced neutron yields (Table 4) collected at Japan's Heavy-Ion Medical Accelerator [44]–[48] Michigan State University's National Superconducting Cyclotron Laboratory [49], and Germany's GSI Helmholtz Centre for Heavy Ion Research [50], [51] represented a necessary first look at a series of GCR-like thick-target interactions, but they were not directly applicable to this work.

Table 2. Existing measurements of proton-induced thick-target neutron yields.

Beam Energy (MeV)	Stopping Target	Measurement Angle (degree)	Reference
113	Be, C, Al, Fe, DU[a]	7.5, 30, 60, 150	[32]
140	Graphite, Al, Fe, Pb	0	[52]
160	H_2O, C, Al, Cu, Co, Bi	0, 10, 45	[53]
210	Fe	0, 7.5, 15, 30, 60, 90, 110	[54]
250	Graphite, Al, Fe, Pb	0	[52]
256[b]	C, Al, Fe, DU[a]	7.5, 30, 60, 120, 150	[55], [56]
350	Graphite, Al, Fe, Pb	0	[57], [52]
450[c]	C, Al, Co	0, 10, 20, 45	[58]
500	Pb, W	15, 30, 60, 90, 120, 150	[59], [60]
740	DU[a]	50, 130	[61], [62]
1500c	Pb, W	15, 30, 60, 90, 120, 150	[59] , [60]

[a] Depleted uranium (DU)
[b] Stopping-length and/or near stopping-length targets
[c] Near stopping-length targets only

Table 3. Existing measurements of helium-induced thick-target neutron yields.

Beam Energy (AMeV)	Stopping Target	Measurement Angle (degree)	Reference
100	Al, C, Cu, Pb	0, 7.5, 15, 30, 60, 90	[44], [20], [45]
100	Water, acrylic, Fe	0, 15, 30, 60, 90, 117.5	[63], [64]
155	Al	10, 30, 45, 60, 90, 125, 160	[49]
160	Pb	0, 45, 90, 120, 150	[65]
177.5	Water, C, steel, Pb	0, 6, 15, 30, 45, 60, 90, 120, 135, 150	[65]
180	Al, C, Cu, Pb	0, 7.5, 15, 30, 60, 90	[44], [45]
230	Water, acrylic, Fe	0, 15, 30, 60, 90, 117.5	[63], [64]

Table 4. Existing measurements of heavy-ion ($2<Z\leq28$)-induced thick-target neutron yields.

Beam Type/ Energy (AMeV; Z)	Stopping Target	Measurement Angle (degree)	Reference
C (100; Z=6)	C, Al, Cu, Pb	0, 7.5, 15, 30, 60, 90	[44], [45]
C (155; Z=6)	Al	10, 30, 45, 60, 90, 125, 160	[49]
C (180; Z=6)	C, Al, Cu, Pb	0, 7.5, 15, 30, 60, 90	[44], [45]
C (200; Z=6)	Water	0, 10, 20, 30	[50]
C (400; Z=6)	C, Al, Cu, Pb	0, 7.5, 15, 30, 60, 90	[44], [45]
C (400; Z=6)	Graphite	0, 7.5, 15, 30, 50, 90	[51]
C (1000; Z=6)	Fe	0, 7.5, 15, 30, 50, 90	[51]
Ne (100; Z=10)	C, Al, Cu, Pb	0, 7.5, 15, 30, 60, 90	[46], [45]
Ne (180; Z=10)	C, Al, Cu, Pb	0, 7.5, 15, 30, 60, 90	[46], [45]
Ne (400; Z=10)	C, Al, Cu, Pb	0, 7.5, 15, 30, 60, 90	[46], [45]
Si (800; Z=14)	C, Cu	0, 7.5, 15, 30, 60, 90	[48], [45]
Ar (400; Z=18)	C, Al, Cu, Pb	0, 7.5, 15, 30, 60, 90	[48], [45]
Fe (400; Z=26)	C, Al, Cu, Pb	0, 7.5, 15, 30, 60, 90	[48], [45]
Fe (400; Z=26)	C, Al, Cu, Pb	90, 120, 160	[47]

For most of the experiments listed above, DDTT neutron yields were measured for transport code benchmarking or shielding design purposes. Many experiments were conducted to validate the outputs of transport codes using various intranuclear cascade models. PHITS, MCNPX, FLUKA, and HETC were among the considered codes. Other neutron yield measurements were incorporated into the shielding design of accelerator facilities. With these experiments, neutron yields were used to estimate the secondary neutron source terms in accelerator facility target rooms, beam dumps, switch yards, and production targets. These source terms could then be used to determine neutron exposures for personnel, predict radiation damage to materials, or validate shielding configurations. While the work presented in the literature is applicable and useful in a variety of scenarios, significant research gaps exist for thick-target neutron yields produced by GCR-like interactions. Furthermore, no data exist for thick-target neutron yields produced with a dual-target setup.

IV. EXPERIMENTAL SETUP AND ANALYSIS TECHNIQUES

IV.1 Experimental Setup

IV.1.1 Overview

In March 2016, 100 hours of secondary neutron and light charged ion measurements occurred at the NASA Space Radiation Laboratory (NSRL) facility at Brookhaven National Laboratory (BNL). BNL's Booster synchrotron was used to deliver the 400 and 800 AMeV iron, 400 and 800 MeV proton, and 400 AMeV helium projectiles to the upstream aluminum target with areal densities of 20, 40, and 60 g/cm^2. Additionally, a 60 g/cm^2 thick aluminum target was added 350 cm downstream from the middle of the upstream target to eventually study neutrons scattered from or produced in the back target. Two start scintillators were centered in front of the upstream target to identify valid beam particles. Liquid scintillator arrays were placed along beam-left at 10°, 30°, 45°, 60°, 80°, and 135° off the beam axis, while sodium iodide (NaI) arrays were placed along beam-right at 10° and 30°. The beam entered the experiment room at a height of 121.92 cm and all detector centers were aligned to this height. Secondary neutrons were measured in the liquid scintillators while secondary light charged ions were measured in the liquid scintillators and NaI arrays. Overall, secondary neutron production was measured for fifteen beam-target systems at six angular locations. A schematic representation of the NSRL target room and a photo of the actual setup are shown in Figure 7 and Figure 8.

IV.1.2 Projectile Beams

The following projectile beams and energies were selected for the March 2016 experiment: 400 and 800 AMeV iron, 400 and 800 MeV protons, and 400 AMeV helium projectiles. All beams were delivered by BNL's Booster Synchrotron. Within the Booster, the helium and iron projectiles were accepted from the Electron Beam Ion Source (EBIS)[1] while the proton projectiles were

[1]Ion species of +1 helium and iron were created in the hollow cathode and laser ion sources, respectively, and injected into the EBIS magnetic trap [66], [41]. A high-density electron beam was passed through the trap until the

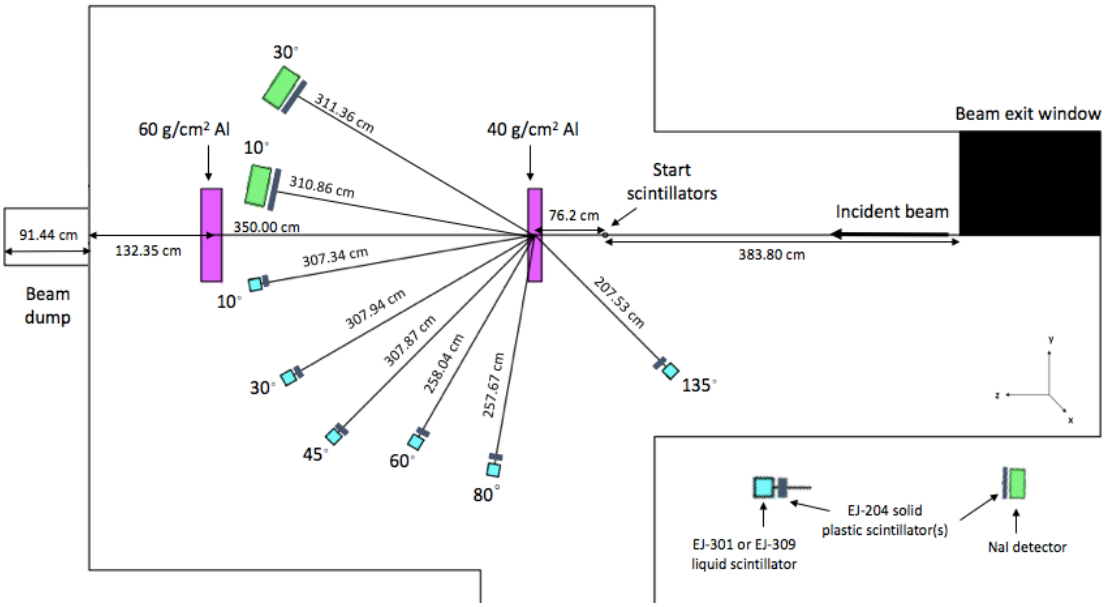


Figure 7. NSRL target room schematic. Listed flight paths are from the center of the upstream target to the center of the detectors.

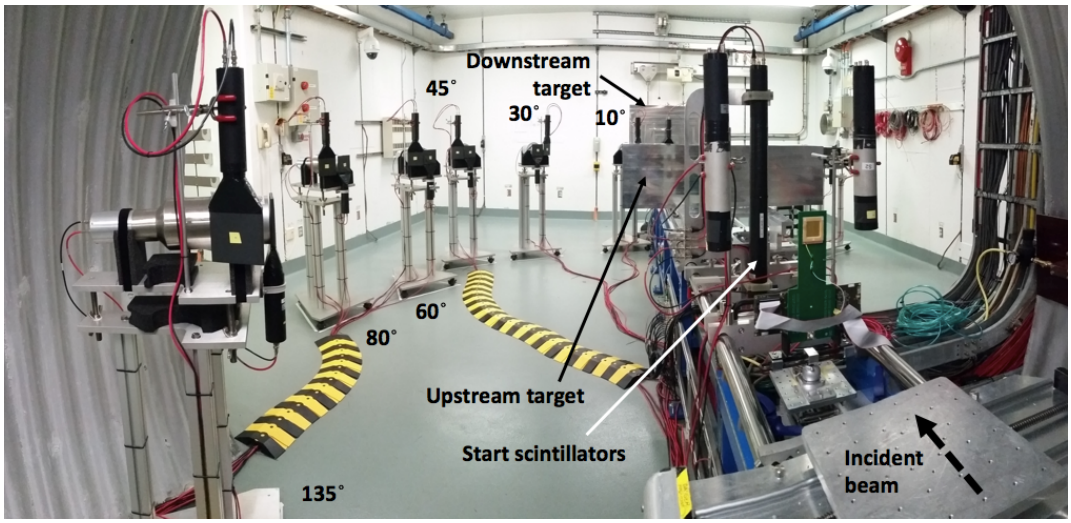


Figure 8. Experimental setup in NSRL target room.

desired ion charge state was achieved. The ions were then extracted, pre-accelerated to 2 AMeV, and injected into the Booster [43]. With the Tandem van de Graaff, hydrogen anions were accelerated, stripped of their electrons and converted to protons, and then accelerated again. Protons were then extracted and injected into the Booster [67].

accepted from the Tandem van de Graaff (Figure 6). After acceleration in the Booster, projectiles were sent down the NSRL beam line, passed through a 381 μm aluminum exit window, and entered the target room at a height of 121.92 cm. Beam spills lasted between approximately 0.5 and 2.0 s, depending upon the projectile species and energy. Similarly, the full width at half maximum (FWHM) values for the beam spots varied between 3 and 7 cm. Approximately 1,000 to 2,000 particles were delivered per spill.

IV.1.3 Targets

Upstream targets had a cross sectional area (width by height) of 100 by 30 cm^2, while the downstream target had a cross sectional area of 100 by 100 cm^2. The upstream aluminum target varied in thickness while the downstream target was fixed at 60 g/cm^2. Areal thicknesses of 20, 40, and 60 g/cm^2 corresponded to thicknesses of 7.41, 14.81, and 22.22 cm for aluminum (density = 2.7 g/cm^3). Each target was constructed out of 10 g/cm^2-thick aluminum slabs that were layered together to achieve the desired thickness. This meant a target change consisted of the removal or addition of two aluminum slabs instead of replacing the entire target, decreasing the downtime between target changes. Upstream targets were attached to a stand which was secured to the beam line, while the downstream target sat on a cart placed at the end of the beam line (Figure 9). The centers of the upstream and downstream targets were separated by 350 cm.

Using the NIST range tables for protons in aluminum, the ranges of 400 and 800 AMeV iron, 400 and 800 MeV protons, and 400 AMeV helium ions were scaled by A/Z^2 (projectile mass divided by its squared charge) and calculated [68]. Of the fifteen beam-target systems, only a third of the systems resulted in a beam that was fully stopped by the upstream target (Table 5). For all other beam-target systems, the primary beam punched through the upstream target and struck the downstream target. Using an energy loss code written in MATLAB, it was further determined that many of the remaining beams also punched through the downstream target and entered the beam dump [69], [70]. The beam dump consisted of a 91.44 cm deep hole in the concrete wall which was covered by a steel door when the beam was turned off.

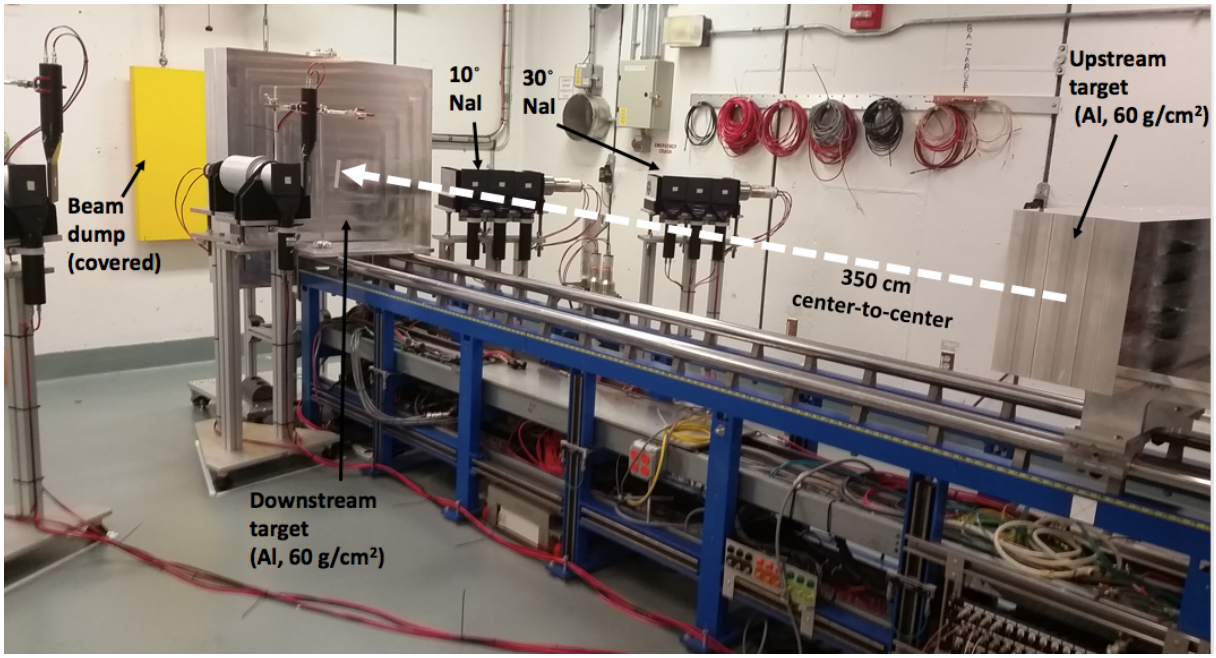


Figure 9. 60 g/cm^2 upstream and downstream aluminum targets.

Table 5. Incident beams that stopped (Y) or did not stop (N) in the 20, 40, and 60 g/cm^2 upstream or the 60 g/cm^2 downstream aluminum targets.

Beam	Energy (AMeV)	Al, 20 g/cm^2		Al, 40 g/cm^2		Al, 60 g/cm^2	
		Up Stop?	Down Stop?	Up Stop?	Down Stop?	Up Stop?	Down Stop?
Iron	400	Y	-	Y	-	Y	-
	800	N	Y	Y	-	Y	-
Proton	400	N	N	N	N	N	Y
	800	N	N	N	N	N	N
Helium	400	N	N	N	N	N	Y

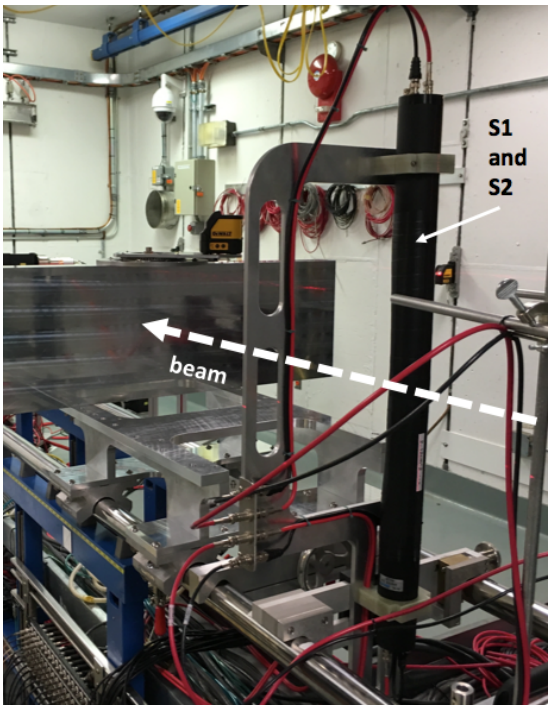
IV.1.4 Start Scintillators

Two different solid plastic start scintillator pairs were used during this experiment, depending upon the beam species. Two EJ-228 paddles were used for the iron beams, while an EJ-228 scintillator array created in-house at BNL was used for the proton and helium beams. EJ-228 scintillators are designed for very fast timing experiments with high count rates and work best when kept to a small size. The polymer base of the detectors is polyvinyl toluene doped with anthracene, which serves as a wavelength shifter. It has a density of 1.023 g/cm^3 [71]. Both scintillator centers were separated by 7.9 cm and placed 78.45 cm in front of the upstream target. The upstream and downstream start scintillators (S1 and S2) had cross sectional areas of 4 by 4 cm^2 and 5 by 5 cm^2, respectively. Both scintillators were 0.2 cm thick. Operating voltages for S1 and S2 were both set to 1500 V for the iron projectiles.

For the proton and helium beams, the EJ-228 gains were too small and the scintillators triggered on ambient gammas in addition to the incident beam. This resulted in high individual but low coincidence counts between S1 and S2. The paddle scintillators were switched out with the BNL scintillator array which had a different photomultiplier tube (Figure 10a). The centers of the scintillators were separated by 3 cm and the tube (5.08 cm diameter) was centered 76.2 cm in front of the upstream target. S1 and S2 had cross sectional areas of 1 by 1 cm^2 and 1.4 by 1.4 cm^2, respectively. Both were 0.2 cm thick. Voltages were adjusted for each beam to ensure the start scintillator pulse height spectra were not off-scale. Operating voltages for S1 and S2 were set to 2040 and 1700 V for the proton beams, and 1700 and 1450 V for the helium beam.

IV.1.5 Veto Detectors

Each of the six liquid scintillators were paired with two EJ-204 plastic organic scintillators that were 12.7 cm wide, 12.7 cm tall, and 0.635 cm thick. These detectors are made of polyvinyl toluene with a density of 1.023 g/cm^3 [72]. Due to their thinness and high hydrocarbon content, the probability of neutrons and gammas depositing energy in the "veto" detectors is almost zero [12]. Contrastingly, charged particles interacted in the plastic scintillators with almost 100% efficiency. Because of the difference in the interaction methods of incident particles, these veto detectors were

a) 

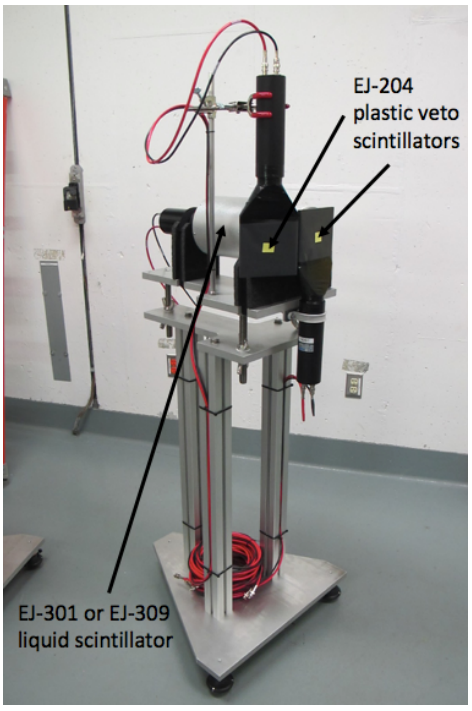
b) 

Figure 10. (a) BNL start scintillator tube with upstream aluminum target and (b) liquid scintillator array on custom cart.

used to separate neutral and charged particle events that were subsequently detected in the liquid scintillators. To ensure that incident neutral and charged particle events were properly tagged, one veto was placed directly before the front face of the liquid scintillator while the second veto was angled to cover the side of the liquid scintillator facing the beam line (Figure 10b). This ensured that any secondary charged particles produced in the air column between the two targets would be properly tagged if they entered the liquid scintillator. Additionally, three EJ-204 scintillators (CS paddles) were arranged in front of each NaI array. The twelve veto detectors and six CS paddles were operated at 2000 V.

IV.1.6 Liquid Scintillators

Organic liquid scintillators were utilized in this experiment due to their excellent pulse shape discrimination (PSD) properties in fast-neutron environments [73]. When ionizing radiation interacts in the active volume liquid, some of the deposited energy excites the organic molecules to discrete states. These molecules then de-excite by emitting light, which eventually produces an electrical signal [10]. For neutral particles like neutrons and gammas, the recoil nuclei (i.e. protons) and electrons are respectively responsible for scintillating the liquid. PSD takes advantage of the difference in the pulse shapes of these protons and electrons [74]–[76]. The mechanisms that determine a given particle's pulse shape are highly complicated but in general, each pulse is composed of a fast and a slow scintillation component [77], [78]. Pulses have a rise time of approximately 10 ns with a several microseconds long decay. The slow component is dependent upon the energy loss density surrounding the particle's track, and is more intense for heavily ionizing particles (i.e. protons) rather than electrons [79]. Heavily ionizing particles will thus have a more pronounced pulse tail when compared to an electron pulse, especially near the end of its track. This difference makes it possible to separate neutron and gamma events by comparing the relative light outputs of the fast and slow components of the pulses.

This experiment used EJ-301 and EJ-309 liquid scintillators. According to the manufacturer, EJ-301 is identical to NE-213 and thus demonstrates the same properties [80]. NE-213 has a density of 0.827 g/cm^3 and is composed of the organic compounds xylene, naphthalene, POPOP, and

activators. EJ-309 was developed as an alternative to EJ-301, whose low flash point (26°C) characterizes it as a flammable liquid [81], [82]. EJ-309 has a high flash point (144°C), making it more favorable for use in difficult environmental conditions. However, EJ-309 has a slightly worse PSD ability [83].

EJ-301 liquid scintillators were used at 10°, 30°, and 45°, while EJ-309 liquid scintillators were used at 60°, 80°, and 135°. Both scintillators were right cylinders with an active volume diameter and height of 12.7 cm, and both were encased in aluminum housing with a thickness of 0.152 cm on the sides and front face. The liquid scintillators were placed on a rolling cart with their veto detectors for ease of setup, as shown in Figure 10b. Operating voltages were chosen to allow for both neutron and charged particle detection, rather than to maximize the PSD properties of the liquid scintillators (Table 6). This meant the operating voltages were lower than ideal for neutron detection and higher than ideal for charged particle detection. Despite this, neutron-gamma discrimination was still achieved below 5 MeV. The voltage at 10° was higher than at 30° and 45° to compensate for a lower level of neutron-gamma separation observed before the experiment. Voltages at 60°, 80°, and 135° were higher than at forward angles due to the decrease in measured charged particles at wide angles. Because neutrons could originate from anywhere along the centerline of the upstream target and be detected anywhere in the liquid scintillators, the flight path was taken from the center of the upstream target to the center of the liquid scintillator. These values are listed in Table 6 and include the separation between the front faces of the veto detector and the liquid scintillator (1.08 to 1.50 cm), as well as the aluminum housing thickness.

Table 6. Operating voltages and flight paths for liquid scintillators.

Liquid scintillator (angle)	Operating Voltage (V)	Flight path (cm)
10°	1500	307.34
30°	1400	307.94
45°	1400	307.87
60°	1700	258.04
80°	1700	257.67
135°	1900	207.53

IV.1.7 Shadow Bar System

The background neutron environment mainly consisted of neutrons that scattered throughout the target room before they were detected in the liquid scintillators. Two shadow bars were used to characterize background neutrons by completely blocking particles coming directly from the upstream target to the liquid scintillator array. This meant any neutron event that registered in the scintillator volume was considered background. The iron shadow bars were 91 cm and 182 cm in length with a diameter of 12.7 cm. Both were attached to rolling stands with adjustable heights (Figure 11). When in use, each shadow bar was placed directly in front of a liquid scintillator array and lined up with the upstream target using the in-room laser alignment system (Figure 12).

To characterize the background, the following shadow bar configurations were executed for each beam-target system, resulting in at least four individual runs per system: configuration A: no shadow bars; configuration B: 182 cm bar at the 10° array and 91 cm bar at the 60° array; configuration C: 182 cm bar at the 30° array and 91 cm bar at the 80° array; configuration D: 182 cm bar at the 45° array and 91 cm bar at the 135° array. For a given scintillator location, three of the four datasets were considered "un-shadowed" which meant they recorded background neutrons and neutrons produced in the upstream target. The remaining run with the shadow bar in front of the scintillator was considered "shadowed" and only consisted of background neutrons. Shadowed runs were eventually subtracted from un-shadowed runs to eliminate neutron background.



Figure 11. 182 cm iron shadow bar, target room hallway.

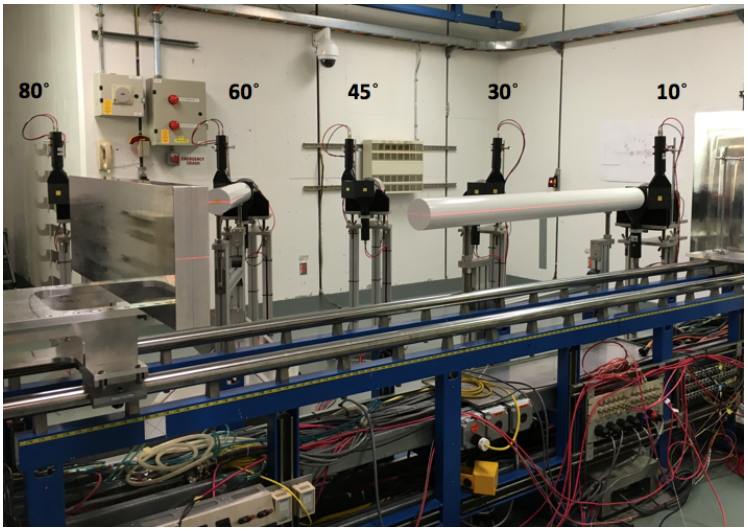


Figure 12. Shadow bar alignment for liquid scintillators at 10° and 60°, configuration B.

IV.2 Electronic Equipment and Data Acquisition

IV.2.1 Trigger Logic

To measure the time of flight (TOF) of particles created in the upstream target, the equipment listed in Table 14 (Appendix I) was arranged according to the electronic logic diagram in Figure 13. The complete logic system is shown in Figure 14, and an example of the coincidence signals needed to set the acquisition gate is shown in Figure 15. Data were acquired on an event-by-event basis that was set by an acquisition trigger. Organic liquid scintillators (OLS), CS paddles, S1, and S2 were included in the trigger logic while the NaI and veto detectors were not included. All detectors were cabled such that their signal transit times were the same. The acquisition trigger started with a detection event in a liquid scintillator or CS paddle and stopped with the arrival of a delayed logic signal from the start scintillators. This ensured that all time-to-digital converter (TDC) units stopped acquiring data even if the detector did not register an event, which increased the time in the TDC histograms from right to left. During this time, charge deposition and timing information was recorded for all detectors via charge-to-digital converters (QDCs) and TDCs.

The first component of the trigger logic involved the S1 and S2 scintillators. For both detectors, the negative signal was passively split. One of the split analog signals was delayed and sent to a 10-bit QDC to obtain a pulse height spectrum. The second analog signal was sent to a constant

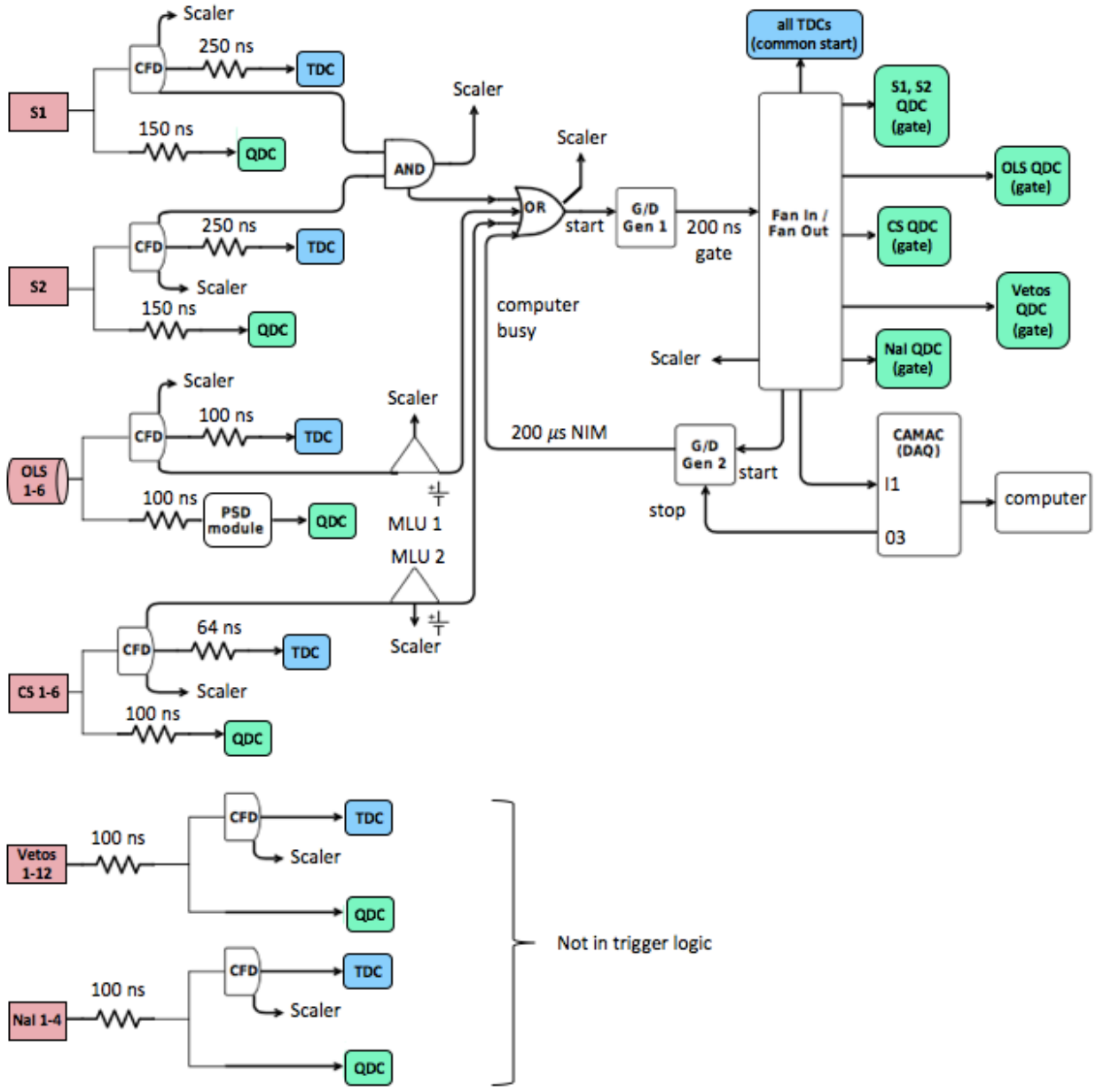


Figure 13. Electronic logic map.

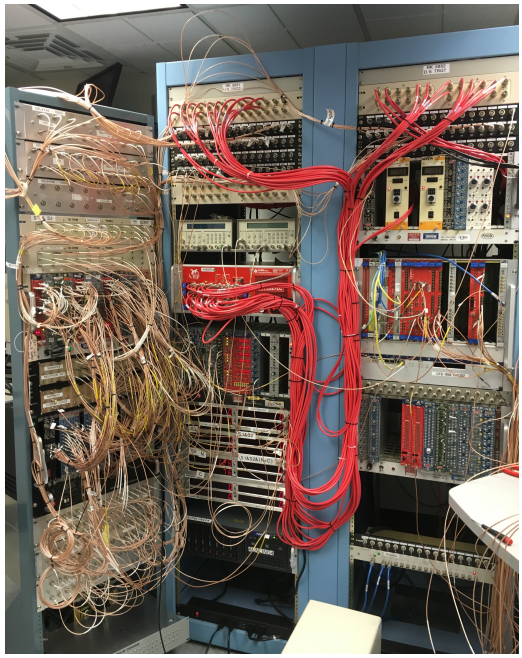


Figure 14. Physics room with logic equipment at NSRL.

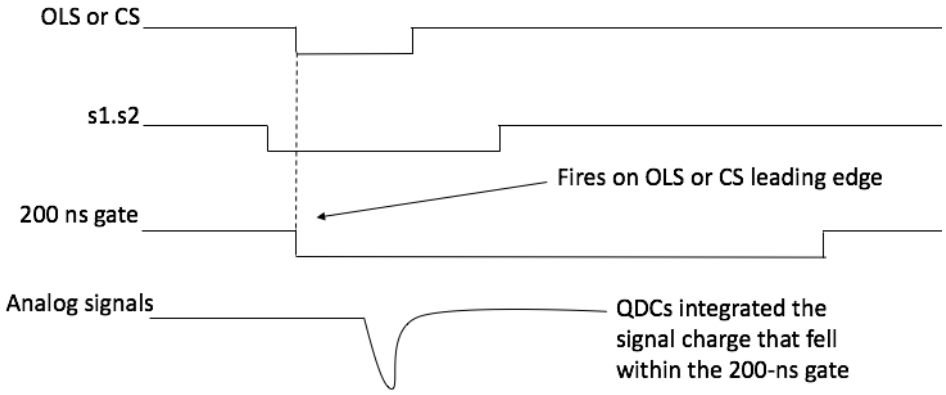


Figure 15. Coincidence between (OLS or CS) AND *s1.s2* setting the acquisition gate and trigger.

fraction discriminator (CFD) which output logic NIM signals if the input signal surpassed an internal, user-adjusted threshold. Of the multiple CFD outputs, one was delayed and used as the STOP signal for TDC acquisition. Another was input to an *AND* coincidence module which fired a logic NIM signal when S1 and S2 were in coincidence (*s1.s2*).

Similarly, the negative signal of the six OLS were passively split. For the OLS, one analog signal was delayed and put into a PSD module. This module outputted four signals, the total signal (*t_qdc*), total attenuated signal (*ta_qdc*), head signal (*h_qdc*), and head attenuated signal (*ha_qdc*), which were all fed into an 11-bit QDC. The head signal was found by integrating the charge deposited in the first 20 to 35 ns of the total signal, while the attenuated signals were found by dividing the total and head signals by an internal factor. The second OLS analog signal was sent to a CFD where the outputs were sent to the OLS TDC STOP after external delay, as well as a multiplicity logic unit (MLU). MLUs fired a logic signal with >1 input. Because an external voltage supply was used to force one *TRUE* condition, any input from an OLS CFD output a logic signal. This electronic mapping was replicated for the six CS paddles with the exception that the PSD module was taken out and a shorter external delay was utilized before the TDC unit.

At this point, three output signals of interest existed: the coincidence start signal *s1.s2*, a signal from any OLS, and a signal from any CS paddle. These signals were fed into an *OR* coincidence module which fired a logic pulse when two of the three signals were in coincidence. Because the signal transit times between all detectors were the same, *s1.s2* theoretically arrived in the *OR* coincidence module first and the subsequent arrival of the OLS or CS paddle signal fired the coincidence pulse. Once generated, the *OR* coincidence signal was fed into a gate and delay generator (G/D) which created a 200-ns gate that was actively split and served as the START for all TDCs and the gate for all QDCs (Figure 15). A 200-ns gate was selected because it safely captured the charge deposited by a 5 MeV neutron, the target for low-energy neutron detection. A 5 MeV neutron's TOF ranged from 67.3 to 99.8 ns, depending upon the flight path.

To account for dead time, a 200-μs gate was created with a second G/D after the event gate was set. The 200-μs gate was input to the "computer busy" channel in the *OR* coincidence module. At this point, all other events were blocked from firing an *OR* coincidence signal while the first event

was processed. A signal from the CAMAC reset the second G/D when the event processing was complete. If not, the "computer busy" automatically cleared at the end of 200 μs and the next coincidence event could fire the *OR* signal, restarting the acquisition process.

Scaler modules were utilized at all points in the electronic setup to track the number of events that met certain logic requirements. Scalers of interest for measurement normalization included *s1.s2*, RAW, and LIVE events. *s1.s2* included information on the number of coincidence between S1 and S2. RAW scalers represented all coincidence events that met the conditions for *OR* logic. Contrastingly, the LIVE scalers recorded the events that met the conditions for *OR* logic, were not blocked by the "computer busy" signal, and set the 200-ns acquisition gate. The live time of the system was found by dividing the LIVE and RAW scalers, which gave the fraction of events processed by the CAMAC.

IV.2.2 TDC and QDC Data Acquisition

Even though the use of a "computer busy" signal blocked the processing of multiple triggers at once, event data were acquired in all QDCs and TDCs regardless of which detector set the trigger. With a TDC module, the time intervals between the designated START and STOP signals were proportionally converted to pulse amplitudes, resulting in a time spectrum [84]. This meant that only detectors that set the trigger contained useful timing information. If a coincidence event between *s1.s2* and the OLS at 10° set the trigger, the timing difference between the *OR* coincidence START and OLS-delayed STOP signals in the OLS always occurred at a fixed interval, forming a "self-time" peak at the corresponding channel location. As a result, a neutron TOF spectrum at 10° was created by considering the S1 TDC spectrum for only the events when *s1.s2* was in coincidence with the OLS at 10°. Neutron TOFs increased from right to left in these spectra because faster events had a larger difference between the START and STOP signals, resulting in a higher channel number.

Similarly, the QDC integrated charge deposited in S1, S2, OLS, CS paddles, veto detectors, or NaIs regardless of which detector set the trigger. Coincidence events between *s1.s2* and an OLS

or CS paddle that set the trigger were timed such that the full analog signal was integrated in the QDC during the 200-ns gate. Events that did not set the trigger were mistimed and as such, their signal charge was not always fully integrated in the QDC. Mistimed events were filtered out of the QDC spectra by gating on the self-timed events.

Finally, the raw event-by-event data acquired by the TDC and QDC modules were passed to the DAQ computer via the CC-USB CAMAC Crate controller. The SpecTcl analysis software created by Michigan State University's National Superconducting Cyclotron Laboratory was used to analyze the data online and save it in a readable format [85]. Files were later converted and analyzed offline with the ROOT Data Analysis Framework [86].

IV.2.3 Issues with the Acquisition Trigger

Figure 16 shows the TDC spectrum recorded at the 30° OLS for all beam-target systems. The blue self-time peak was formed with a coincidence between *s1.s2* and the 30° OLS, the pink spectrum was formed with a coincidence between *s1.s2* and the remaining five OLS, while the green spectrum was formed with a coincidence between *s1.s2* and the CS paddles. Additionally, the peak within the green spectrum was formed with a coincidence between the CS paddles and OLS. During data analysis, it was determined that the transit times of the CS paddles and the start scintillators to the electronics room were not equal due to differences in their photomultiplier tubes. This meant the CS paddle signals from high-energy events were arriving at the *OR* gate faster than the *s1.s2* coincidence signal, which shifted many valid events to the left shoulder of the self-time peak. While this did not have much of an effect on the OLS analysis, the issue was fixed in subsequent experiments to improve NaI measurements.

IV.2.4 QDC Calibration

During the setup phase of the experiment, the QDCs for the liquid scintillators were calibrated using button cobalt-60 and cesium-137 gamma sources due to their availability (Table 15, Appendix I). This converted the channel numbers in a QDC spectrum to electron equivalent energy

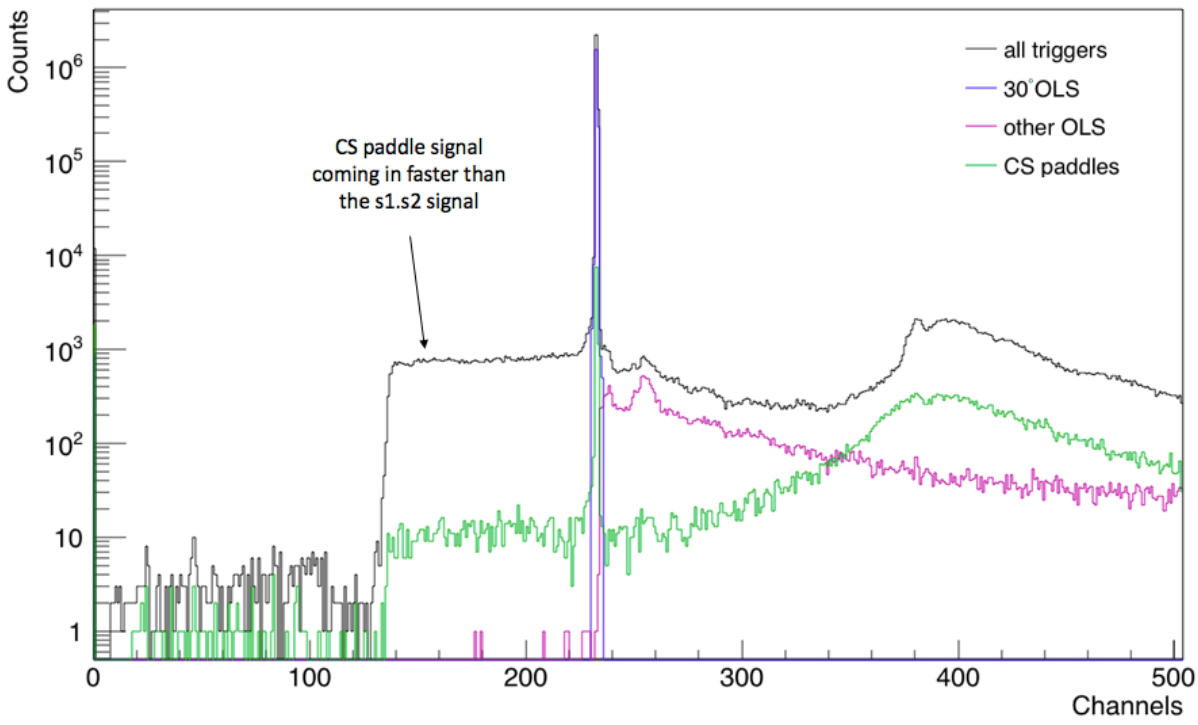


Figure 16. 30° OLS TDC spectra for all beam-target systems gated on all triggers, 30° OLS self-time, remaining five OLS self-times, and CS paddle self-times.

(MeVee) instead of the recoil proton energy (MeV). Liquid scintillators have a linear energy response to gammas above 100 keV and a non-linear energy response to protons [87], [88]. Because of this, an additional calibration based on the data collected in references [81] and [89] was also used to convert between electron-equivalent and recoil proton energies.

Most of the interactions between the incident gammas and liquid scintillators occurred via Compton scattering. In this process, incident gammas scattered off atomic electrons, transferring energy to the electrons which formed the QDC pulse height spectrum [10]. The maximum energy of a recoil electron (E_e) occurred when the incident gamma backscattered at 180° *(θ)*, equaling the Compton edge energy (equation 4). E_γ was the incident gamma energy of the button sources, and m_e was equal to 0.511 MeV/c^2. Using the button sources, the channel number corresponding to 80% of the right edge of the maximum counts was found and set equal to the Compton edge energy [81]. Additionally, the pedestal peak was recorded and set equal to 0 MeV. The cobalt-60, cesium-137, and pedestal channel values were then fitted linearly. The fit equations were used to convert QDC channel numbers to electron-equivalent energies. This process was repeated for all liquid scintillators and the resulting calibrations are shown in Figure 17.

$$E_e = E_\gamma \cdot \left[1 - \frac{1}{1+\left(\frac{E_\gamma}{m_e}\right)\cdot(1-\cos\theta)}\right] \tag{4}$$

IV.2.5 TDC Calibration

TDC channels were calibrated using a pocket pulser and LEMO cables of various lengths. First, the peak location in the TDC spectra was recorded with no delay cable. Next, the peak locations were recorded when 8 ns and 16 ns of delay were added using the LEMO cables. The three channel locations were plotted and the slope of the linear fit was calculated (Table 7). These slopes represented the time division per TDC channel (tdc_{cal}) and were later used to calculate neutron TOF.

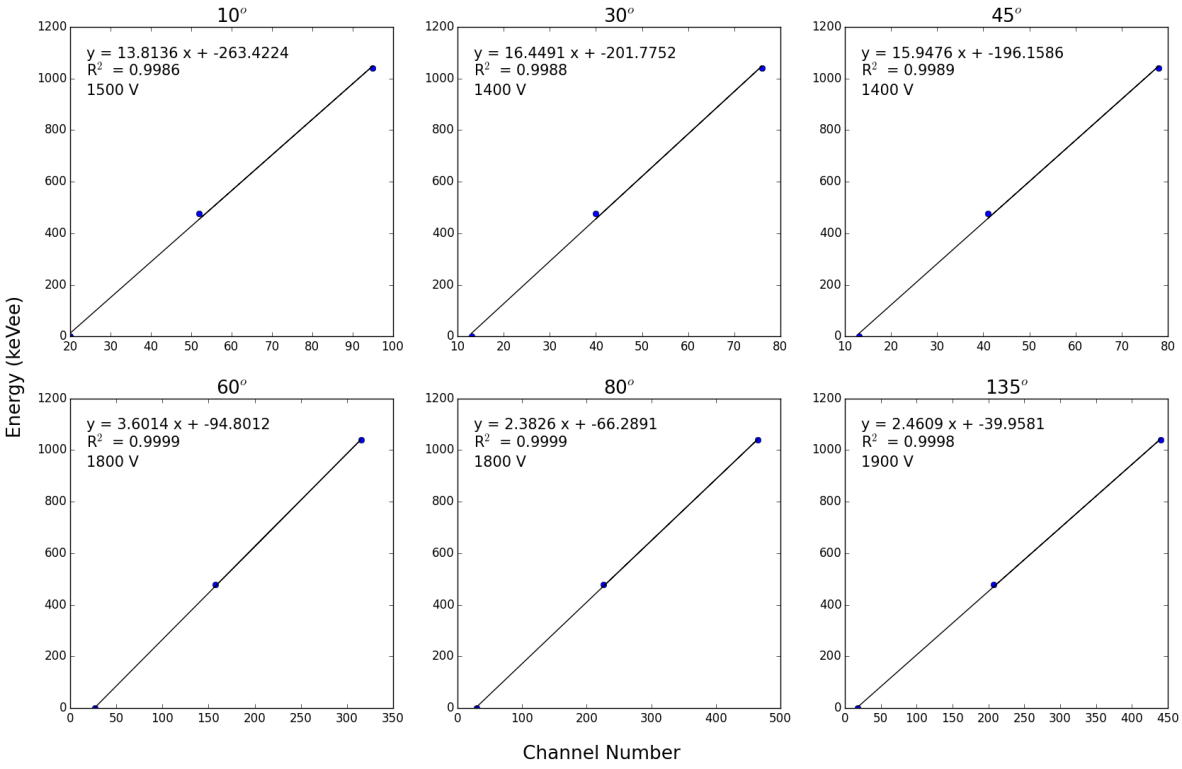


Figure 17. Gamma calibrations for liquid scintillators at operating voltages.

Table 7. TDC calibration for liquid scintillators.

Liquid scintillator (angle)	Time per TDC channel (ns/ch)
10°	0.238
30°	0.237
45°	0.235
60°	0.232
80°	0.235
135°	0.229

IV.3 Data Filtering

IV.3.1 Overview

Each ROOT file contained event-by-event information for the six liquid scintillators and six NaI detectors at a given beam-target configuration. To generate double differential thick-target (DDTT) yields for neutrons originating from the upstream target, valid neutron events were isolated from the total event data using a series of gates. These gates were designed to eliminate any event that did not fall within its user-specified parameters. By taking an output spectrum of interest and applying various gates, the same data could be filtered in multiple ways. To extract valid neutron event information, multiple filters were designed to: 1) eliminate data not contained within the good beam gate; 2) eliminate events in the liquid scintillator that did not set the coincidence trigger; 3) eliminate charged particle events; 4) separate neutron and gamma events; and 5) eliminate background neutron events. After these gates were applied, the TOF technique could be applied to the neutron event data to calculate DDTT yields.

IV.3.2 Good Beam Gate

Good beam gates were used to eliminate charge deposited in the start scintillators that did not correspond to valid events. For example, the gate eliminated double hits which occurred when two beam particles simultaneously entered the start scintillators and depositing twice the energy, but were registered as a single hit by the scalers. Other events eliminated included fragments that formed when the beam projectiles broke up in the air column before the start scintillators, or primary beam projectiles or fragments that struck S1 or S2, but not both. These gates were created by plotting the charge deposited in S1 versus S2 for all runs taken for a given beam species and energy, and then taking a graphical cut around the primary beam spot. Examples of good beam gates for three of the five beam species are shown below in Figure 18 through Figure 20. The beam spots were well-defined for the 400 and 800 AMeV iron species, containing 80.1% and 88.4% of the total events, respectively. However, the diffuse nature of the charge deposited by the 400 and 800 MeV proton projectiles meant that 58.8% and 66.5% of the total events were contained within the beam spot. The 400 AMeV helium beams contained 77.4% of the total events in the beam spot.

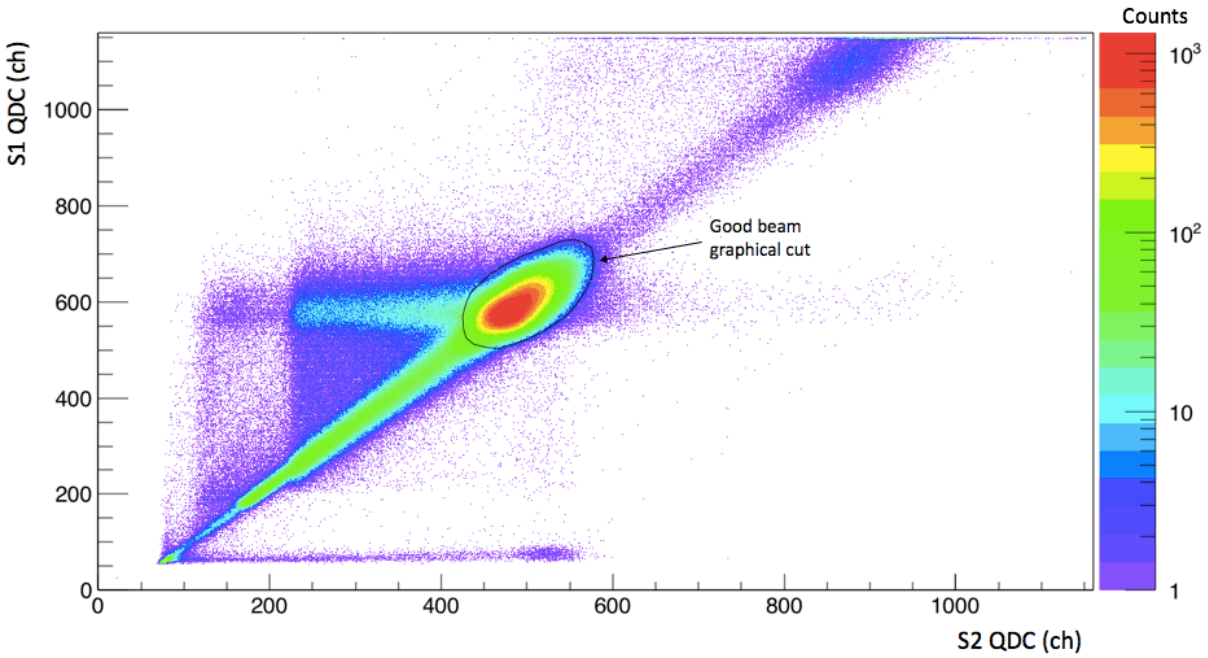


Figure 18. Charge deposited in S1 and S2 scintillators for 800 AMeV iron on all targets.

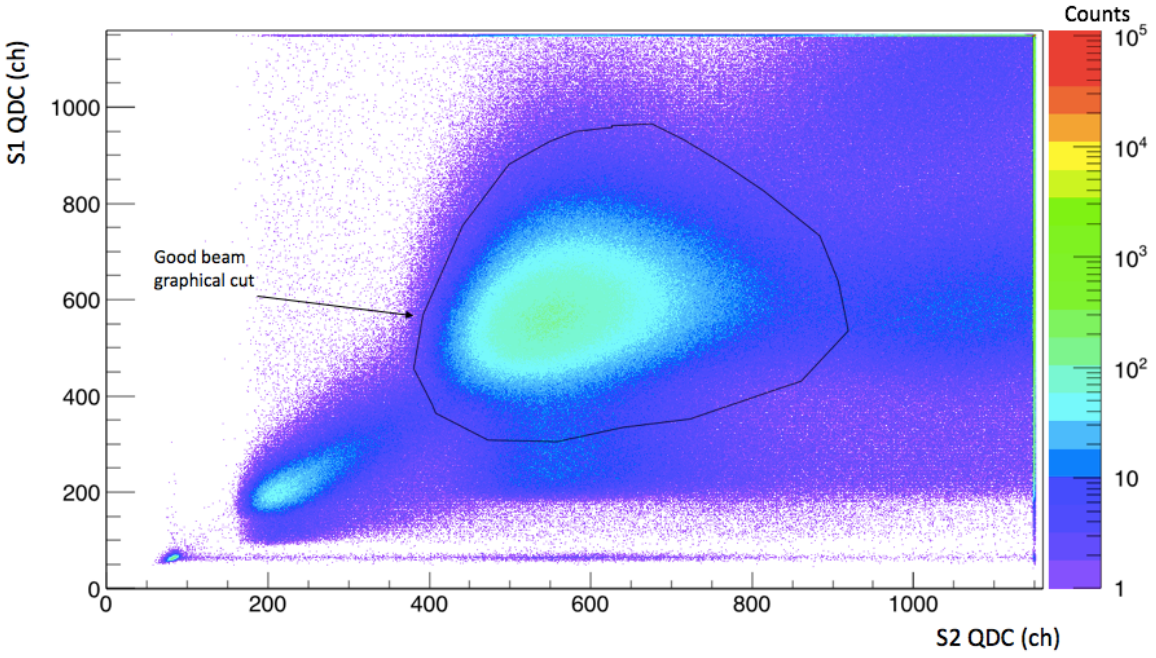


Figure 19. Charge deposited in S1 and S2 scintillators for 400 MeV protons on all targets.

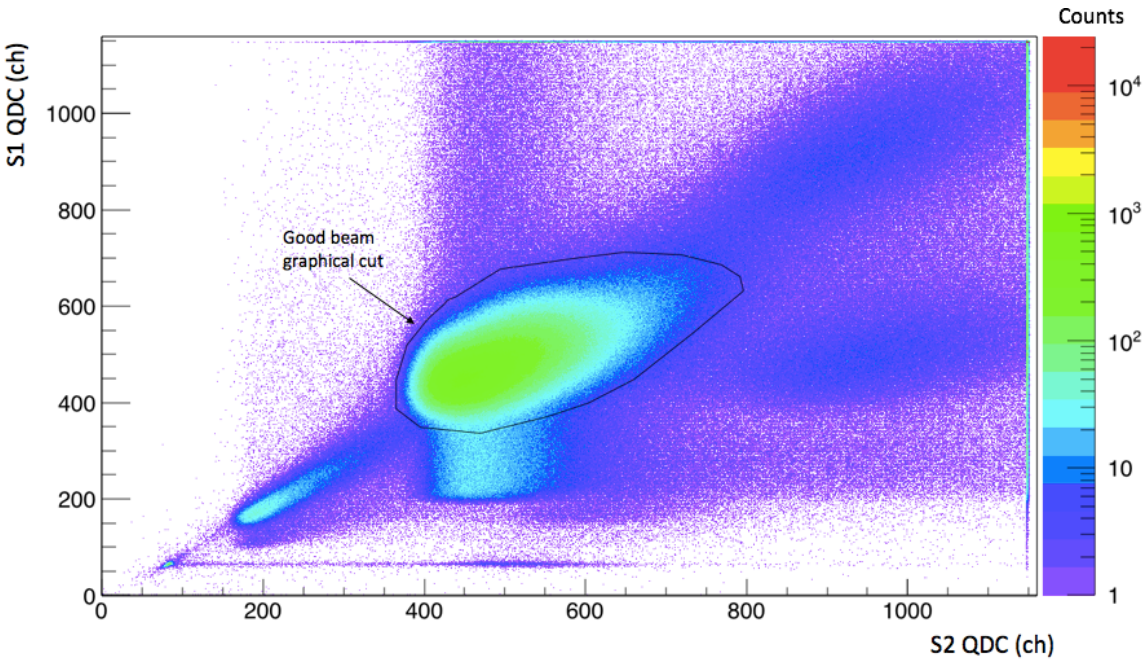


Figure 20. Charge deposited in S1 and S2 scintillators for 400 AMeV helium on all targets.

IV.3.3 Self-Time Gate

To create the self-time gates, one-dimensional TDC histograms for each liquid scintillator were plotted for all beam-target systems. The locations of the self-time peaks were noted and a cut was set on either side of the peak. Events that occurred outside of the self-time peak were considered mistimed events, or events that were detected in a liquid scintillator but did not set the coincidence trigger. While the number of mistimed events varied run to run, in general, approximately 75% or more of the events were mistimed at 10°, while 94% of events were mistimed at the remaining angles. No particle identification information was obtained using the self-time gate because both neutral and charged particle events could set the coincidence trigger in the liquid scintillators. Each gate width was less than or equal to 10 channels, which corresponded to a width of 2.38 ns or less. Since time increased from right to left due to the trigger system logic, the self-time peak shifted to the right as the angle of the liquid scintillator increased and the resulting particle flight path decreased. While the self-time peaks varied according to the location of the detectors, the peaks did not shift based on the selected beam-target system, resulting in six self-time gates (Figure 21).

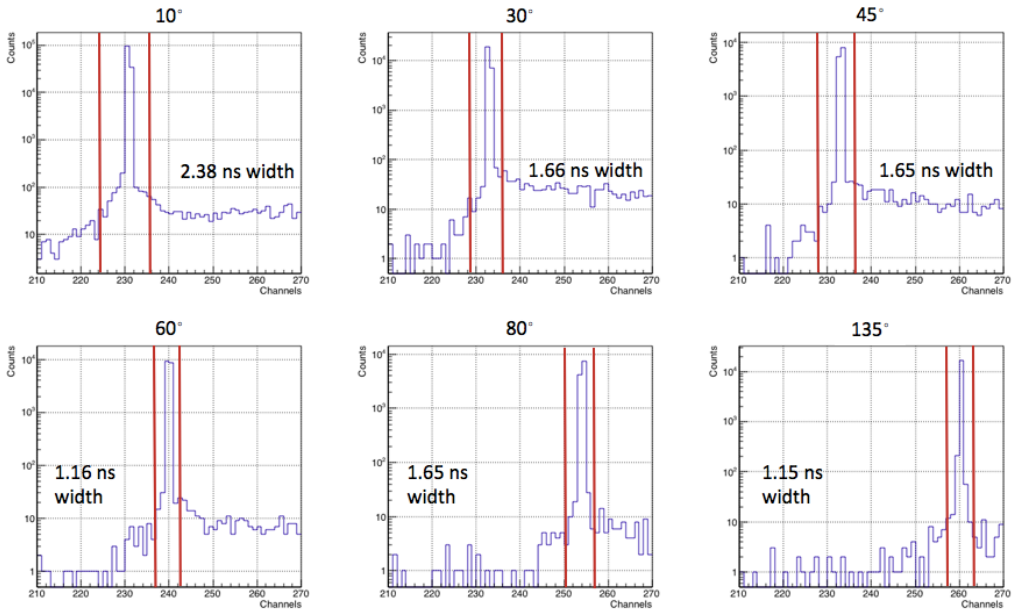


Figure 21. Liquid scintillator self-time peaks and gate widths for an 800-AMeV iron beam on 20 g/cm^2 aluminum target, no shadow bars.

IV.3.4 Neutral and Charged Particle Separation

Next, the neutral (neutrons and gammas) and charged particle event contributions that set the coincidence trigger in the liquid scintillators were separated using the two veto detectors. Due to the interaction mechanisms of neutral particles in thin media, the neutral particle event information was contained within the non-zero pedestal peaks whose locations were dependent upon the electronic noise processed event-by-event [64]. This meant any event that registered in the veto detector's pedestal and was subsequently detected in a scintillator was the result of a neutral particle interaction [12]. Events to the right of pedestal were considered charged particle events which were not utilized in this analysis. To create the veto gates, one-dimensional QDC histograms for each scintillator's two veto paddles were plotted for all beam-target systems. The locations of the pedestals were noted and a cut was placed to the right of the peak past the 3σ value of the pedestal centroid. All events to the right of this cut were thrown out. Once again, the pedestals varied by detector but they did not shift based on the selected beam-target system. A single cut for each veto detector was applicable for all beam-target systems, resulting in a total of twelve veto gates (Figure 22).

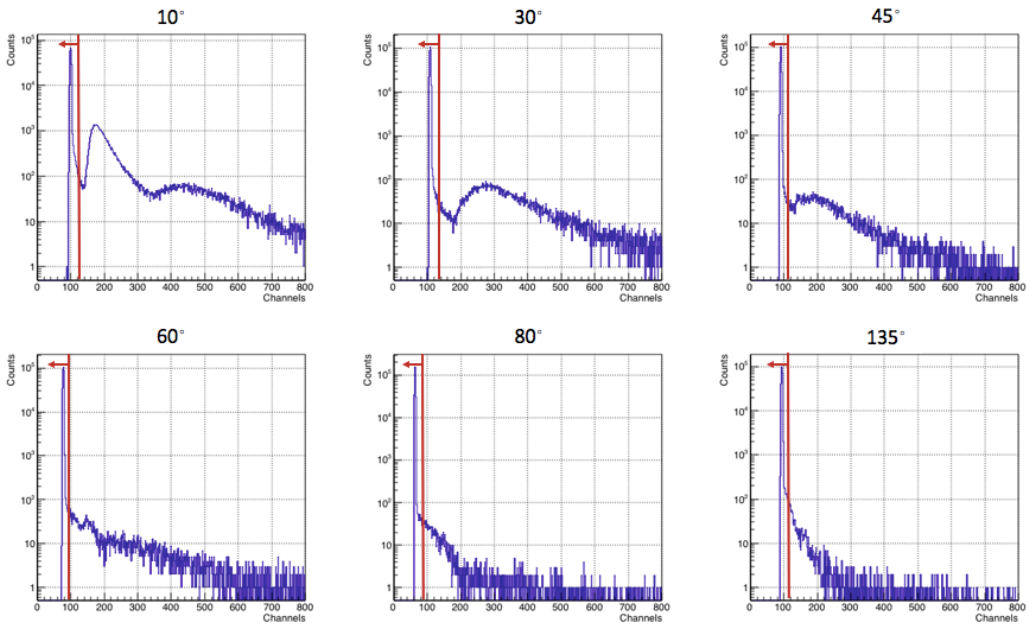


Figure 22. Front veto paddle QDC spectra with neutral particle pedestal cuts for an 800-AMeV iron beam on 20 g/cm^2 aluminum target, no shadow bars.

IV.3.5 Neutron – Gamma Discrimination

Neutral events were further separated into neutron and gamma events with the pulse shape discrimination (PSD) technique. Using the un-attenuated signal outputs from the PSD module, a two-dimensional charge deposition spectrum was constructed for each ion beam species. In each spectrum, the charge deposited in the first 20 to 35 ns of the signal (*h_qdc*) was plotted against the charge deposited in the entire signal (*t_qdc*), which resulted in clear separation between neutron and gamma events (Figure 23a). Gamma events were concentrated in the top line because more of their charge was contained in the fast component of the pulse, resulting in higher *h_qdc* channel values than the neutron events in the same *t_qdc* channel. Contrastingly, neutron events were represented by recoil protons and were found in the bottom line. Once the un-attenuated spectra were constructed, graphical cuts were used to separately select the neutron and gamma events. Events in the low-energy, unseparated region were excluded, while events in the high-energy, pileup region were examined later using the attenuated signals. One neutron cut and one gamma cut were made for each liquid scintillator with the un-attenuated signals.

a)

b)

c)

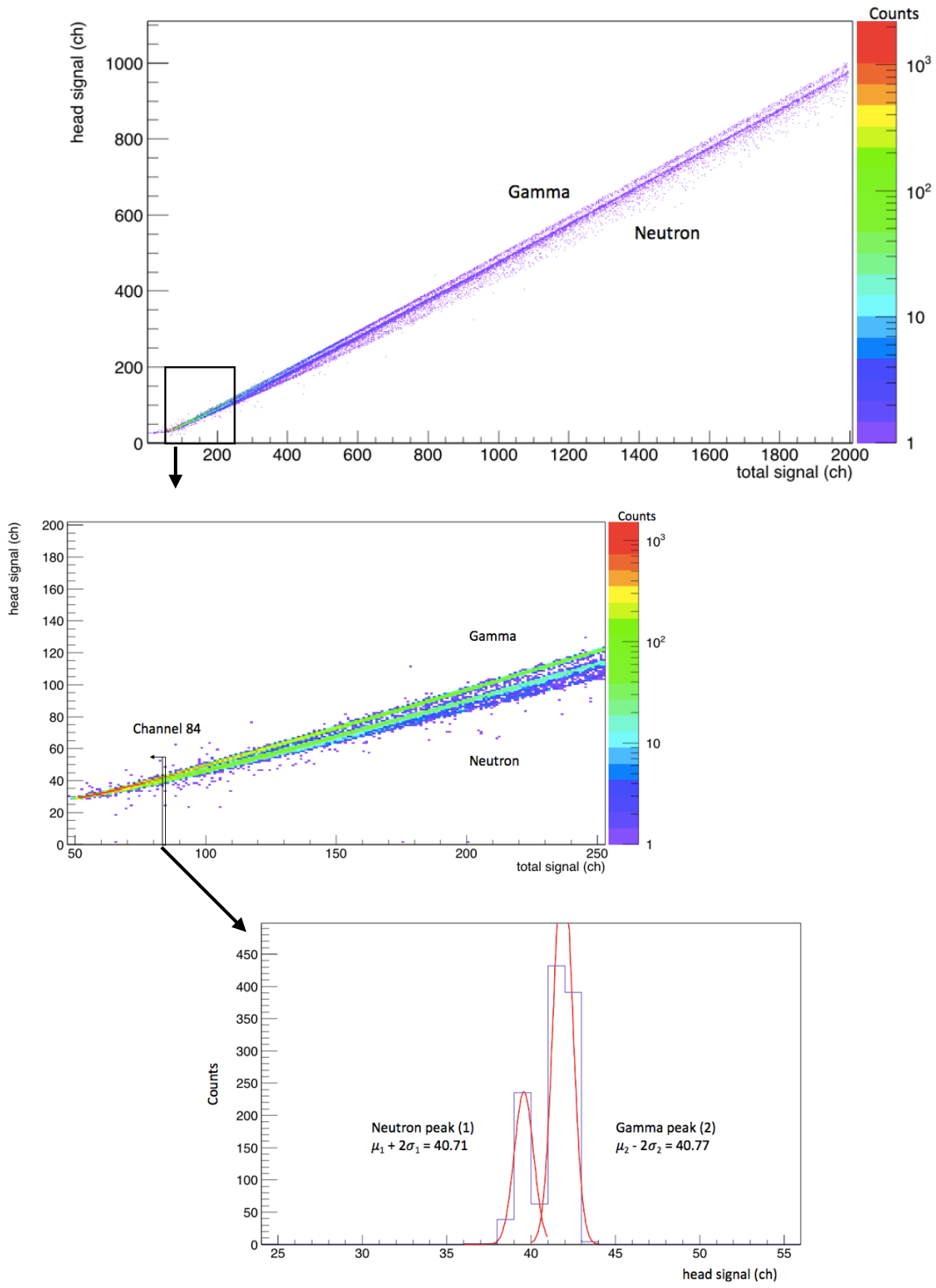


Figure 23. (a) Un-attenuated neutron and gamma PSD at 45° for 400 AMeV iron, pileup region excluded, in (b) the low energy separation region with (c) Y axis-projection of the neutron-gamma separation threshold at channel 84. Neutron and gamma peaks are fitted with Gaussian distributions and are well-separated at 2σ.

An additional analysis was performed near the neutron-gamma separation threshold for the un-attenuated signals (Figure 23b). Because a neutron can deposit up to its full energy in a single interaction, the energy at the neutron-gamma separation threshold represented the lowest energy neutron resolvable by PSD. By taking one-channel-wide slices of the PSD spectra and projecting the slices onto the y-axis, distinct neutron and gamma peaks were observed (Figure 23c). Both peaks were fitted with a Gaussian distribution and their standard deviations (σ) were calculated. The neutron and gamma events were considered well-separated if their 2σ values did not overlap. A 2σ separation was chosen because the separation in all subsequent channel slices above this threshold increased. The channel number of the threshold slice was first converted to electron-equivalent energy (MeVee) using the experimental calibration curves (Figure 17). Then it was converted to the proton recoil energy, which corresponded to the incident neutron energy (MeV), using a light output calibration based on [81] and [89]. The lowest resolvable neutron energy for each liquid scintillator is displayed in Table 8.

Finally, because the un-attenuated signals demonstrated pulse pileup at high energies, the neutron-gamma graphical cut procedure was repeated for the attenuated *h_qdc* and *t_qdc* signals gated on the un-attenuated signals' pile-up region. While pulse pileup with the attenuated signals was not observed at higher energies, the neutron and gamma lines appeared to merge (Figure 24). As previously mentioned, the main differences between proton and electron scintillation occurred in the slow component of the pulse, which was affected by the behavior of the particles near the end of their tracks. Because high-energy protons did not stop in the active volume and exited the liquid scintillators, their track structures were not distinguishable from that of the recoil electrons. At this point, all events were included in the neutron event gate. Gamma or high energy recoil proton events caught up in this gate were eliminated later because their times of flight were greater than or equal to the prompt gamma TOF. One neutron and one gamma cut was made for each liquid scintillator with the attenuated signal. To determine the total neutron and gamma event contributions in a liquid scintillator, *OR* logic was set between the gates made with the attenuated and un-attenuated signals. The gamma events were used to identify the prompt gamma peak while the neutron events were used in the TOF analysis.

Table 8. Lowest resolvable neutron energy with PSD in liquid scintillators

Liquid scintillator (angle)	Electron-Equivalent Energy (MeVee)	Neutron Energy (MeV)
10°	0.85	2.82
30°	0.96	3.09
45°	1.15	3.50
60°	0.40	1.71
80°	0.26	1.26
135°	0.26	1.26

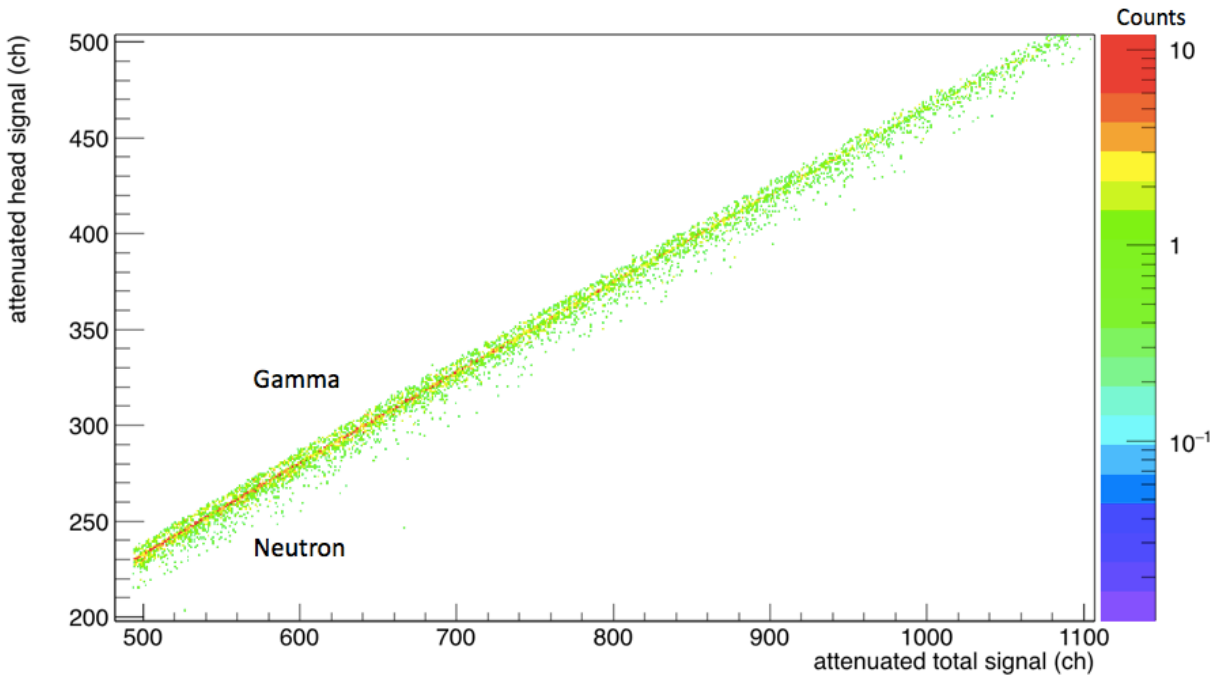


Figure 24. Attenuated neutron and gamma PSD at 45° for 400 AMeV iron gated on the pileup region of the un-attenuated signals.

IV.3.6 Pulse Height Gate

In addition to background subtraction, a pulse height gate was applied to help eliminate low energy, low pulse height background events near the neutron-gamma separation threshold. Using the un-attenuated total signal, a cut was set at a neutron energy above the lowest resolvable neutron energies found with PSD in Table 8. The energy of the pulse height gate was then converted to an electron-equivalent energy and finally a QDC channel number using the light output calibration and the experimental calibration curves, respectively [81], [89]. When the gate was applied, only neutron events with a pulse height above this channel number were accepted. Liquid scintillators at 10°, 30°, and 45° had a pulse height gate of 4 MeV (1.4 MeVee), while scintillators at 60°, 80°, and 135° had a pulse height gate of 2 MeV (0.51 MeVee). Differences in the pulse height gate between the forward and large angle detectors may be attributed to the differences in their scintillation material and the voltage settings.

IV.4 Source Particle Adjustment

Due to the use of shadow bars, multiple runs (run number denoted by "*i*" in equation 5) were taken for the same beam-target configuration. Adding these runs together thus improved the counting statistics for a given configuration. While individual runs typically acquired data for about an hour, the exact duration, system live time, and number of source particles varied for each run. Source particles were defined as the number of incident beam particles coincident between the two start scintillators (*s1.s2*) contained within the good beam gate (*GB*) that were recorded during the live time of the acquisition system (*LT*). Source particles varied run to run based on the behavior of the delivered beam. To combine multiple runs for a given beam-target configuration correctly, the yields ($N_{measured}$) were scaled by the source particles according to equation 5. After this correction was applied, each beam-target configuration now consisted of an un-shadowed and a shadowed dataset, instead of the original four or more runs. Yields were now expressed in units of neutrons per source particle (*# neutrons / S. P.*).

$$Yield = \frac{\sum_{i=1}^{n} \frac{N_{(measured)\mathrm{i}}}{LT_i}}{\sum_{i=1}^{n} GB_i \times (s_1 \cdot s_2)_i} \tag{5}$$

IV.5 Background Subtraction

Because the shadow bar completely blocked neutrons and gammas coming directly from the front target, any event that registered in the scintillator volume during a shadowed run was considered a background event. These background neutrons and gammas either crossed one of the side surfaces of the liquid scintillator, or they bypassed the shadow bar by scattering off the floor and entering the front face of the liquid scintillator, typically with a reduced energy. In the case of the forward-most angled liquid scintillators, neutrons and gammas produced in or reflected off the back target also contributed to the background events. For each beam-target configuration, the shadowed runs were subtracted from the un-shadowed runs to eliminate the background events on a per source particle basis. This meant the final energy spectra calculated using the time-of-flight technique were representative of the neutrons or gammas coming directly from the upstream target, and not background events that scattered into the scintillator.

IV.6 Prompt Gamma Peak Identification

During fragmentation reactions, gammas are created when the excited projectile and target fragments decay [19]. These prompt gammas were used as a timing reference for neutron events because their flight paths and velocity were constant and known, resulting in fixed times of flight. This meant the location of the prompt gamma peak for each beam-target configuration was needed before calculating neutron TOFs. Gamma events were isolated for a configuration by gating the background-subtracted S1 TDC data for a scintillator on the appropriate good beam, self-time, veto, gamma, and pulse height cuts, and then scaling the yields by the source particle adjustment. This resulted in a one-dimensional TOF histogram that displayed all gammas detected by the scintillator. The prompt gamma peak was fitted with a Gaussian distribution and the calculated centroid and standard deviation were recorded.

IV.7 Time-of-Flight Calculation

To create neutron TOF spectra, the one-dimensional S1 TDC data were filtered using a series of gates. Recall that the number of beam particles incident on the upstream target was narrowed using

a good beam gate. Subsequent events that set the coincidence trigger in one of six liquid scintillators but did not deposit energy in the veto detectors were considered valid neutral events. Application of the PSD discrimination neutron gate filtered out the gamma events while a pulse height gate eliminated low energy, low pulse height background neutrons. Once these gates were applied, individual runs were normalized to their proper number of source particles and background subtracted. Finally, prompt gamma peak centroids were identified for each beam-target configuration which served as a reference time for the neutron TOF analysis.

After undertaking these steps, the TDC channel number of each neutron event was converted to energy using relativistic kinematics. Each neutron event's TDC channel (tdc_n) was converted to a time of flight (t_n) with equation 6. While neutron TDC channels varied by event, the flight path (d) and TDC calibration (tdc_{cal}) varied by liquid scintillator, as seen in Sections IV.1.6 and IV.2.5. Prompt gamma peak centroids (tdc_γ) varied by the beam-target system. Because valid neutron events were slower than the prompt gammas, the neutron TOF was found by adding the difference between the timing of the neutron channel and prompt gamma centroid to the gamma TOF. Neutron times of flight were subsequently converted to neutron velocities (v_n) and kinetic energies (T_n) with equations 7 and 8. The speed of light (c) and neutron rest mass-energy (m_n) were constant at 30 cm/ns and 939.565 MeV/c^2, respectively.

$$\mathrm{t_n} = \frac{\mathrm{d}}{\mathrm{c}} + \left[\left(\mathrm{tdc_\gamma} - \mathrm{tdc_n}\right) \cdot \mathrm{tdc_{cal}}\right] \tag{6}$$

$$\mathrm{v_n} = \frac{\mathrm{d}}{\mathrm{t_n}} \tag{7}$$

$$\mathrm{T_n} = \left(\sqrt{\frac{1}{1-\left(\frac{\mathrm{v_n}}{\mathrm{c}}\right)^2}} - 1\right) \cdot \mathrm{m_n} \tag{8}$$

Calculations for a sample neutron event at channel 600 are shown below. In Figure 25, a 400 AMeV iron beam was incident upon a 60 g/cm^2 aluminum target and neutrons were measured at

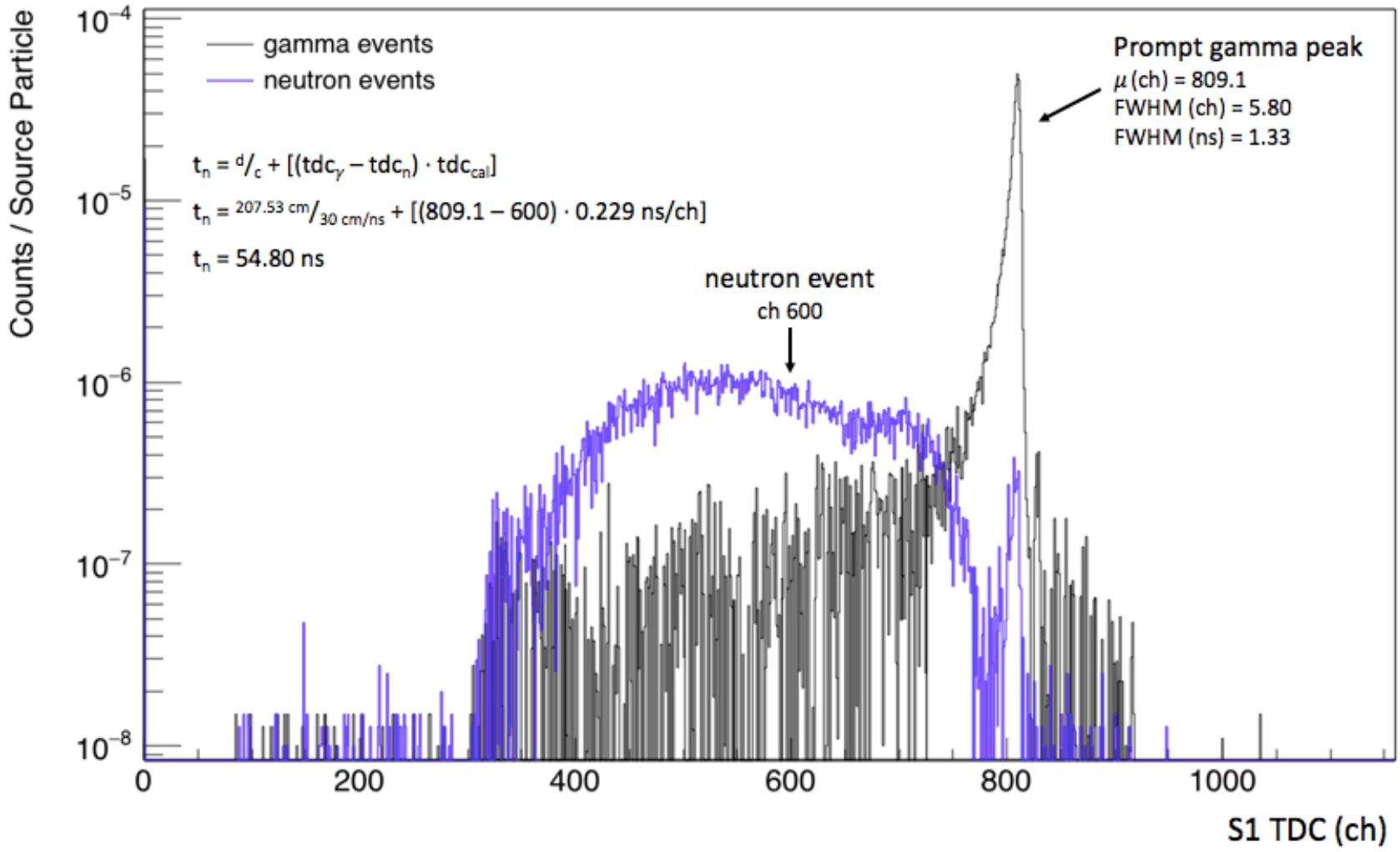


Figure 25. Neutron and gamma TOF spectra at 135° for 400 AMeV iron on 60 g/cm^2 aluminum. Neutron events 3σ to the left of the prompt gamma peak centroid and above are eliminated in the TOF analysis. Time increases right to left.

135°. Recall that time increased from right to left due to the selection of the trigger logic. For this scenario, the prompt gamma peak was located at channel 809.1 ± 2.46. Using equation 6 and the flight path and TDC calibration information for the 135° scintillator, the neutron TOF was calculated at 54.8 ns. This TOF was then converted to a velocity of 3.79 cm/ns (equation 7) and a kinetic energy of 7.58 MeV (equation 8).

IV.8 Correction Factors

IV.8.1 Efficiency Correction

Because neutrons do not continually lose energy as they traverse a medium like charged particles, liquid scintillators detect less than 100% of incident neutrons. An energy-dependent neutron detection efficiency correction was applied such that the measured yields were increased to reflect the true number of neutrons incident on the scintillator [84]. This correction factor was calculated using the SCINFUL-QMD Monte Carlo code [90]. SCINFUL-QMD expanded upon the SCINFUL and CECIL Monte Carlo codes by considering 39 possible neutron reaction channels and by incorporating quantum molecular dynamics (QMD) and statistical decay models (SDM) to replicate neutron interactions between 150 MeV and 3 GeV [90], [91]. As described by Satoh *et al.* [90], nuclear interactions for neutrons between the 10 keV cutoff energy and 150 MeV were modeled using an extended reaction cross section library. Depending upon the threshold energy and liquid scintillator size, SCINFUL-QMD generally agreed with experimentally-measured neutron detection efficiencies between approximately 3 and 134 MeV. At energies above 134 MeV, SCINFUL-QMD results were compared to efficiencies calculated with the established CECIL Monte Carlo code. Differences between these two codes were typically larger than differences between the SCINFUL-QMD calculations and experimental efficiencies, mostly due to the addition of pion-production reaction channels in SCINFUL-QMD and the incorrectly large cross section employed in CECIL for the $C(n, x\alpha)$ reaction. Because of the addition of new reaction channels and improved cross sections, SCINFUL-QMD calculations are considered more accurate than the CECIL-calculated efficiencies [90]. After calculating the scintillator response function, SCINFUL-QMD integrated the function above a given pulse height threshold to calculate the neutron detection efficiency as a function of energy (Figure 26) [90].

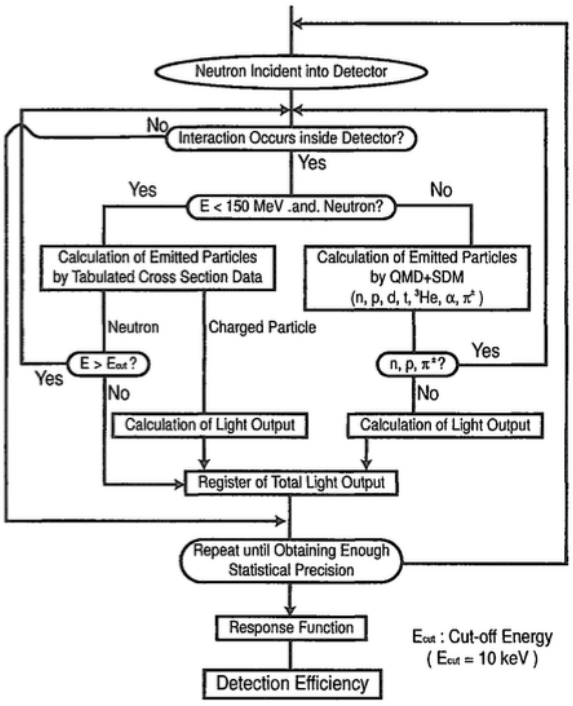


Figure 26. SCINFUL-QMD computational process [90].

Inputs to the code included scintillator type and dimensions, distance from the source to the active volume, light attenuation factor for the scintillator material, neutron energies, pulse height thresholds, and number of histories. A 12.7 cm diameter, 12.7 cm deep right cylindrical NE-213 organic liquid scintillator was selected as the scintillator type. Recall that EJ-301 is identical to NE-213 and that the active volume dimensions matched those of liquid scintillators used in March 2016. The distances from the source to the active volume were set equal to the distances from the center of the upstream target to the front face of the liquid scintillator's active volume, which was measured during the experiment.

The default light attenuation factor was used (8.0×10^{-3} cm^{-1}), and the SCINFUL-QMD calculations were performed for neutron energies ranging from 2 or 4 MeV to 3 GeV, depending upon the pulse height gate of the scintillator [92]. Detection efficiencies were calculated at the six scintillator locations for pulse height thresholds between 2 and 25 MeV, though not all were utilized during the analysis. Each calculation was performed for 10,000 histories and the energy-

dependent efficiencies were tabulated. Depending upon the energy of the measured neutron, the detection efficiency per energy bin was calculated via linear interpolation of the tabulated data. The yield in each bin was then divided by the neutron detection efficiency. Examples of the detection efficiencies for the 10° and 135° liquid scintillators are displayed in Figure 27.

IV.8.2 Solid Angle and Energy Bin Width Corrections

To directly compare the measurement yields to literature or Monte Carlo-simulated yields, results are often converted to double differential yields. Double differential yields are expressed in units of neutrons per source particle per solid angle steradian per energy (*# neutrons / S. P. / Ω / MeV*). This meant the efficiency- and source particle-adjusted yields were further normalized to energy bin width and the solid angle of the upstream target as seen by the scintillator. Energy bin width was calculated by finding the difference in the right and left edges of the energy bins, while the solid angle was estimated using equation 9. In this equation, *a* represents the radius of the scintillator and *d* is the flight path from the center of the upstream target to the center of the liquid scintillator. This estimation was used because *d* was significantly greater than *a* [84].

$$\Omega \cong \frac{\pi a^2}{d^2} \tag{9}$$

IV.9 Monte Carlo Simulations

IV.9.1 PHITS Overview

The Particle and Heavy Ion Transport Code System (PHITS) version 2.76 was utilized for a series of Monte Carlo simulations. As described in [29], PHITS used physics models and data libraries to simulate nuclear and atomic reactions between a wide range of particle species and heavy ions, and then transport said particles between collisions (Figure 28). Initial heavy-ion nuclear interactions between the iron projectiles and target materials were simulated using the JAERI Quantum Molecular Dynamics Model (JQMD) and an evaporation and fission model (GEM). The light ion- (proton and helium) induced reactions were better described using the INCL4.6

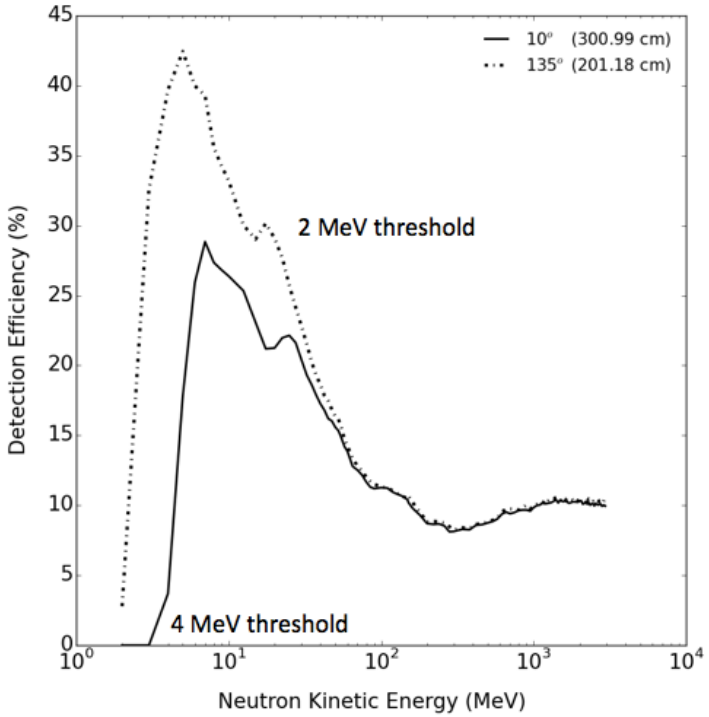


Figure 27. Neutron detection efficiency as a function of energy for a 12.7 cm by 12.7 cm cylindrical liquid scintillator at 10° and 135°, with pulse height thresholds of 4 and 2 MeV, respectively. Listed flight paths are to front surface of active volume.

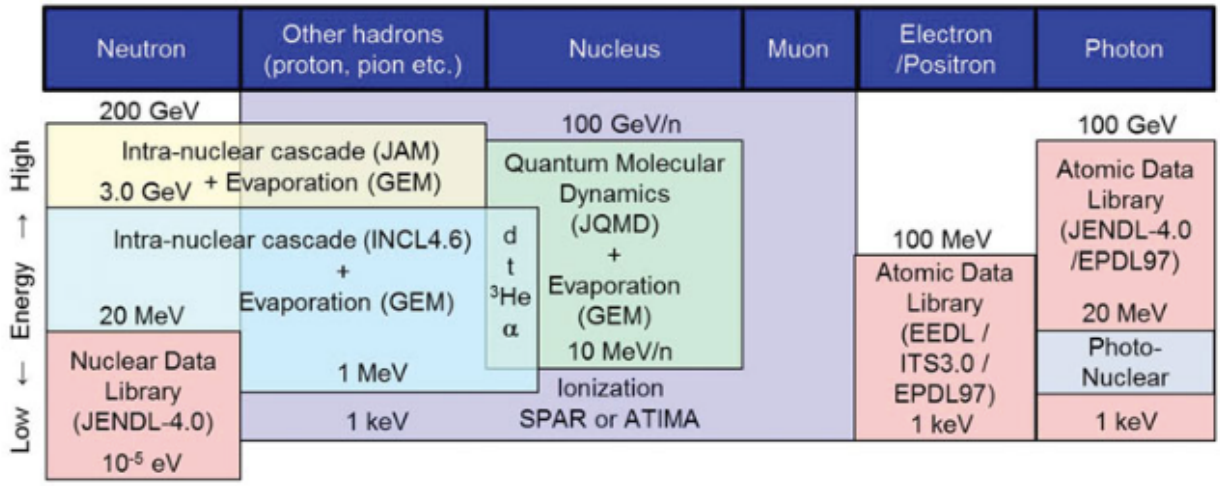


Figure 28. PHITS physics models for different particle species and energy ranges [29].

intranuclear cascade model to predict the abrasion and cascade stages of an interaction, in addition to GEM. Individual neutron interactions were simulated with the nuclear data library JENDL-4.0 below 20 MeV before transitioning to intranuclear cascade models. Charged particle stopping powers were calculated in SPAR with the continuous slowing down approximation. For the PHITS simulations, a cutoff energy of 1 keV was selected for protons, neutrons, photons, and heavy charged particles, while a cutoff energy of 100 keV was selected for electrons and positrons.

IV.9.2 Design of PHITS Benchmarking Simulations

Two geometry configurations were explored in PHITS to study the effect of room-scattered neutron yield contributions in the liquid scintillators. Simulations were conducted for each beam-target system studied in March 2016. First, the air-filled target room was modeled to include the floor, ceiling, interior and exterior walls, tunnel, room entrance, beam dump, rail system, and detector stands. Next, the veto detectors and liquid scintillators (including the aluminum housing) were placed in the room at 10º, 30º, 45º, 60º, 80º, and 135º off beam axis with their corresponding flight paths. A uniform beam with a diameter of 2.5 cm was placed 15 cm away from the center of the upstream target. The neutron flux as a function of energy was calculated for neutrons that crossed the front surface of the six liquid scintillators' aluminum housing and entered the active volumes (*neutrons / cm^2 / MeV / S. P.*), which is a PHITS T-Cross tally. This meant with each crossing neutron, the flux tally of the corresponding energy bin was increased by $1/\cos\theta$, where θ was the angle between the vector normal to the crossing surface and the direction of the incident neutron [29]. Detected neutrons could be produced anywhere in the room as long as they crossed the aluminum housing surface and entered the scintillator active volume. Simulations were run for 1.0×10^8 histories and upon completion, the outputs were divided by the solid angle of the detector (equation 9) to generate DDTT neutron yields.

A second simulation using a ring configuration was also executed in PHITS because the room configuration may have included neutrons that satisfied the T-Cross conditions but did not originate directly from the upstream target. These simulations were designed and executed by Hui-Chen Wang, a graduate student in UTK's Department of Nuclear Engineering and a collaborator

on the thick GCR shielding project. Six cylindrical rings with a width and depth equal to the liquid scintillator's active volume dimensions were established at the proper flight paths (Figure 29). This geometry configuration could be used because of the symmetric production of neutrons in the direction of the incident beam [22], which improved counting statistics. While the upstream and downstream targets were included in the ring configuration, target room features such as the walls, floor, and ceiling were not included, eliminating the sources of room-scattered neutrons. All targets and ring detectors were contained in air and the same source information described above were included. A *T-Cross* tally was established to count neutrons that exited the air-filled region in front of the ring and entered the ring detector, which also eliminated neutrons that were scattered off of or produced in the downstream target. Simulations were executed for 1.0×10^7 histories.

IV.9.3 MCNP Overview

Benchmarking simulations were also designed using Los Alamos National Laboratory's Monte Carlo N-Particle Transport code, MCNPX version 2.7 [28]. MCNP utilized the Cascade-Exciton Model (CEM03.02) and the Los Alamos Quark-Gluon String Model (LAQGSM03.03) event generators [93]. As described in [93] and [28], both models simulated nuclear reactions as a three-stage process starting with an intranuclear cascade model. In both models, primary particle interactions were tracked until their secondaries stopped or escaped the nucleus. CEM utilized an expansion of the time-independent, Dubna Cascade Model (DCM) while LAQGSM used the updated, time- dependent DCM. After the cascade stage, the emitted neutrons and protons coalesced to form light ions (deuterons, tritons, helium-3, and helium-4), while excited $A<13$ residual nuclei were inputted into a Fermi breakup model. The remaining nuclei ($A \geq 13$) were submitted to a pre-equilibrium particle emission model followed by an evaporation and fission model. All models, except the initial intranuclear cascades, were utilized by both the CEM and LAQGSM event generators.

The default CEM and LAQGSM physics model options were utilized for the MCNP benchmarking simulations [94]. CEM was used for reactions induced by nucleons and pions below 3.5 GeV, while LAQGSM modeled the remaining nucleon- and pion-induced reactions in addition to all

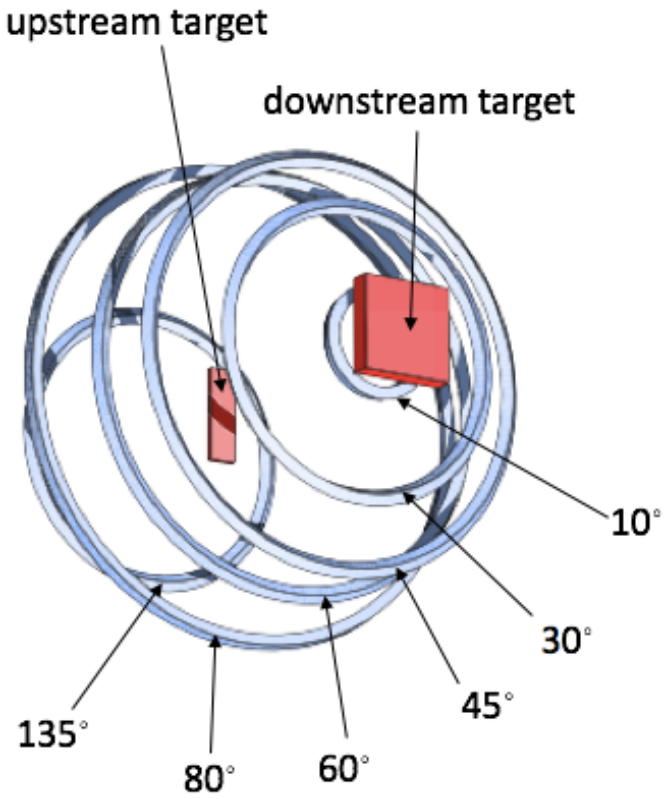


Figure 29. 3-dimensional representation of PHITS ring configuration with aluminum targets and six liquid scintillator rings [95].

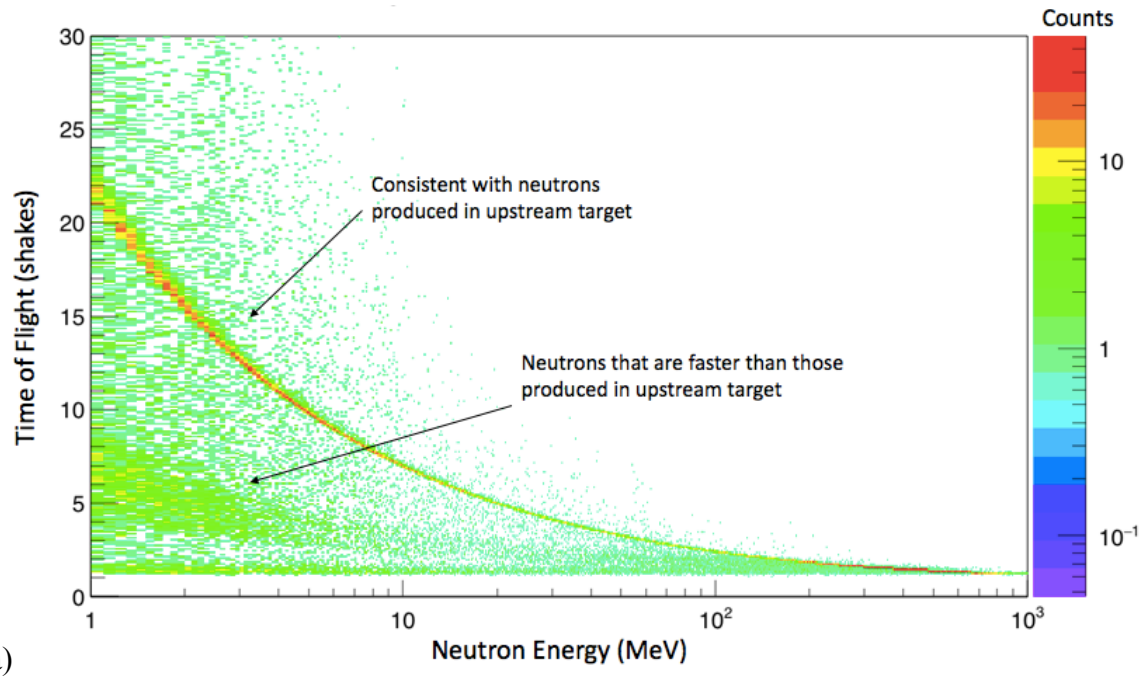
light and heavy ion-induced reactions [28]. CEM and LAQGSM were also used for photonuclear reactions below and above 1.2 GeV, respectively [28]. Protons, light ions, neutrons, and pions were tracked to 0 MeV while heavy ions were cutoff at 1 MeV [94]. Finally, neutrons, photons, and electrons were modeled using the ENDF data libraries below 150 MeV when available [28].

IV.9.4 Design of MCNP Benchmarking Simulations

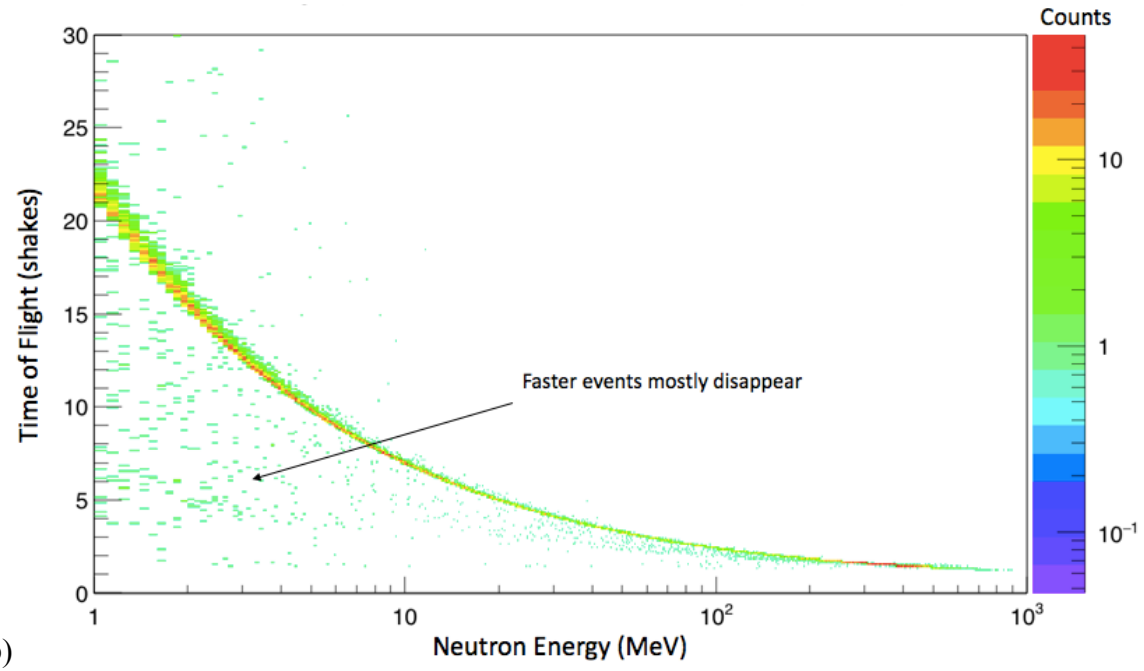
MCNP simulations were executed for each March 2016 beam-target system using a room geometry similar to the geometry modeled in PHITS. These simulations were designed and executed by Luis Castellanos, a graduate student in UTK's Department of Nuclear Engineering and another collaborator on the thick GCR shielding project. The neutron flux as a function of energy was calculated for neutrons that crossed the front face of the liquid scintillator active volumes (*neutrons / cm^2 / S. P.*), which is a MCNP F2 tally. The MCNP simulations were run for 1.0 x 10^7 histories for the iron projectiles and 1.0 x 10^8 particles for the proton and helium projectiles. Output results were later divided by the energy bin width and multiplied by the flight path squared to generate DDTT neutron yields.

Additionally, the "surface source write" card (SSW) in each simulation was utilized to eliminate the neutrons not produced in the upstream target. This option recorded the energy, weight, time, particle identification, position, direction, and k-value ($k = |cos\theta|$) for every neutron track that crossed a specified surface and entered a volume of interest [96]. The SSW card was executed simultaneously with the room geometry simulations, indicating that the SSW card could then be applied to the room geometry results to generate two sets of useful data from a single simulation. The SSW card recorded all neutrons that crossed the front face of and entered the scintillator active volume, as well as all neutrons moving in the opposite direction [94]. Neutron track information was then translated from binary to plain text and inputted into ROOT for manipulation [94], [97]. This task was also completed by Mr. Castellanos.

Time versus energy spectra were constructed for the neutrons detected at the six liquid scintillator positions for each beam-target system. Figure 30a is a representative spectrum showing the 800 AMeV iron projectiles incident on 20 g/cm^2 of aluminum at 10º. Recall that this beam punched



a)



b)

Figure 30. (a) Neutron time of flight versus energy for 800 AMeV iron projectiles incident on 20 g/cm^2 aluminum at 10°, (b) excluding all neutrons with k<0.97. Results calculated using MCNP. 1 shake is equivalent to 10 ns.

through the upstream target and stopped in the downstream target (Table 5). The prominent curved feature present in all spectra aligned with TOF calculations for neutrons produced in the upstream target. At 10º, a group of low-energy neutrons appeared below the line of upstream target-produced neutrons. Based on their proximity to the downstream target and their times of flight, these low-energy neutrons were produced by primary beam interactions in the downstream target. This group were not as prominent with the 400 AMeV iron beam because the beam fully stopped in the upstream targets. As the angle of detection increased, the TOFs for the downstream target-produced neutrons lengthened due to the increased distance between the downstream target and scintillators. Eventually, these neutrons appeared above the line of upstream target-produced neutrons.

To eliminate neutrons that were not produced in the upstream target in these simulations, the author placed a restriction on the cosine of the angle between the vector normal to the crossing surface and the direction of the incident neutron track. The angular acceptance of the scintillators was approximately ±1.2º from the center of the scintillator's surface, which corresponded to a *k*-value of 0.999. For the data cut, a more relaxed *k*-value of 0.97 was selected which corresponded to an angular acceptance of about ±7.0º [94]. This restriction effectively eliminated most neutrons that were not produced in the upstream target (Figure 30b). Additionally, the author took a ROOT graphical cut around the neutrons produced in the upstream target. The k>0.97 restriction was combined with the graphical cut to form the neutron directionality correction, which was then applied to the MCNP DDTT yields calculated with the room geometry. Neutron events that only originated from the upstream target were thus read out for comparison to the experimental data.

V. RESULTS AND DISCUSSION

V.1 Prompt Gamma Peak Identification

Despite background subtraction, multiple gamma peaks were found in each scintillator. The centroids of all peaks were found by fitting them with a Gaussian distribution in ROOT. For most cases, a preliminary prompt gamma peak was easily identified based on its relatively high intensity when compared to surrounding peaks. A time of flight (TOF) for this peak was calculated using the flight paths for each scintillator. Due to the reverse timing of the TDC module, peaks that appeared to the left of the peak were slower than the prompt gammas, indicating that they most likely originated from the back target or other downstream sources that were not blocked by the shadow bar system. Peaks to the right of the prompt gamma peak had a faster TOF than the prompt gammas and subsequently originated from upstream locations in the target room. The TOF of these faster gamma peaks were calculated by subtracting the timing difference between the prompt and extra gammas, and then comparing the resulting TOF to TOFs from potential upstream target room sources.

A computer rendering of the room was created which included the walls, liquid scintillators, targets, and start scintillators. Assuming no energy loss between the beam exit window and the upstream target, the beam travel time was backtracked from the upstream target to the start scintillators and the beam exit window. Gamma TOFs from the start scintillators and the beam exit window were then calculated and compared to the TOFs of the extra peaks.

It was determined that the incident beam species had the largest effect on shape of the gamma TOF spectra. For the 400 AMeV iron beam, a small peak to the right of the prompt gamma peak at 45°, 60°, 80°, and 135° originated from the start scintillators. At 135°, the farthest peak from the right originated somewhere along the beam line between the start scintillators and the beam exit window (Figure 31). One possible source was the beam profile monitor seen in Figure 32. Similarly, the extra peak observed with the 800 AMeV iron spectrum at 135° was traced back to the beam exit window (Figure 33).

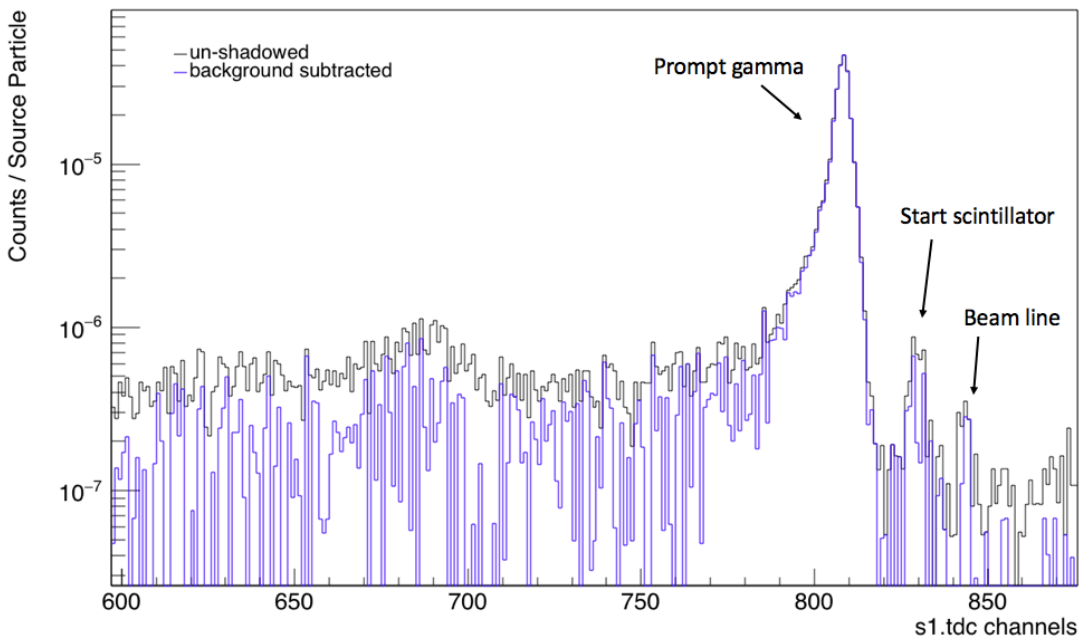


Figure 31. Un-shadowed and background-subtracted gamma TOF spectra for 400 AMeV iron beam on 20 g/cm^2 aluminum at 135°.

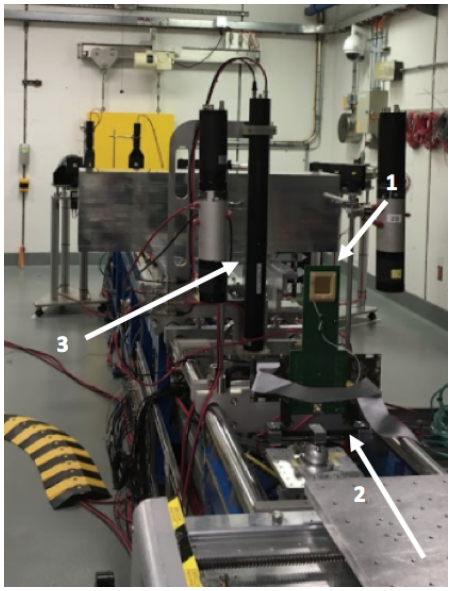


Figure 32. Possible source of smallest gamma peak observed at 135° with 400 AMeV iron projectile (beam profile monitor, 1), located between the beam exit window (off-camera, 2) and the start scintillators (3).

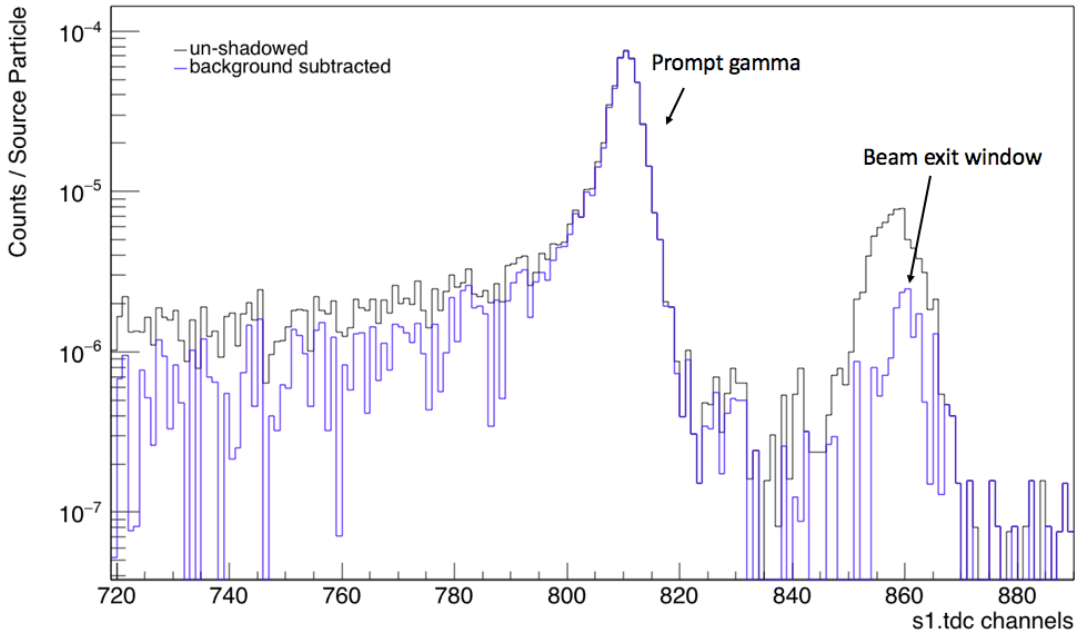


Figure 33. Un-shadowed and background-subtracted gamma TOF spectra for 800 AMeV iron beam on 20 g/cm^2 aluminum at 135°.

For the proton and helium beams, one or two peaks to the left of the preliminary prompt gamma peak at 10° and 30° did not fully disappear with background subtraction. In some cases, the intensities of the extra peaks were similar to or greater than the intensity of the prompt gamma peak. All proton and helium beams used in this experiment punched through the upstream target, resulting in gamma production by primary beam interactions in the downstream target. After taking the beam travel time into consideration, the left-most peak's TOF in the 10° scintillator indicated it originated from the back target, while the middle peak originated from gammas produced in the air column between the upstream and downstream targets (Figure 34). In the 30° scintillator, the air column peak was not visible, due to the increased distance between the scintillator and air column.

After the extra peaks were identified, the prompt gamma peak centroids were recorded and the FWHM were calculated (Table 9 to Table 11). These peak centroids were used in the neutron TOF analysis. For most of the beam-target systems, the FWHM values increased as the upstream target

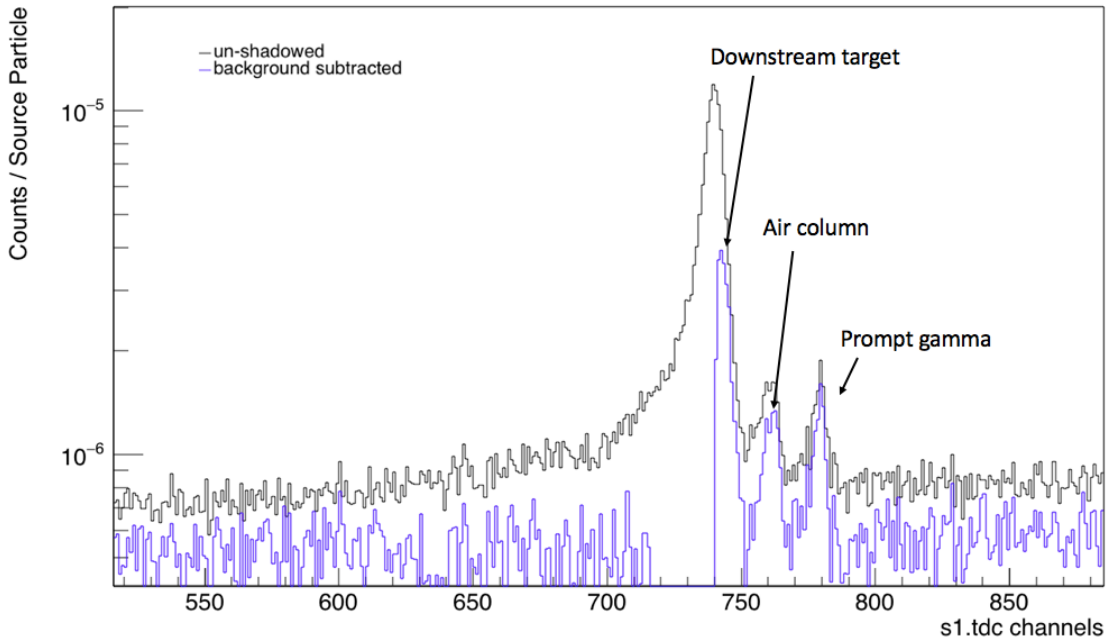


Figure 34. Un-shadowed and background-subtracted gamma TOF spectra for 400 MeV proton beam on 20 g/cm^2 aluminum at 10°.

Table 9. Prompt gamma peak centroids and FWHMs for all beams on 20 g/cm^2 aluminum target.

Detector angle	Centroid (channel), FWHM (ns)				
	400 AMeV Fe	**800 AMeV Fe**	**400 MeV H**	**400 MeV H**	**400 AMeV He**
10°	775.3 0.82	777.9 1.06	779.4 1.22	781.2 1.32	789.4 0.81
30°	767.5 0.73	770.4 0.88	770.1 0.87	772.6 1.19	781.6 0.71
45°	768.9 0.79	771.7 0.85	771.5 1.23	773.6 0.98	783.0 0.85
60°	796.4 0.93	798.7 0.93	800.2 1.16	801.9 1.19	810.6 1.07
80°	792.4 1.00	795.3 1.05	795.1 1.18	797.7 1.27	806.8 1.16
135°	808.2 1.04	810.5 1.13	811.0 1.34	812.9 1.02	822.4 1.06

Table 10. Prompt gamma peak centroids and FWHMs for all beams on 40 g/cm^2 aluminum target.

Detector angle	Centroid (channel), FWHM (ns)				
	400 AMeV Fe	**800 AMeV Fe**	**400 MeV H**	**800 MeV H**	**400 AMeV He**
10°	775.3 0.89	777.9 1.13	779.4 1.34	781.2 1.33	789.4 0.84
30°	767.5 0.92	770.4 0.93	770.1 1.07	772.6 1.12	781.6 0.84
45°	768.9 0.91	771.7 1.03	771.5 1.13	773.6 0.97	783.0 0.89
60°	796.4 1.07	798.7 1.06	800.2 1.24	801.9 1.19	810.6 1.09
80°	792.4 1.01	795.3 1.18	795.1 1.19	797.7 1.29	806.8 1.13
135°	808.2 1.21	810.5 1.36	811.0 1.47	812.9 1.26	822.4 1.32

Table 11. Prompt gamma peak centroids and FWHMs for all beams on 60 g/cm^2 aluminum target.

Detector angle	Centroid (channel), FWHM (ns)				
	400 AMeV Fe	**800 AMeV Fe**	**400 MeV H**	**800 MeV H**	**400 AMeV He**
10°	775.3 0.93	777.9 1.15	779.4 1.71	781.2 1.27	789.4 0.88
30°	767.5 0.96	770.4 1.09	770.1 1.12	772.6 1.15	781.6 0.79
45°	768.9 0.94	771.7 1.14	771.5 0.99	773.6 1.05	783.0 0.97
60°	796.4 1.19	798.7 1.21	800.2 1.53	801.9 1.26	810.6 1.14
80°	792.4 1.39	795.3 1.39	795.1 1.23	797.7 1.38	806.8 1.33
135°	808.2 1.33	810.5 1.65	811.0 1.41	812.9 1.39	822.4 1.48

thickness increased from 20 to 60 g/cm^2. An increase in upstream target thickness resulted in increased locations along the center line of the target for the primary beam to interact and produce gammas. In turn, this increased the distribution of prompt gamma flight paths and subsequent TOFs, resulting in wider FWHMs. Overall, the FWHM values ranged from 0.71 to 1.32 ns, 0.84 to 1.34 ns, and 0.79 to 1.71 ns for systems with the 20, 40, and 60 g/cm^2 aluminum targets, respectively. Prompt gamma peak FWHM values were later utilized when calculating the energy resolution of the measured neutron spectra.

V.2 Uncertainty Calculations for Experimentally Calculated Yields

V.2.1 Statistical Uncertainties

Statistical uncertainty in the double differential thick-target (DDTT) neutron yields were Gaussian-distributed and varied by energy bin. For each shadowed or un-shadowed dataset, the uncertainties per bin were calculated by taking the square root of the number of counts in the bin and then scaling the error by the source particle adjustment (equation 5). Next, the fractional statistical uncertainties for the shadowed ($\sigma_{subtract}$) or un-shadowed (σ_{add}) dataset corresponding to a particular beam-target system were added in quadrature to account for background subtraction (equation 10). Uncertainties were improved by rebinning the data to at least the FWHM of the prompt gamma peak, which represented the lowest energy resolvable by the liquid scintillator. In general, the data were rebinned such that improvements in the statistical uncertainties were balanced with the number of points needed to represent all energy regions of the spectra.

$$\sigma_{net} = \sqrt{\sigma_{add}^2 + \sigma_{subtract}^2} \tag{10}$$

Statistical uncertainties varied by target thickness, angle, energy, and projectile beam species. As the target thickness increased from 20 to 60 g/cm^2, the uncertainties generally decreased at all neutron energies due to the increased production of secondary neutrons in the thicker targets. Median statistical uncertainties were generally higher at 10°, 45°, and 80°, especially for neutrons with energies below approximately 120 MeV. Uncertainties in this neutron energy region were

highly beam-dependent, with proton and iron projectile beams registering the highest and lowest uncertainties, respectively. In general, statistical uncertainties were higher when the incident projectile beam penetrated the upstream target and interacted in the downstream target, creating an additional source of background neutrons seen by the forward angled scintillators. These downstream target-produced neutrons appeared at intermediate energy ranges in the TOF spectra. For example, 800 MeV protons lost the least amount of energy per nucleon when penetrating the 20 g/cm^2 upstream aluminum target, which made the downstream target produced neutrons appear at higher energies when compared to penetrating beams that lost more energy per nucleon. As such, 10 to 20 MeV neutrons produced in the downstream target with this system would appear in the neutron TOF spectra with approximate energies between 80 and 118 MeV. Uncertainties at 135° were the lowest overall.

At 10°, neutrons produced by the 400 AMeV iron beams had median statistical uncertainties of approximately 4.5% for all thicknesses of aluminum, with maximum uncertainties below 19% (20 g/cm^2) and 9% (40 and 60 g/cm^2). For the 800 AMeV iron beam that punched through the upstream aluminum target (20 g/cm^2), the median statistical uncertainty was near 26% with a maximum uncertainty of 43%. Neutrons created by the 800 AMeV iron projectiles that stopped in the 40 and 60 g/cm^2 aluminum targets had median uncertainties of about 8%, with maximum uncertainties below 14%. The 400 MeV proton beams penetrated all aluminum target thicknesses and registered the worst statistical uncertainties at the forward-most angle. Median uncertainties were approximately 28% (20 g/cm^2) and 13% (40 and 60 g/cm^2), with maximum statistical uncertainties ranging up to 53%. For the remaining beams that penetrated the upstream targets (800 MeV proton and 400 AMeV helium), the median statistical uncertainties were near 18% (20 g/cm^2) and 10% (40 and 60 g/cm^2), while maximum statistical uncertainties ranged up to 27% (20 g/cm^2) and 20% (40 and 60 g/cm^2).

At 30°, 45°, and 60°, the median uncertainties for the iron beams were approximately 10% (20 g/cm^2) and 7% (40 and 60 g/cm^2), with maximum uncertainties ranging from 13 to 35% (20 g/cm^2) and 7 to 14% (40 and 60 g/cm^2). With all target thicknesses, a few outliers were noted with statistical uncertainties between 16 and 71%. For the proton and helium beams, the median

uncertainties were approximately 13% (20 g/cm^2) and 10% (40 and 60 g/cm^2), and the maximum uncertainties ranged from 15 to 29% (20 g/cm^2) and 10 to 25% (40 and 60 g/cm^2). Several outliers for all target thicknesses were noted either below <20 MeV or at the highest energy bins, with fractional uncertainties ranging up to 59%.

Median uncertainties ticked slightly upwards for all projectile beams at 80° and were smallest at the back angle of 135°. Iron projectiles at 80° had median uncertainties near 14% (20 g/cm^2) and 12% (40 and 60 g/cm^2), with maximum uncertainties ranging from 13 to 20% (all thicknesses). A couple outliers were recorded at the highest energy bins and extended up to 58% uncertainty. The proton and helium projectiles had approximate median uncertainties of 13% (20 g/cm^2) and 14% (40 and 60 g/cm^2), with maximum uncertainties ranging from 12 to 23% (all thicknesses). Similar to the iron projectiles, a few outliers were recorded at the highest energy bins and extended up to 47% uncertainty. At 135°, iron projectiles had median uncertainties near 4.5% (20 g/cm^2) and 2.5% (40 and 60 g/cm^2). The proton and helium projectiles had approximate median uncertainties of 6.5% (20 g/cm^2) and 4.8% (40 and 60 g/cm^2). Depending upon the beam-target system, the statistical uncertainties for the highest energy bin ranged from 5 to 19%. Below the highest energy bin, all uncertainties were lower than 7.5%.

Statistical uncertainties in PHITS and MCNP also varied depending upon the detected neutron energy, angle, target thickness, and projectile beam species. In general, uncertainties were best below the high-energy peak and at more forward angles, and they improved as the target thickness increased. Additionally, statistical uncertainties were best for the simulations with the iron projectiles, followed by the helium and proton projectiles. The PHITS ring simulations had the lowest uncertainties, followed by the room geometries modeled in PHITS and MCNP. Maximum statistical uncertainties below the high-energy peak ranged from approximately 3 to 20%, 6 to 20%, and 10 to 30% for the PHITS ring, PHITS room geometry, and the MCNP simulations, respectively. Above the beam peak, uncertainties steadily increased, oftentimes reaching 100% uncertainty at the highest energy bins. Statistical uncertainties could be improved by running the simulations with a larger number of source particles.

V.2.2 Systematic Uncertainties

Systematic uncertainties in the yields were also considered (Table 12). Because neutrons originated from anywhere along the centerline of the upstream target and were detected anywhere within the liquid scintillator active volume, the solid angle uncertainty was calculated based on the solid angle extremes. The fractional uncertainty in solid angle was found according to equation 11. Recall that the true solid angle (Ω) was calculated for a neutron produced at the center of the upstream target and detected at the center of the liquid scintillator active volume. The maximum (Ω_{max}) and minimum ($\Omega_{\min}$) solid angles were calculated with the shortest and longest flight paths, respectively. For the 10°, 30°, 45°, 60°, and 80° scintillators, the Ω_{max} was calculated for a neutron produced at the downstream surface of the first target and detected at the front of the scintillator active volume. The quantity Ω_{min} was calculated for a neutron produced at the upstream surface of the first target and detected at the end of the active volume. For the back-angled scintillator at 135°, Ω_{max} was calculated for a neutron produced at the upstream surface of the first target and detected at the surface of the active volume, while the Ω_{min} was calculated for a neutron produced at the downstream surface of the first target and detected at the end of the active volume. Uncertainties in solid angle increased as target thickness increased and ranged from 5.4 to 13.8%.

$$\frac{\delta_\Omega}{\Omega} \cong \frac{(\Omega_{\max} - \Omega_{\min})/\,\Omega}{2} \tag{11}$$

Table 12. Systematic uncertainties for liquid scintillators.

Liquid Scintillator (angle)	Solid Angle Uncertainty for 20, 40, and 60 g/cm^2 (%)	Efficiency Uncertainty (%)	Good Beam Graphical Cut Uncertainty (%)
10°	6.5, 8.9, 11.3	10.2	400 AMeV Fe: 1.3 800 AMeV Fe: 5.6 400 MeV H: 2.8 800 MeV H: 5.7 400 AMeV He: 1.6
30°	6.2, 8.3, 10.4		
45°	5.8, 7.6, 9.3		
60°	6.4, 7.8, 9.2		
80°	5.4, 5.9, 6.4		
135°	8.7, 11.2, 13.8		

Uncertainty in neutron detection efficiency was calculated using the data presented in Figure 4 in [90]. The efficiency uncertainty was estimated by averaging the percent difference between efficiencies calculated experimentally and with SCINFUL-QMD. The average neutron detection efficiency uncertainty was 10.2%. Finally, due to the subjective nature of the good beam graphical cuts taken in ROOT, it was important to re-analyze the final data with a new set of good beam graphical cuts. To minimize author bias, another member of the analysis team took the new set of graphical cuts. Then, the absolute percent difference between the total integrated DDTT neutron yields found with the original and new graphical cuts were calculated and averaged for each beam. Uncertainty in the graphical cuts ranged from 1.3 to 5.7%.

A total systematic uncertainty was reported for each energy bin by adding the solid angle, neutron detection efficiency, and good beam graphical cut uncertainties. These uncertainties were not characterized by an underlying statistical distribution, and instead, represented a range that the normalized data fit within. Fractional systematic uncertainties ranged between approximately 16 and 30%. Systematic uncertainties dominated the statistical uncertainties for approximately 92% of all energy bins, indicating that only about 8% of the data had fractional statistical uncertainties above 30%. In these cases, statistical uncertainties dominated systematic uncertainties at low to intermediate energies, particularly at 10° with the 20 g/cm^2 aluminum target. This was most likely due to the 10° scintillator's proximity to the downstream target and beam dump. Additionally, 59% of all energy bins had fractional statistical uncertainties less than or equal to 10%.

V.2.3 Energy Resolution

The fractional energy resolution $(\Delta T/T)$ in equation 13 was determined by taking the partial derivative of equation 8 with respect to flight path and time, and then propagating the error according to equation 12. Values that varied with energy bin included the neutron kinetic energy (T), velocity-dependent β factor $(\beta = v_n / c)$, and neutron time of flight (t). Neutron flight path (d) varied with scintillator location and the rest mass-energy of a neutron (m) was constant at 939.565 MeV/c^2. The following methods were used to estimate the timing (Δt) and flight path (Δd) resolutions of the scintillators.

$$\Delta T^2 = \left(\frac{\partial T}{\partial d}\right)^2 \cdot \Delta d^2 + \left(\frac{\partial T}{\partial t}\right)^2 \cdot \Delta t^2 \quad (12)$$

$$\frac{\Delta T}{T} = \frac{T+m}{T} \cdot \frac{\beta^2}{1-\beta^2} \cdot \sqrt{\left(\frac{\Delta t}{t}\right)^2 + \left(\frac{\Delta d}{d}\right)^2} \quad (13)$$

Timing resolution was taken as half of the FWHM of the observed prompt gamma peak in the TOF spectra. Due to the thickness of the targets and variability in gamma production points, the timing resolution was dependent upon the flight paths of the prompt gammas. To decouple the timing and flight path resolutions, the FWHM values for a given beam-scintillator system were plotted for each target thickness. A linear trend line was fit to the data and the y-intercept of this fit represented the FWHM of a prompt gamma peak with 0 g/cm^2 target thickness (Figure 35). The best fit was selected for each scintillator and the results were recorded in Table 13. The average of the six timing resolutions was equal to 0.795 ns, which was similar to the intrinsic timing resolution seen in cobalt-60 coincidence studies with 12.7 cm by 12.7 cm EJ-301 liquid scintillators with no target [98].

The timing resolution was better for scintillators with a longer flight path (Table 13). The 10°, 30°, and 45° scintillators had approximate flight paths of 300 cm and demonstrated the lowest timing resolutions. As the flight path decreased to 250 cm (60° and 80°) and 200 cm (135°), the resolution worsened. This was expected because a decrease in flight path resulted in less separation of high-energy neutrons. The fractional timing resolution ($\Delta t/t$) varied with each energy bin for a given beam-target configuration, worsening as the neutron energy increased and the TOF decreased.

Next, the flight path resolution was determined using a method similar to the solid angle uncertainty calculation (equation 11). Flight path resolutions were not dependent upon neutron energy or incident beam species, but did vary based on target thickness and scintillator angle (Table 13). The fractional flight path resolutions ($\Delta d/d$) worsened as the target thickness increased from 20 to 60 g/cm^2 at all angles. These uncertainties were best for the scintillator at 80° because the

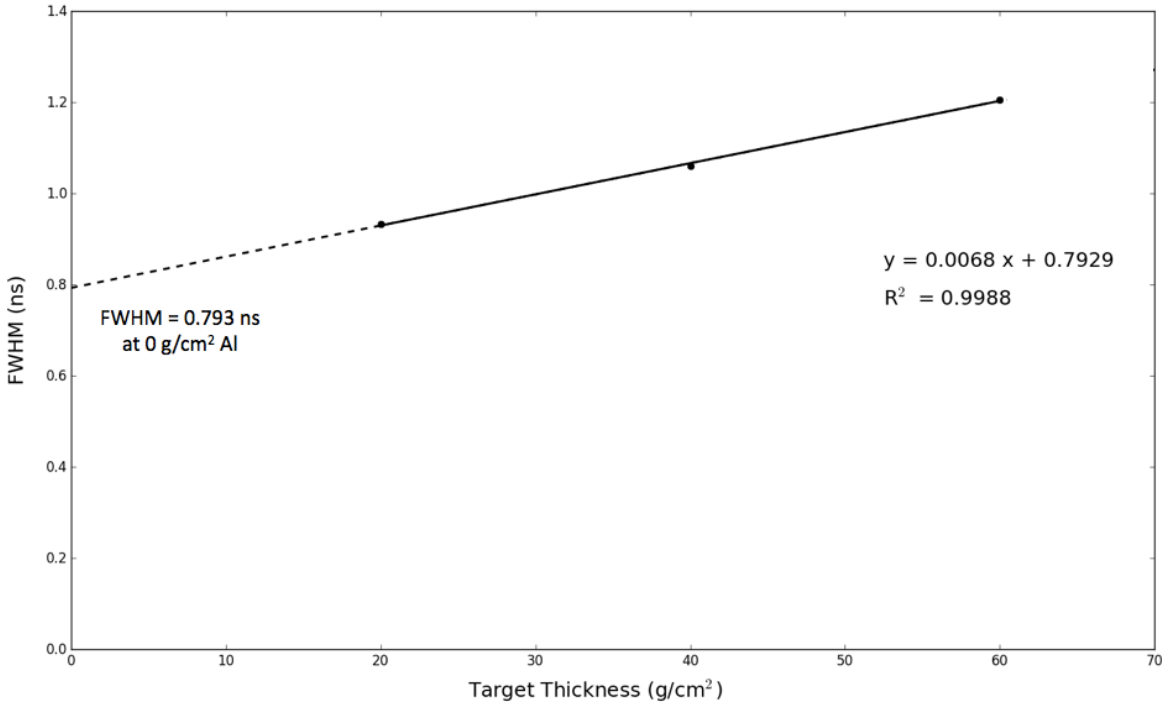


Figure 35. FWHM linear fit for 800 AMeV iron on aluminum targets at 60°.

Table 13. Timing resolutions and fractional flight path resolutions for liquid scintillators.

Scintillator (angle)	FWHM [2·Δt] (ns)	Δd/d for 20, 40, and 60 g/cm^2 (%)
10°	0.767	3.3, 4.4, 5.6
30°	0.760	3.1, 4.2, 5.2
45°	0.722	2.9, 3.8, 4.6
60°	0.793	3.2, 3.9, 4.6
80°	0.862	2.7, 3.0, 3.2
135°	0.865	4.3, 5.6, 6.8

flight paths from the upstream and downstream faces of the front target had the smallest difference, and they were worst for the scintillator at 135°.

When combined, the overall energy resolution worsened as the energy of the detected neutron increased and as the flight path decreased, ranging up to 52% at the highest energies. Figure 36 is an example of the fractional energy resolutions at one of the longest (10°) and shortest (135°) flight paths for the 400 AMeV iron projectiles incident on 20 g/cm^2 aluminum. It was noticeable that the energy resolution was worse for the scintillator at 135°, with absolute percentage differences in the uncertainties that were roughly 2 to 4% higher than those at 10° in the overlapping energy region. Similarly, the energy resolutions worsened with the increase in neutron energy, particularly above 40 MeV.

V.2.4 High-Energy Correction Factor

Large energy resolutions at high energies resulted in spectral shape ambiguity for some beam-target systems. To account for this issue, an additional correction factor was added to neutrons at or above the incident beam energy in MeV per nucleon (*b*). First, a Monte Carlo-based simulation was designed to track the neutrons produced in the upstream target as a function of neutron energy and depth in the target. PHITS version 2.76 was used with the physics settings described in Section IV.9.1. For each beam-target configuration, the upstream target was placed in an air-filled sphere and a cylindrical ion source (2.5 cm diameter) was placed 15 cm away from the center of the front surface. A geometric mesh with a cross sectional area (width by height) of 100 by 30 cm^2 was then established along the *z*-centerline of the target, stepping through the target depth in increments of 1 g/cm^2 aluminum (~0.37 cm). Next, the T-Product tally calculated the neutrons produced in the user-specified energy groups by all primary beam particles and secondary ions in each mesh region. Production mechanisms included nuclear reactions, decays, and fission [29]. Neutrons produced outside the target in air were not tracked. Neutrons produced per source particle for the five projectile beams incident upon 20, 40, and 60 g/cm^2 aluminum are presented in Figure 37 to Figure 41. The black vertical lines represent the target boundaries and the projectile beams were incident from the left side of the plots.

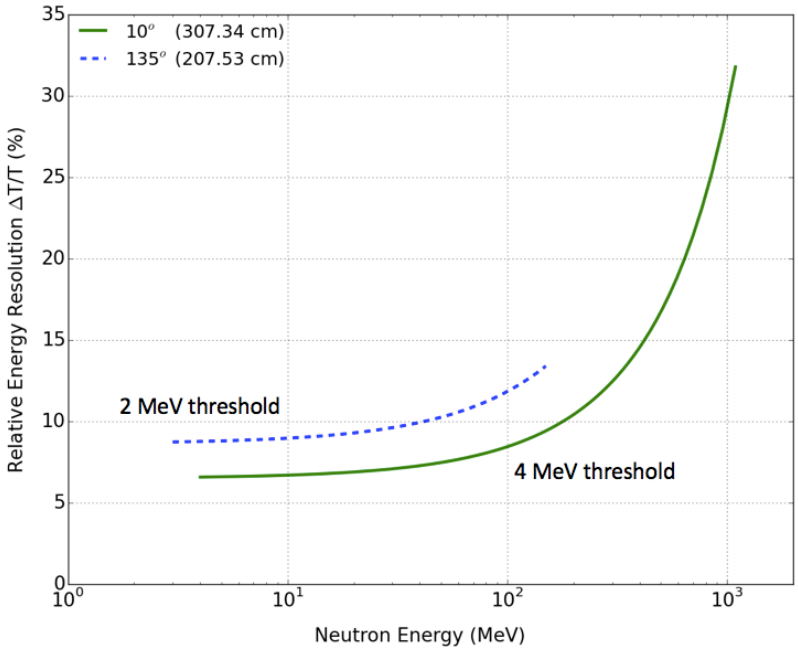


Figure 36. Fractional energy resolutions for 400 AMeV iron beam on 20 g/cm^2 aluminum at 10° and 135°. Listed flight paths are from upstream target center to scintillator active volume center.

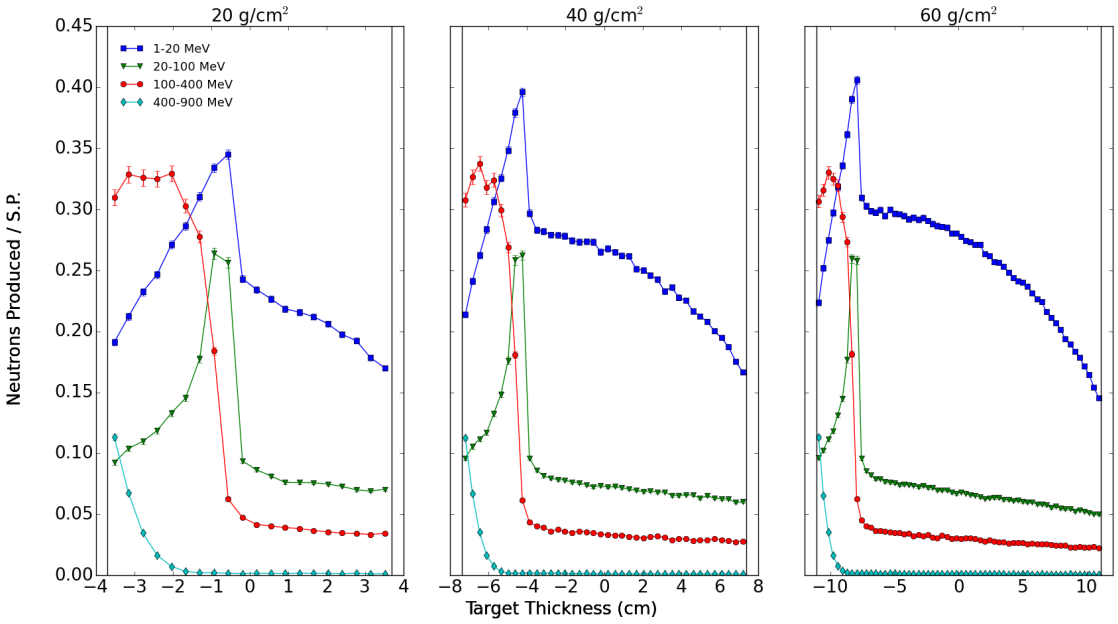


Figure 37. Neutrons produced in 20, 40, and 60 g/cm^2 aluminum with 400 AMeV iron projectiles.

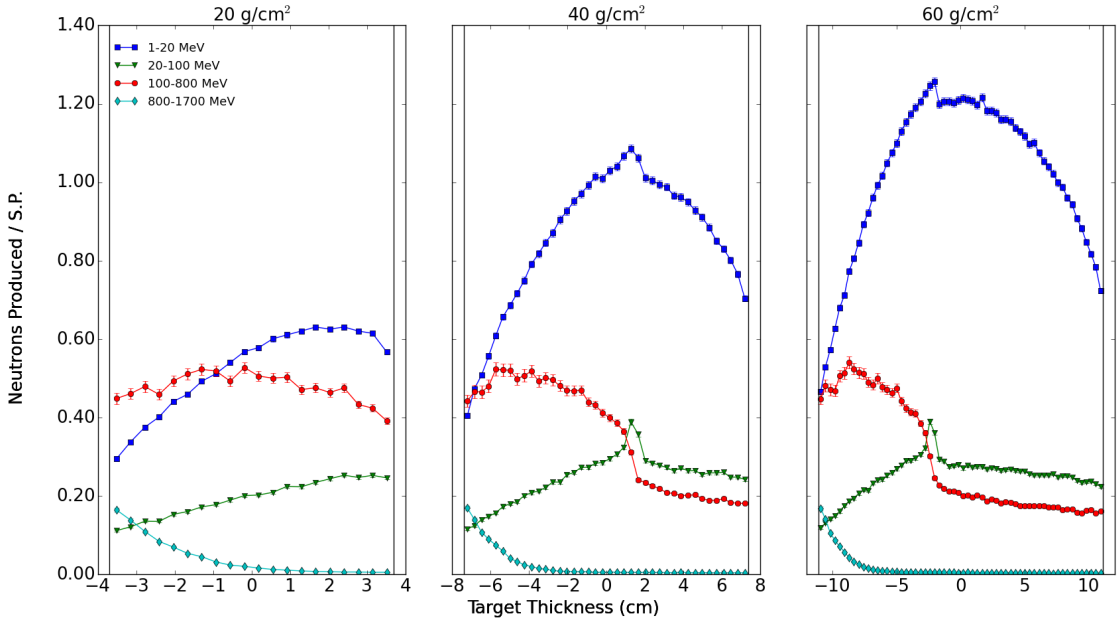


Figure 38. Neutrons produced in 20, 40, and 60 g/cm^2 aluminum with 800 AMeV iron projectiles.

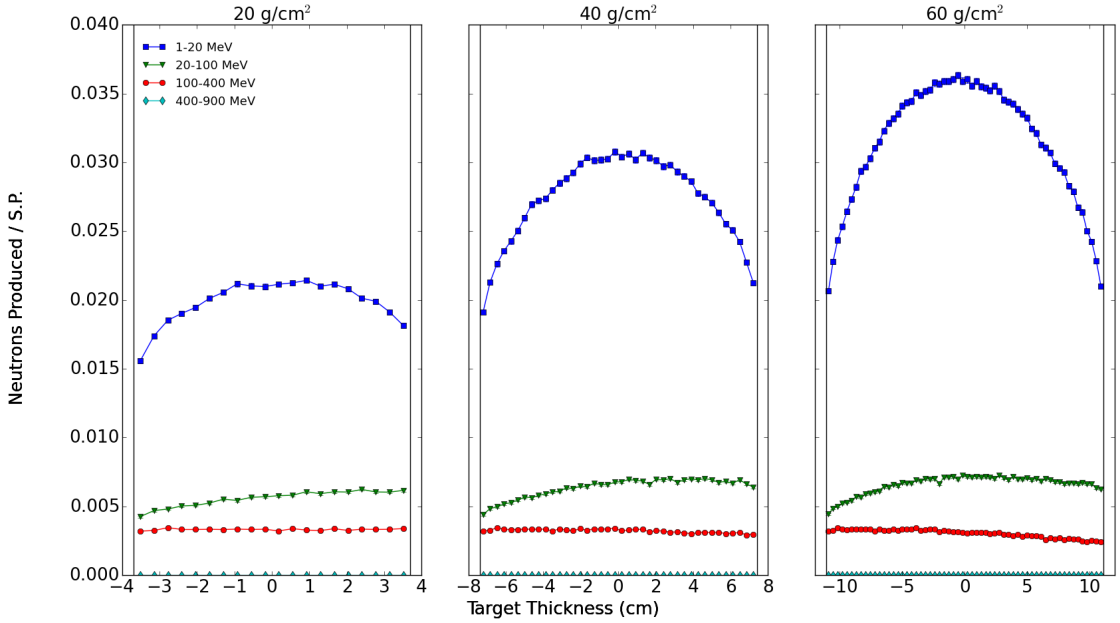


Figure 39. Neutrons produced in 20, 40, and 60 g/cm^2 aluminum with 400 MeV proton projectiles.

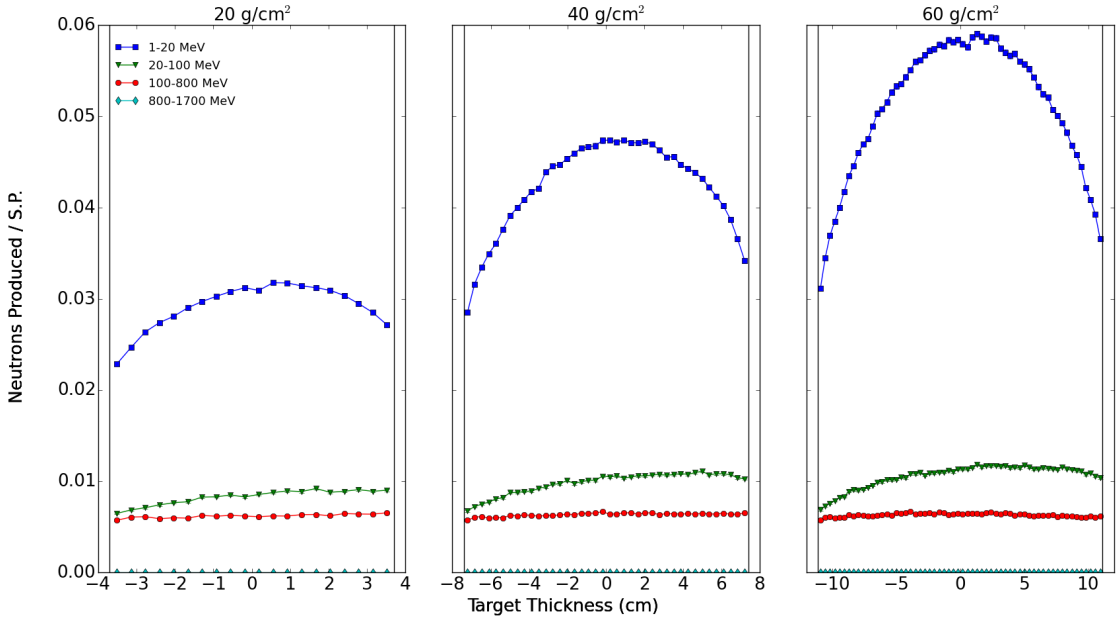


Figure 40. Neutrons produced in 20, 40, and 60 g/cm^2 aluminum with 800 MeV proton projectiles.

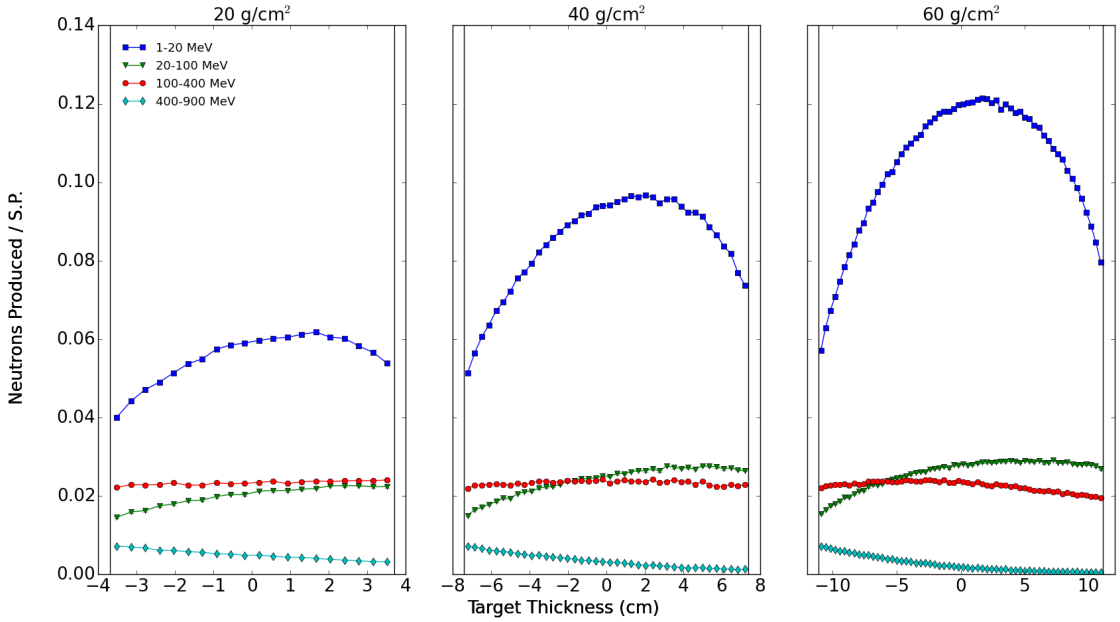


Figure 41. Neutrons produced in 20, 40, and 60 g/cm^2 aluminum with 400 AMeV helium projectiles.

The user-defined energy groups were based on the regions observed in the experimental energy spectra. Neutron groups included: 1 to 20 MeV, 20 to 100 MeV, 100 to *b* MeV, and *b* to (*2b+100*) MeV. The first two groups represented the lower energy region characterized by the exponential downward slope seen in the experimental energy spectra. The third group covered the observed plateau region to slightly past the incident beam energy, *b*, in MeV per nucleon, while the fourth group encompassed high-energy neutrons beyond *b*. Statistical uncertainties for the first three energy groups were less than 4% and less than 10% for the high-energy group.

Holding target thickness and beam species constant, increasing the beam energy resulted in increased neutron production in the upstream target, as expected. Likewise, increasing the mass of the incident projectile increased neutron production due to the larger number of interactions occurring between the beam and target. The simulation also demonstrated that the neutron yields between 1 and 20 MeV increased as target thickness increased, since low-energy neutrons were produced by target evaporation during fragmentation. An increase in target thickness resulted in more beam-target interactions and thus, more target evaporation neutrons. Contrastingly, the 20 to *b* MeV neutron yields remained roughly constant as target thickness increased. Neutron yields above *b* MeV for iron and helium projectiles approached zero as the target thickness increased due to the decrease in projectile beam energy as a function of target depth. Additionally, neutrons above *b* MeV were equal to zero for the proton projectiles on all target thicknesses because most high-energy neutrons at forward angles originated from projectile breakup. Since proton beams did not contain neutrons, high-energy neutrons were not produced.

The peak observed in the 1 to 100 MeV energy ranges for 400 AMeV iron on 20, 40, and 60 g/cm^2 aluminum was located at a target depth of 3.3 cm (8.9 g/cm^2), which matched the depth where the beam stopped in the upstream target. Similarly, this peak was located at a target depth of 9.3 cm (25.1 g/cm^2) for the 800 AMeV iron incident on 40 and 60 g/cm^2 aluminum, which also corresponded to the depth where the beam stopped. Increased neutron yields near the end of the iron projectile ranges may be attributed to the combination of an increase in the total reaction cross section and the stopping power at low projectile energies [99]. Neutron production beyond the stopping peaks was attributed to secondary particles interacting with the target. No peaks were

observed with the remaining beam-target systems because the projectiles all punched through the upstream targets.

While neutrons between 1 and *b* MeV were produced throughout the full width of the upstream target, the high-energy ($\geq b$) neutron yields for the iron- and helium-induced reactions dropped off as the depth in the target increased. This meant the original flight path assumption, which was measured from target center to liquid scintillator center (a_1), was inaccurate for high-energy neutrons (Figure 42). Likewise, the solid angle and flight path uncertainties, which included the distance from the downstream surface of the front target, were overestimated. Thus, a high-energy neutron correction factor was needed for neutrons detected with energy $\geq b$. By integrating the area under the high-energy production curves (Figure 37, Figure 38, and Figure 41) and calculating the target depth that encompassed 80% of the total neutron production, a revised target "width" (z) that was less than the true target width ($2w$) was determined. The revised flight path (a_2) was then extended to the midpoint of z, lengthening the original flight path from a_1 to $\sqrt{c_2^2 + b^2}$. Flight path and target width adjustments for each iron- and helium- configuration are shown in Table 16 (Appendix I). As expected, the revised target width z was less than the true target width $2w$ for the Z>1 projectiles on all aluminum target thicknesses. For the 400 AMeV iron, 800 AMeV iron, and 400 AMeV helium projectiles, the revised target widths were an average of 18%, 31%, and 61% of the true target widths, respectively.

After the energy spectrum for the selected iron- or helium-target system was created, neutrons with a bin midpoint $\geq b$ were removed. Neutron energies for these bins were then recalculated using the revised flight paths (Table 16) and appended to the original spectrum. By lengthening the flight paths but keeping the neutron TOF constant, the bin energies were adjusted upwards between 0.9 and 24.8 MeV. Additionally, the corresponding solid angle and flight path uncertainties were recalculated by considering the revised "downstream" surface (z) of the front target instead of the true physical downstream surface ($2w$). This change reduced the solid angle and flight path uncertainties by decreasing the differences between their minimum and maximum values. The absolute difference in the fractional solid angle uncertainties for the high-energy corrected neutron yields decreased up to 5.7% between 10° and 80°. This meant at high energies, the corrected

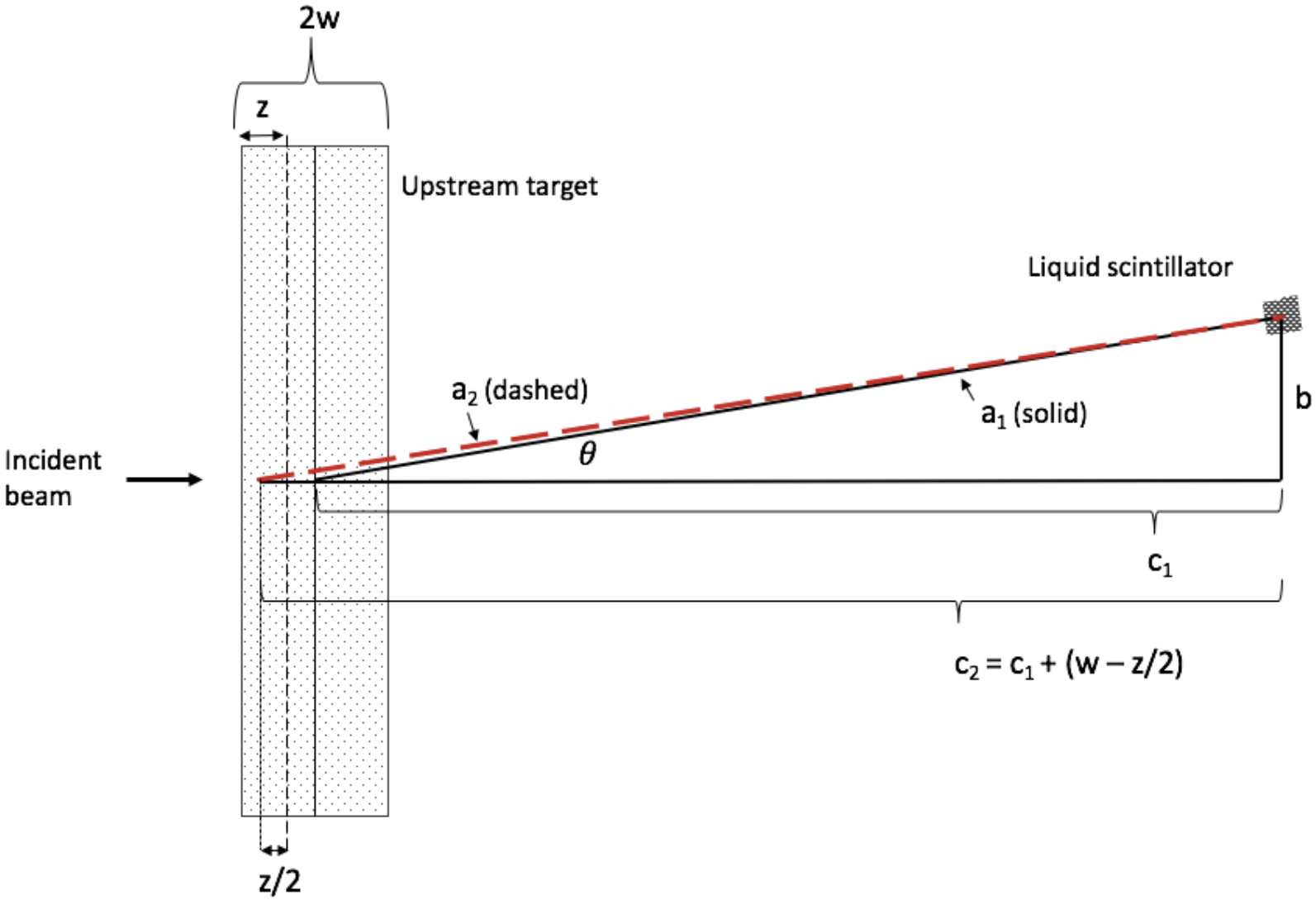


Figure 42. Flight path adjustment for high-energy neutrons schematic.

fractional solid angle uncertainties ranged from 4.4 to 7.6%, versus 5.4 to 11.3% if left uncorrected (Table 12). With the correction to the flight path uncertainties, the overall fractional energy resolutions now ranged between 5.5 and 35.6%, an absolute percentage decrease in up to 16.3%. The largest uncertainty reductions occurred for the iron and helium projectiles incident upon the 60 g/cm^2 target since the thickest target had the largest flight path extremes. In general, one or two energy bins were replaced in 70% of the iron and helium datasets measured between 10° and 80°. No corrections were applied at 135° since all detected neutrons were significantly below *b*.

V.3 Experimental and Simulated Double Differential Thick-Target Neutron Yields

V.3.1 Experimental DDTT Yield Spectra

The DDTT neutron yields for all projectile-target systems measured in March 2016 are displayed in Figure 47 through Figure 66 in Appendices II and III. Statistical uncertainties in the yields and the uncertainties in the energy for the bin midpoint are included. To display the results for a given projectile-target system at six angles on the same figure, yields at each angle were multiplied by successive powers of 100, starting with the results for the 80° liquid scintillator. This allowed for the visual separation of yields at low energies. Additionally, each figure contains PHITS or MCNP simulation results. These results are represented by either a dashed or solid line, specified later. Statistical uncertainties for the simulations and systematic uncertainties for the experimental results are not included in the plots, but were previously discussed in Sections V.2.1 and V.2.2, respectively.

With the Z>1 projectile beams (400 and 800 AMeV iron, 400 AMeV helium), a broad, fairly flat peak was observed at 10°, roughly between 50 and 80% of the incident beam energy in AMeV. As previously mentioned, a broad peak was formed, instead of a sharp peak like in cross section measurements, due to the range of projectile energies and projectile-target interaction mechanisms in the thick targets [22]. Most of the neutrons within and above the broad peak originated from projectile nuclei fragmentation or the knock-out process [21]. As the upstream target thickness increased from 20 to 60 g/cm^2, the broad peak slightly flattened out, most likely due to the energy loss of high-energy projectiles as they traversed the additional aluminum material. Past the peak,

neutrons with rapidly decreasing yields were observed with energies up to approximately twice the incident beam energy. For the 800 AMeV iron projectiles, fewer high-energy neutrons were counted due to the poor energy resolution at forward angles. DDTT yields below the broad energy peak were characterized by an exponential decrease.

For the Z=1 projectiles (400 and 800 MeV protons), a sharp drop-off near the incident beam energy instead of a broad peak was observed at 10° because of fewer available projectile-target interaction mechanisms. It was expected that few neutrons with energies above the incident beam energy would be detected due to the absence of neutrons in the proton beams, and thus, lack of neutrons originating from projectile breakup. However, neutrons with up to 1.6 times the incident beam energy were observed at multiple angles for the 400 MeV proton beam. An appreciable number of neutrons created with the 800 MeV proton beam were not detected over 800 MeV. Despite these differences, all proton projectile systems featured an energy shoulder near the incident beam energy in the 10° liquid scintillator.

At intermediate neutron energies and as the angles increased between 30° and 80°, the broad peak featured at 10° became less and less prominent, forming a shoulder, and the experimental yields began to decrease more rapidly as the neutron energy increased. Neutrons detected at these angles mostly originated from the overlap region formed during a projectile-target interaction [12], [20]. At all angles, detected neutrons with energies <20 MeV originated from breakup of the target nuclei [21]. The emission of low-energy neutrons appeared isotropic because the target pre-fragment was moving slowly in the laboratory frame [12]. This resulted in the overlap of low-energy neutron yields at all angles. The neutron yields at 135° were dominated by this process.

A portion of the experimental data had large statistical uncertainties or negative data points for neutrons below approximately 120 MeV. While this was also seen at wider angles, large uncertainties or negative data points were mostly observed in the liquid scintillator at 10° due to its proximity to the downstream target and beam dump, especially with projectiles that punched through the upstream target and interacted in the downstream target (Table 5). It was determined that the background neutron yields below 120 MeV were on the same order as or slightly higher than the neutron yields that originated from the upstream target.

Because this experiment was not conducted in a vacuum, it is possible that the measured yields included neutrons that were produced in the upstream target and in the air column along the beamline. These neutrons, which were produced by primary beam interactions in air or were ablating off the forward-moving projectile fragments, may not have been fully blocked by the shadow bar system and would be partially included in the background measurements. This would increase the final statistical uncertainties according to equation 10. Additionally, it is possible that neutrons were created by an interaction between a projectile fragment and the shadow bar, entering the liquid scintillators as background. This would increase the background measurements relative to the runs without the shadow bars, artificially suppressing the true DDTT yields. If the production of extra background neutrons during a shadow bar run surpassed the number of neutrons created during an un-shadowed run, the resulting DDTT yields may have negative values after background subtraction and consequently be thrown out of the analysis. Furthermore, a high-energy neutron may have entered the liquid scintillator and imparted enough energy such that a recoil proton escaped the scintillator and struck the veto detector. This would tag the high-energy neutron signal as a charged particle event, which would eliminate it from either the total or the background counts, depending upon the run. This process was unlikely due to the low number of charged particle events seen in the front veto detector during a shadow bar run.

Despite these possibilities, large statistical uncertainties at low energies were mostly caused by the simple lack of neutron counts. At forward angles, comparable levels of total and background neutron measurements resulted in large statistical uncertainties after background subtraction. At wider angles, low neutron counts below 120 MeV were most likely attributed to increased attenuation through the large amount of target material the neutrons had to traverse, when compared with measurements at forward angles. For the March 2016 calculations, a pulse height stitching technique was successfully utilized to reduce these large statistical uncertainties below 120 MeV. In the subsequent November 2016 run, fractional statistical uncertainties were decreased by lengthening the beam spill to approximately 3 to 4 s, which increased the number of projectile-target interactions and subsequent secondary neutrons per spill.

In addition to rebinning the data, a pulse height stitching technique was utilized for specific beam-target systems to reduce statistical uncertainties. For a given system, the background-subtracted

neutron data were read out of ROOT with a series of increasing pulse height gates (Section IV.3.6). As the pulse height increased, the signal-to-noise ratio was improved for some data points by eliminating low pulse height neutron events, reducing the background neutron contributions. This decrease in the neutron background resulted in increased DDTT yields, smaller statistical uncertainties, and the "reappearance" of neutron yields that were previously negative due to background subtraction.

For each pulse height gate dataset, new energy-dependent neutron detection efficiencies were calculated with SCINFUL-QMD, and the resulting yields were normalized, corrected, and rebinned as previously discussed. Multiple DDTT yield datasets could then be stitched together to replace specific data points with large statistical uncertainties. An example of this procedure is shown in Figure 43 for a system at 30º. The original spectrum taken with the minimum, 4 MeV pulse height gate is shown in black. After exploring the DDTT yields taken with different pulse height gates, the 4 MeV pulse height data at neutron energies of 10.8 and 16.7 MeV were replaced with data taken with a 7 MeV pulse height gate. For the 10.8 MeV data point, the absolute difference in the statistical uncertainty decreased by 7% and the DDTT yield increased by approximately 1.3 times. A slight improvement was seen with the 16.7 MeV data point. The absolute difference in the statistical uncertainty decreased by 0.3%, while the DDTT yield increased by less than a factor of 1.01. Overall, this method could be used to sample different energy regions of neutron spectra, resulting in final spectra with lower statistical uncertainties.

Experimental and simulated DDTT neutron yields for all beam-target systems at six liquid scintillator locations will be discussed in the next section. Recall that two geometry configurations were used in PHITS (room geometry and ring geometry) to explore differences in the yield contributions from neutrons produced by room scatter and the downstream target. Additionally, neutron yields were calculated in MCNP using the room geometry. During the execution of these simulations, a separate particle tracking technique was also run to determine the directionality of individual neutron events in the MCNP simulations. This particle tracking information was then used to exclude neutrons not produced in the upstream target. The angular yield distributions for each system will also be discussed in Section V.3.3.

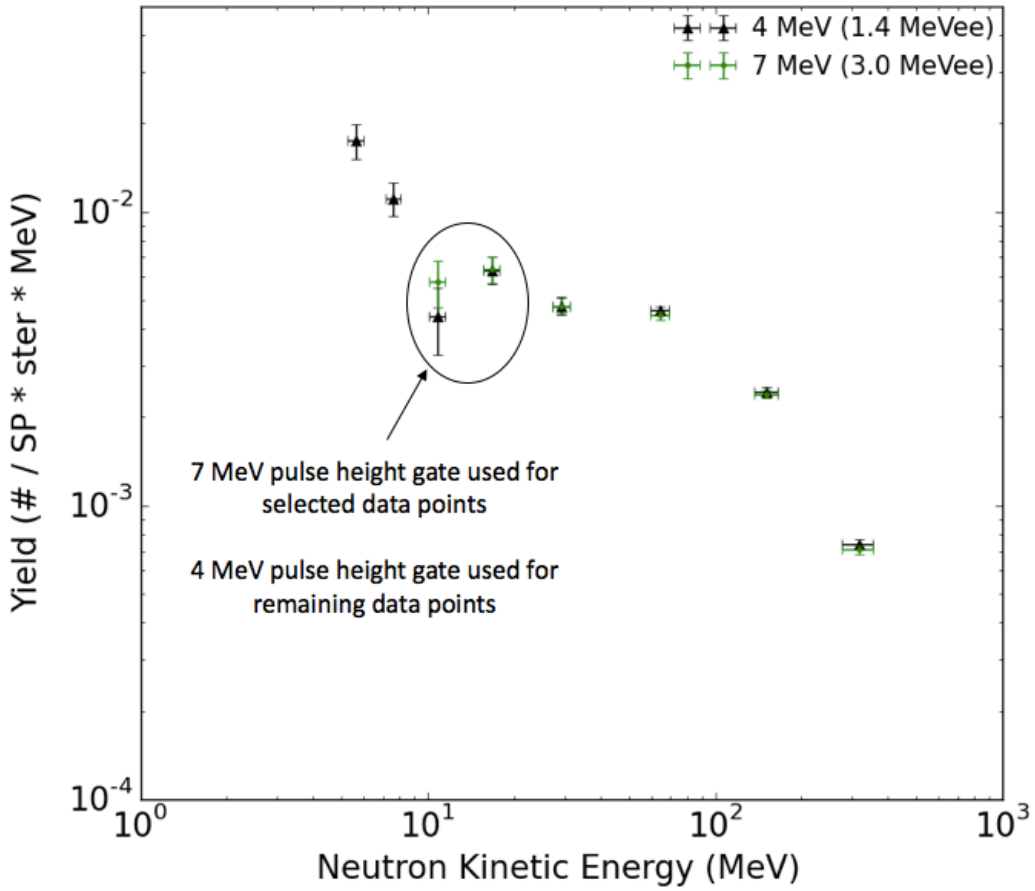


Figure 43. Pulse height stitching at 30º for 400 AMeV iron projectiles incident on 20 g/cm^2 aluminum.

V.3.2 Comparison with PHITS and MCNP Simulations

In general, the largest differences seen between the four sets of MCNP and PHITS simulations and the experimental DDTT neutron yields occurred below the broad peak (forward angles) or shoulder (wider angles) at all angles. For clarity, the differences between the MCNP and PHITS simulations calculated with the room geometry in this energy region will first be discussed, followed by a discussion on the differences between the simulations that modeled the room geometries and those that excluded room-scattered neutrons. The differences between the background-corrected MCNP and PHITS simulations will then be compared to the experimental yields at all energies.

Figure 47 through Figure 51 in Appendix II compares experimental DDTT neutron yields to those calculated with the room geometry in MCNP (dashed line) and PHITS (solid line). Both sets of simulations included neutrons that originated from the upstream target in addition to low-energy, room-scattered neutrons. Overall, the MCNP and PHITS geometry yields differed the greatest at low and intermediate energies below the broad peak or shoulder, particularly at 10º. Here, the MCNP-calculated yields were larger than the PHITS yields below the start of the peak by up to a factor of 6. The same behavior was seen to a lesser extent below the shoulder as the angle increased to 30º, and disappeared at larger angles. As the angle of detection increased between 30º and 135º, the MCNP and PHITS simulations approached each other for most systems, with the best fit between the transport codes demonstrated at the shoulder energies at wider angles. Differences between the two transport models also appeared to decrease as the aluminum target thickness increased from 20 to 60 g/cm^2. Both sets of simulations systematically overestimated the experimental yields at low to intermediate energies, with the exception of the 400 MeV proton systems discussed later.

Since most room-scattered neutrons were measured at low to intermediate energies, a closer fit to the experimental data in this energy region was expected with the PHITS ring geometry and the directionally-corrected MCNP simulations. As seen in Figure 57 through Figure 66 in Appendix III, the PHITS and MCNP simulations that modeled the realistic room geometries were higher than their background-corrected counterparts below the peak or shoulder, as expected. The largest differences between the PHITS ring and room geometries were noted below 10 MeV for all beam-target systems, with the room geometry yields surpassing the ring yields by up to a factor of 7.5 at

the lowest energies. Similarly, the MCNP room geometry simulations surpassed the directionally-corrected MCNP simulations up to an approximate factor of 30 at the lowest recorded experimental neutron energies, with smaller differences seen as the neutron energy and angle increased. At the beginning of the peak or shoulder energy, both sets of MCNP and PHITS geometry simulations merged with their corrected counterparts. An exception to this observation involved the simulations at 80° for all projectile beams incident on the 40 and 60 g/cm^2 aluminum targets. Here, the PHITS ring yields were up to approximately 1.6 to 1.9 times higher than the room yields between ~5 MeV and the peak or shoulder energy for all projectiles. As a result, the PHITS room geometry simulations more closely modeled the experimental data at 80° in this energy region.

Figure 52 through Figure 56 in Appendix II compares experimental DDTT neutron yields to those calculated using the MCNP room geometry with the neutron directionality correction (dashed line) and the PHITS ring geometry (solid line). Overall, the ring-calculated PHITS yields were larger than the directionally-corrected MCNP yields below the peak or shoulder energies at all angles. At 10º, this difference extended through the peak, with the two sets of simulations merging at high energies. Larger differences between the two sets of 80º simulations were observed at intermediate energies, most likely due to PHITS' overestimation of neutron contributions from the thickest section of the upstream target. Differences between the simulated and experimental results varied based on the neutron energy and angle of detection, and tended to decrease as the target thickness increased from 20 to 60 g/cm^2.

For the Z>1 projectile systems, the PHITS ring simulations generally overestimated the experimental DDTT yields at low and intermediate energies between 10º and 45º, while the directionally-corrected MCNP simulations tended to underestimate the experimental yields in this region. Because the corrected MCNP simulations excluded all neutrons that did not originate from the upstream target, this underestimation might indicate that the experimental DDTT yields also contained neutrons that were ablating off the forward-focused projectile fragments in the air column. As the angle increased to 60º and 80º, the experimental yields were fairly well-modeled by MCNP below the shoulder, indicating that air column-produced neutrons were not measured at wide angles. This trend was not observed for the 800 AMeV iron systems at 60º, where both sets of simulations overestimated the low energy yields. At 135º, the experimental yields were fairly

well-modeled by both PHITS and MCNP for the 800 AMeV iron projectile systems, with underestimations at most energies prominent for the remaining Z>1 systems.

At the beginning of the 10º broad peak for the Z>1 projectile beams, both simulations continued to overestimate the contributions from projectile break-up or the knock-out process. Here, the MCNP models gave a flatter peak profile that more closely resembled the experimental neutron yields, differing in height up to approximate factors of 1.2 to 2.2. For the 800 AMeV iron and 400 AMeV helium projectile systems, the location of the experimentally measured broad peak lined up fairly well with the MCNP calculations. However, MCNP predicted a peak that was shifted approximately 50 to 100 MeV higher than the experimental peak for the 400 AMeV iron system, which underestimated the DDTT yields at the beginning of the broad peak.

For the 800 MeV proton systems, the experimental yields at 10º and 135º were fairly well-modeled by both sets of simulations at all energies, excluding the forward-angle peak. Between 30º and 80º, the directionally-corrected MCNP results were a better fit to the results below the shoulder, with overestimations demonstrated by the PHITS ring simulations. For both Z=1 projectile beams at 10º, the simulations predicted a sharp drop in the DDTT neutron yields followed by a narrow, pronounced peak near 80 to 95% of the incident beam energy. This sharp peak then broadened and flattened out as the target thickness increased, especially for the lower energy 400 MeV proton projectile beam systems. Instead, the experimental yields demonstrated a more flat, gradual drop-off in this energy region, falling more sharply past the peak location. Unlike the Z>1 calculations, PHITS predicted lower peak heights than MCNP, though they were still larger than the experimental yields up to an approximate factor of 3. Yields beyond the peak energies were under-predicted by both MCNP and PHITS for most Z>1 and Z=1 systems, especially at wider angles.

Finally, experimental yields for the 400 MeV proton systems were systematically higher than the PHITS and MCNP yields between 10º and 80º at most energies, with smaller differences noted between the experimental yields and the PHITS ring simulations as the angle increased. In general, the measured yields were more variable than expected, especially at forward angles. The 400 MeV proton systems had lower projectile-target interactions in comparison to the remaining beam-target systems, resulting in lower secondary neutrons and high statistical uncertainties. It is also possible

that the beam currents used during the experiment were too high, due to the diffuse nature of the charge deposited by the 400 MeV proton projectiles. If this was the case, then the high beam current during the experimental runs lead to improper source particle normalization. With a high current, multiple beam particles may have entered the start scintillator simultaneously but were only counted as a single event by the scalers. This would affect the background subtraction and normalization, potentially leading to higher-than-expected DDTT neutron yields. However, the large differences noted between the experimental and simulated results may also point to issues with the intranuclear cascade models used by MCNP and PHITS, particularly for nucleon-nucleon interactions. Because of the large differences seen between the simulated and experimental yields, the large statistical uncertainties, and the beam current issues noted during the measurements, the author recommends re-measuring the 400 MeV proton systems in the November 2017 experiment. This will either verify or replace the 400 MeV proton system measurements from March 2016.

Due to the nature of thick-target measurements, it is often difficult to determine the root cause of inconsistencies that exist between simulations and experimental measurements. An incident projectile has a high probability of multiple interactions in a thick target, which may produce neutrons and other charged particles over a wide range of energies and masses [22]. After their production by incident or secondary projectiles, the energies and yields of secondary neutrons may be further modified by transport through the thick target [32]. Thus, the accuracy of the PHITS and MCNP simulations are dependent upon both the accuracy of the neutron production models and the neutron transport calculations. There is some research to suggest that attenuation of neutrons through thick targets is fairly accurately modeled by PHITS, indicating that differences between the simulations and experimental measurements may be dominated by the neutron production cross sections [47]. While neutron transport is sure to have some effect on the accuracy of the simulations, the secondary particle production cross sections utilized in the various intranuclear cascade models is a known source of inconsistencies between experimental measurements and Monte Carlo simulations. Further studies are needed to determine whether inconsistencies were dominated by production models or neutron transport, and to what degree. Additionally, an analysis should be performed to determine which production cross sections have the largest effect on the simulated results, with the ultimate goal to measure said cross sections.

Overall, the PHITS ring simulations and the directionally-corrected MCNP simulations differed the most from the experimental DDTT neutron yields below the peak or shoulder, which may be the result of inaccuracies in the neutron production cross sections utilized in the cascade models. These differences were more apparent at forward angles, and neutron contributions from projectile breakup or knockout reactions were overestimated by both transport codes at the 10° broad peak. At the shoulder energies between 30° and 80°, both simulations tended to merge together which lead to fairly accurate predictions with either transport code. As the energy increased, all simulations tended to underestimate neutron yields at (60°) and above (all angles) the shoulder energy. Neutron yields from target breakup at 135° were fairly well modeled by both simulations with the 800 AMeV projectile systems, underestimating yields with the 400 AMeV systems. Finally, the simulated and experimental yields tended to differ the most with the 20 g/cm^2 aluminum target systems when compared to thicker targets. PHITS and MCNP would greatly benefit from improvements in the physics models at low and intermediate energies, in addition to better peak-prediction capabilities at 10°. Additionally, both transport codes would benefit from improvements in the target breakup models that dominate the 135° spectra.

V.3.3 Angular Distribution of DDTT Neutron Yields

Finally, the DDTT neutron yields at each angle were integrated above a threshold energy to study the angular distribution in the yields (*# neutrons / S. P. / Ω*). Due to the difference in threshold energies between the forward- (4 MeV at[2] 10º, 30º, and 45º) and wide-angle (2 MeV at[3] 60º, 80º, and 135º) scintillators, as well as the elimination of some low-energy counts with pulse height stitching, each system was integrated above the greatest common minimum energy bin for all projectile beam systems. All beam-target systems were integrated above 7.6 MeV, which allowed for a comparison between the overlapping energy regions. The neutron angular yield distributions for the iron (Figure 44), proton (Figure 45), and helium (Figure 46) systems are shown below.

[2] 1.4 MeVee
[3] 0.51 MeVee

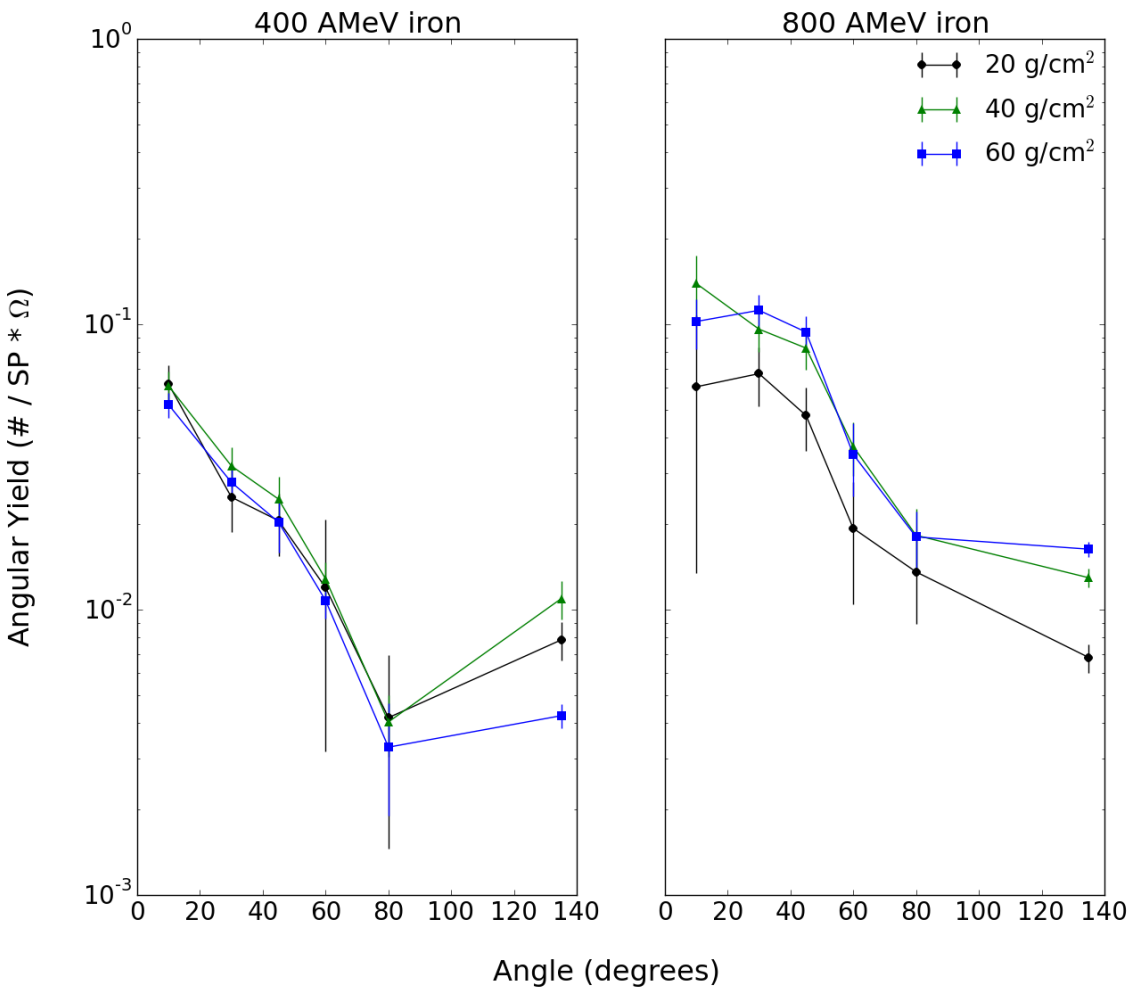


Figure 44. Angular yield spectra for the 400 and 800 AMeV iron systems.

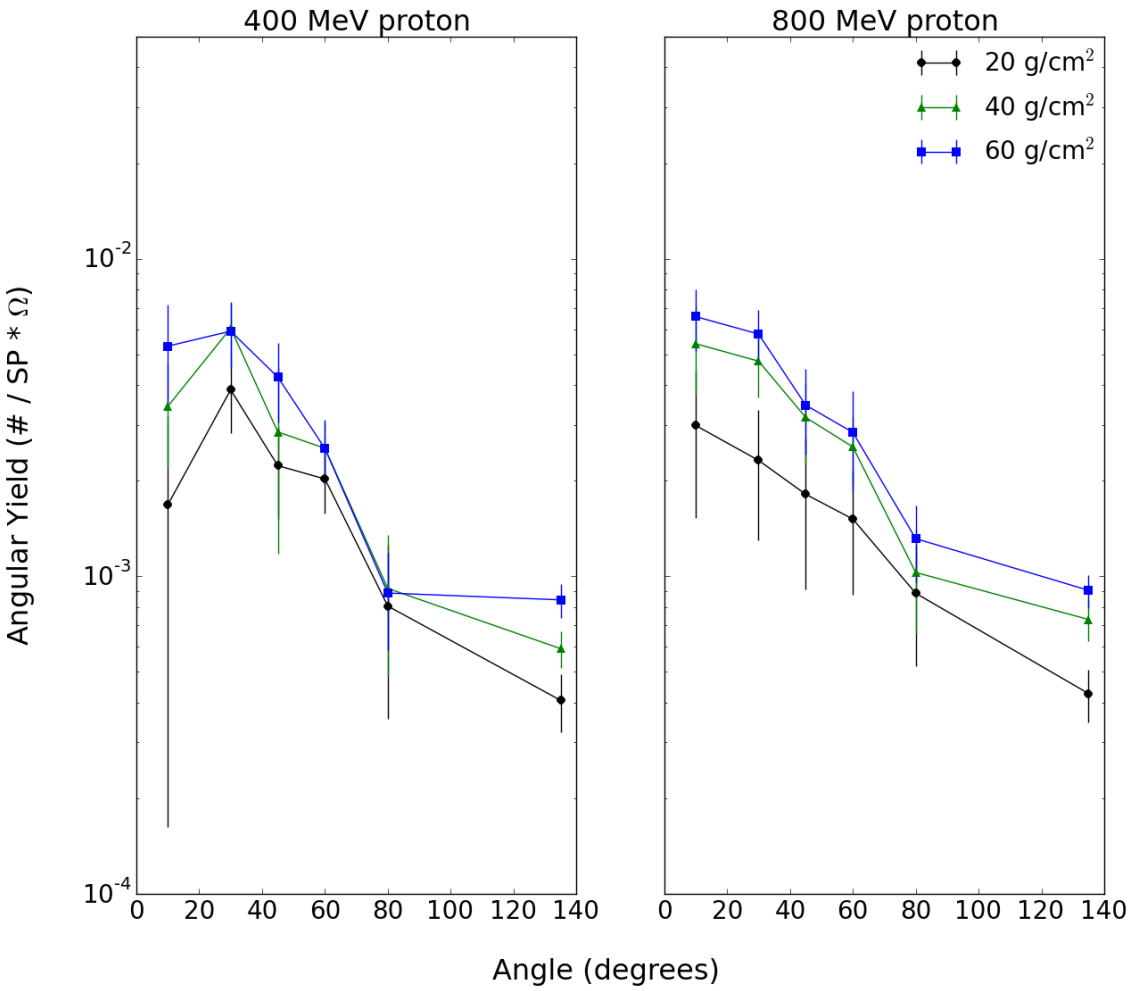


Figure 45. Angular yield spectra for the 400 and 800 MeV proton systems.

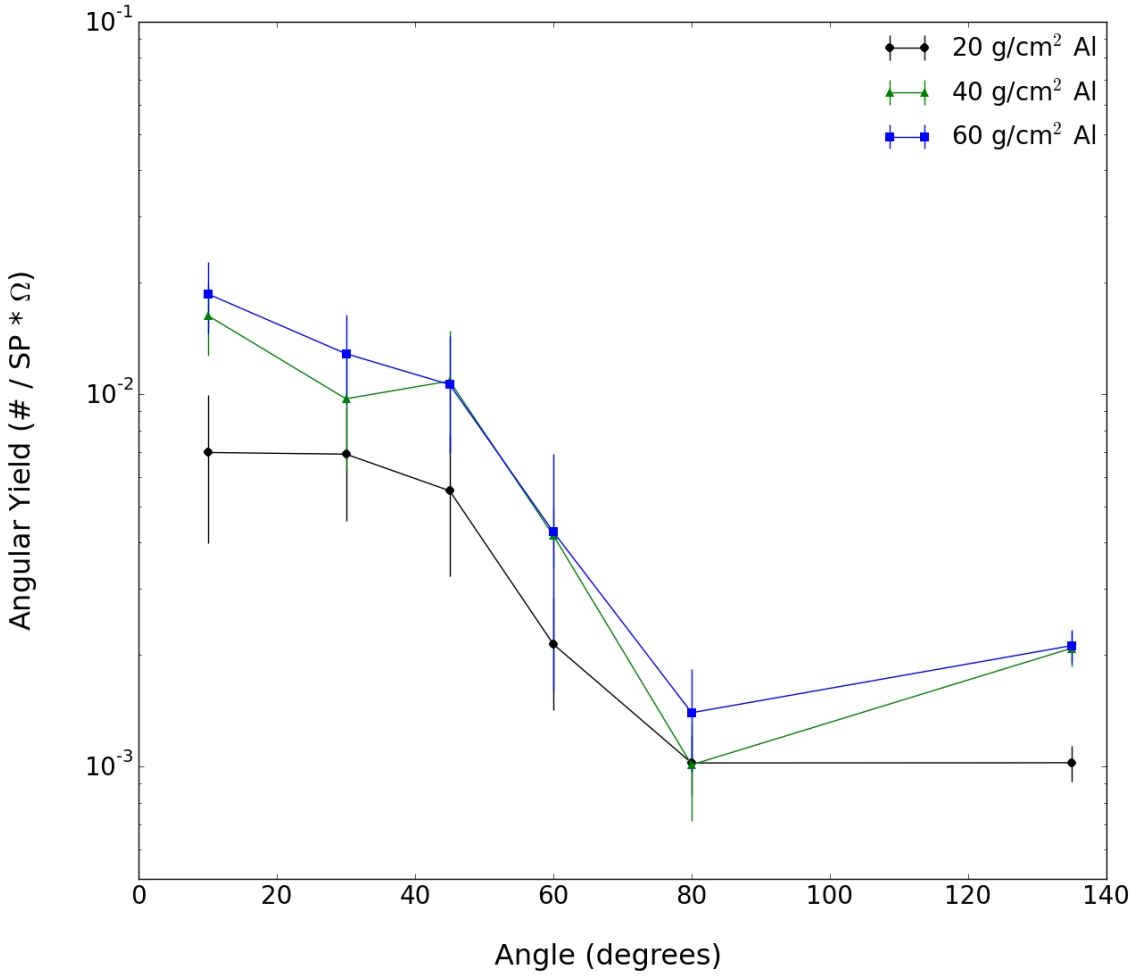


Figure 46. Angular yield spectra for the 400 AMeV helium systems.

Experimental angular distributions at most angles increased as the projectile mass or projectile energy increased for the Z>1 systems. An increase in projectile mass or energy resulted in an increased number of interactions, resulting in increased secondary neutrons. However, a similar angular distribution was observed for both the 400 and 800 MeV proton systems, which could have been the result of the improper normalization of the 400 MeV proton yields, or because the neutron production cross sections are fairly flat for incident protons with energies between 400 and 800 MeV [100]. If proper normalization occurred, then more similar yields might be expected between these two proton systems than what was seen with heavier projectile beams.

Additionally, most of the yields decreased as the detection angle increased from 10º to 135º. This drop was attributed to the lack of high-energy, forward focused neutrons seen at wider angles. Exceptions included the yields at 10º for 800 AMeV iron and 400 MeV proton systems. For the 800 AMeV iron system, lower yields at 10º could also be attributed to a lack of high-energy neutrons due to resolution issues. An uptick in neutron yields was observed at 135º for the majority of the 400 AMeV iron and helium systems, while other systems saw approximately equal yields at 80º and 135º, especially for the 60 g/cm^2 target systems. This increase may be attributed to the low neutron background seen at 135º in conjunction with the shorter amount of upstream target material that was traversed by neutrons that were detected at 135º versus at 80º. If a neutron was created at the center of the upstream target, it would have to traverse 21 (20 g/cm^2 target) to 51 cm (60 g/cm^2 target) of aluminum before detection at 80°, compared to approximately 2.5 to 7.6 cm of aluminum before detection at 135°.

Angular yields as a function of target thickness generally depended upon whether or not the projectile beam was fully stopped in all thicknesses of the upstream aluminum target (Table 5). For example, the 400 AMeV iron projectile beam fully stopped in the first 8.9 g/cm^2 of all upstream targets. After the beam stopped, neutrons were produced by secondary ion interactions in the target material. While there was some overlap in the yields at wider angles between 45º and 80º, the 40 g/cm^2 system had the highest yields at most angles and the 60 g/cm^2 system had the lowest yields at most angles. This indicated that the additional material in the 60 g/cm^2 aluminum target may have attenuated or stopped the neutrons produced by secondary ion interactions. However, this effect was not seen for the 800 AMeV iron projectile beam that stopped in the 40 and 60 g/cm^2

aluminum targets. These systems more closely resembled the projectile beams that were not fully stopped in the upstream targets.

The remaining projectile beam systems all punched through the upstream target. As a result, the addition of more target material increased the number of neutrons seen at all angles. Angular yields with the 60 g/cm^2 aluminum target systems were highest, followed by the 40 g/cm^2 target systems and the 20 g/cm^2 target systems. Some overlap between the 40 and 60 g/cm^2 aluminum target systems was noted between 45º and 80º, indicating that the neutrons emitted from the overlap region were most likely stopped in the larger target thicknesses seen at wide angles. Additionally, larger increases in the angular yields were seen between the 20 and 40 g/cm^2 systems when compared to the 40 and 60 g/cm^2. This could indicate that the addition of aluminum material in a thick target beyond a certain point only increased neutron yields slightly due to the increased attenuation.

VI. CONCLUSIONS AND FUTURE WORK

This dissertation includes a series of secondary neutron measurements taken in March 2016 at Brookhaven National Laboratory's NASA Space Radiation Laboratory. Double differential thick target (DDTT) neutron yields were calculated at 10º, 30º, 45º, 60º, 80º, and 135º off beam axis for 400 and 800 AMeV iron, 400 and 800 MeV proton, and 400 AMeV helium projectile beams incident upon upstream aluminum targets with areal thicknesses of 20, 40, and 60 g/cm^2. Additionally, a second, 60 g/cm^2 thick aluminum target was placed downstream in the experiment room to study backscattered neutrons, which was not included in this work.

In general, the experimental DDTT neutron yields from the upstream target demonstrated expected trends, though large statistical uncertainties were observed at energies below 120 MeV. These issues were more prominent for the projectile beam systems that punched through the thinnest, 20 g/cm^2 upstream aluminum target. The use of a pulse height stitching technique decreased the statistical uncertainties and improved the measurement results in this energy region by reducing low pulse height, background neutron events. Comparisons with PHITS and MCNP Monte Carlo radiation transport codes revealed significant inconsistences between the experimental and simulated DDTT neutron yields at low to intermediate energies, especially at forward angles. Both codes overestimated the peak yields at 10º, but modeled the experimental yields fairly well through the shoulder energy between 30º and 80º. At the back angle of 135º, both sets of simulations underestimated neutron contributions from target breakup for the 400 AMeV projectile beam systems. Overall, both transport codes would benefit from improvements in their neutron production models, particularly below the peak or shoulder energies at all angles.

Future work includes comparing experimental DDTT neutron yields to other Monte Carlo transport model calculations, like FLUKA or GEANT, for benchmarking purposes. Additionally, further studies should be performed to determine the influence of inaccuracies in neutron transport versus neutron production in the MCNP and PHITS physics models. Other useful analyses include identifying and measuring neutron production cross sections that have the largest effect on the differences between the simulated and experimental yields. On the experimental side, re-running

the 400 MeV proton systems in November 2017 is recommended based on the large differences seen between the simulated and experimental yields, the large statistical uncertainties, and the noted beam current issues. This improvement will allow for a more accurate comparison between the benchmarking proton datasets and the Monte Carlo results. Further steps such as increasing the beam spill length and correcting the trigger system were already implemented for the November 2016 experiment, and initial results demonstrated improvements in the measured DDTT yields and statistical uncertainties due to the increased number of neutron counts.

Overall, the double differential thick-target neutron yield measurements presented in this dissertation serve as an important benchmarking dataset for comparison to a variety of radiation transport codes. NASA Langley Research Center is working to incorporate these measurements into a rigorous uncertainty quantification procedure, which will ultimately help improve radiation transport calculations and optimize future shielding designs for long-term missions to Mars.

REFERENCES

[1] L. W. Townsend, W. C. deWet, J. A. Porter, K. R. Burton, and W. J. Smith, "Estimates of Maximum Solar Particle Event Proton Fluences That Do Not Exceed Permissible Radiation Exposure Limits," presented at the 45th International Conference on Environmental Systems, Bellevue, Washington, 2015.
[2] N. McGirl, A. J. Pawel, D. Schappel, J. Shamblin, T. Younkin, and L. Townsend, "Crew Radiation Exposure Estimates from GCR and SPE Environments During a Hypothetical Mars Mission," presented at the 46th International Conference on Environmental Systems, Vienna, Austria, 2016.
[3] M. Durante and F. A. Cucinotta, "Physical basis of radiation protection in space travel," *Rev. Mod. Phys.*, vol. 83, no. 4, pp. 1245–1281, Nov. 2011.
[4] J. W. Norbury *et al.*, "Nuclear data for space radiation," *Radiat. Meas.*, vol. 47, no. 5, pp. 315–363, May 2012.
[5] "Guidance on Radiation Received in Space Activities," National Council on Radiation Protection and Measurements, NCRP Report No. 98, 1989.
[6] J. P. Wefel, "Instrumentation for Radiation Measurement in Space," in *Proc. of the Workshop on the Radiation Environment of the Satellite Power System (SPS)*, Springfield, VA, pp. 117–183. U.S. DOE Report CONF-7809164, 1978.
[7] M. M. Shapiro, Ed., *Composition and Origin of Cosmic Rays*, vol. 107. Springer Netherlands, 1983.
[8] P. Meyer, R. Ramaty, and W. R. Webber, "Cosmic rays—astronomy with energetic particles," *Phys. Today*, vol. 27, pp. 23–30, 32, Oct. 1974.
[9] J. A. Simpson, "Elemental and Isotopic Composition of the Galactic Cosmic Rays," *Annu. Rev. Nucl. Part. Sci.*, vol. 33, no. 1, pp. 323–382, 1983.
[10] J. E. Turner, *Atoms, Radiation, and Radiation Protection*, 3rd ed. Wiley-VCH, 2007.
[11] J. W. Norbury and T. C. Slaba, "Space radiation accelerator experiments – The role of neutrons and light ions," *Life Sci. Space Res.*, vol. 3, pp. 90–94, Oct. 2014.
[12] T. Nakamura and L. Heilbronn, *Handbook on Secondary Particle Production and Transport by High-Energy Heavy Ions*. Singapore: World Scientific Publishing Co. Pte. Ltd., 2006.
[13] D. W. Anderson, *Absorption of Ionizing Radiation*. Baltimore: University Park Press, 1984.
[14] J. D. Bowman, W. J. Swiatecki, and C. F. Tsang, "Abrasion and ablation of heavy ions," *Lawrence Berkeley Natl. Lab.*, 1973.
[15] J. Hüfner, K. Schäfer, and B. Schürmann, "Abrasion-ablation in reactions between relativistic heavy ions," *Phys. Rev. C*, vol. 12, no. 6, p. 1888, 1975.
[16] L. F. Oliveira, R. Donangelo, and J. O. Rasmussen, "Abrasion-ablation calculations of large fragment yields from relativistic heavy ion reactions," *Phys. Rev. C*, vol. 19, no. 3, p. 826, 1979.
[17] J. W. Wilson, L. W. Townsend, and F. F. Badavi, "A semiempirical nuclear fragmentation model," *Nucl. Instrum. Methods Phys. Res. Sect. B Beam Interact. Mater. At.*, vol. 18, no. 1–6, pp. 225–231, 1986.
[18] M. Giacomelli, L. Sihver, J. Skvarč, N. Yasuda, and R. Ilić, "Projectilelike fragment emission angles in fragmentation reactions of light heavy ionsin the energy region 200MeV⁄nucleon: Modeling and simulations," *Phys. Rev. C*, vol. 69, no. 6, Jun. 2004.

[19] S. Sriprisan, “An Improved Knockout-Ablation-Coalescence Model for Prediction of Secondary Neutron and Light-ion Production in Cosmic Ray Interactions,” 2008.
[20] T. Kurosawa, T. Nakamura, N. Nakao, T. Shibata, Y. Uwamino, and A. Fukumura, “Spectral measurements of neutrons, protons, deuterons and tritons produced by 100 MeV/nucleon He bombardment,” *Nucl. Instrum. Methods Phys. Res. Sect. Accel. Spectrometers Detect. Assoc. Equip.*, vol. 430, no. 2–3, pp. 400–422, Jul. 1999.
[21] L. Heilbronn *et al.*, “Neutron yields from 435 MeV/nucleon Nb stopping in Nb and 272 MeV/nucleon Nb stopping in Nb and Al,” *Phys. Rev. C*, vol. 58, no. 6, pp. 3451–3461, 1998.
[22] I. Remec, R. Ronningen, and L. Heilbronn, “Benchmarking of neutron production of heavy-ion transport codes,” in *Reactor Dosimetry: 14th International Symposium*, 2012, vol. 9.
[23] R. Madey *et al.*, “Inclusive neutron spectra at 0 from the reactions Pb (Ne, n) X and NaF (Ne, n) X at 390 and 790 MeV per nucleon,” *Phys. Rev. Lett.*, vol. 55, no. 14, p. 1453, 1985.
[24] R. Madey *et al.*, “Inclusive neutron spectra at 0° from Nb-Nb and Au-Au collisions at 800 MeV/nucleon,” *Phys. Rev. C*, vol. 38, no. 1, p. 184, 1988.
[25] L. Heilbronn and et. al., “Production of Neutrons from Interactions of GCR-Like Particles,” *Acta Astronaut.*, vol. 42, no. 1, pp. 363–373, 1998.
[26] L. Heilbronn, “Neutron Yields from Interactions of GCR-Like Beams in Stopping Targets,” *Adv. Space Res.*, vol. 17, no. 2, pp. 269–276, 1996.
[27] ICRP, 2007. The 2007 Recommendations of the International Commission on Radiological Protection. ICRP Publication 103. Ann. ICRP 37 (2-4).
[28] J. T. Goorley *et al.*, “Initial MCNP6 release overview-MCNP6 version 1.0,” *Nucl. Technol.*, vol. 180, pp. 298–315, Dec. 2012.
[29] T. Satoh *et al.*, “Particle and Heavy Ion Transport code System, PHITS, version 2.52,” *J. Nucl. Sci. Technol.*, vol. 50, no. 9, pp. 913–923, Jul. 2013.
[30] F. A. Cucinotta, L. W. Townsend, J. W. Wilson, J. L. Shinn, G. D. Badhwar, and R. R. Dubey, “Light ion components of the galactic cosmic rays: Nuclear interactions and transport theory,” *Adv. Space Res.*, vol. 17, no. 2, pp. 77–86, 1996.
[31] R. B. Norman and S. R. Blattnig, “Validation of nuclear models used in space radiation shielding applications,” *J. Comput. Phys.*, vol. 233, pp. 464–479, Jan. 2013.
[32] M. M. Meier *et al.*, “Differential neutron production cross sections and neutron yields from stopping-length targets for 113-MeV protons,” *Nucl. Sci. Eng.*, vol. 102, no. 3, pp. 310–321, 1989.
[33] Committee on the Evaluation of Radiation Shielding for Space Exploration National Research Council, *Managing Space Radiation Risk in the New Era of Space Exploration*. National Academies Press, 2008.
[34] S. A. Walker, L. W. Townsend, and J. W. Norbury, “Heavy ion contributions to organ dose equivalent for the 1977 galactic cosmic ray spectrum,” *Adv. Space Res.*, vol. 51, no. 9, pp. 1792–1799, May 2013.
[35] T. C. Slaba, A. A. Bahadori, B. D. Reddell, R. C. Singleterry, M. S. Clowdsley, and S. R. Blattnig, “Optimal shielding thickness for galactic cosmic ray environments,” *Life Sci. Space Res.*, vol. 12, pp. 1–15, Feb. 2017.
[36] A. Ferrari, P. R. Sala, A. Fasso, and J. Ranft, “FLUKA: A multi-particle transport code (Program version 2005),” CERN-2005-010 / SLAC-R-773, Oct. 2005.

[37] S. Agostinelli *et al.*, "Geant4—a simulation toolkit," *Nucl. Instrum. Methods Phys. Res. Sect. Accel. Spectrometers Detect. Assoc. Equip.*, vol. 506, no. 3, pp. 250–303, Jul. 2003.
[38] J. W. Wilson, T. C. Slaba, F. F. Badavi, B. D. Reddell, and A. A. Bahadori, "Advances in NASA radiation transport research: 3DHZETRN," *Life Sci. Space Res.*, vol. 2, pp. 6–22, Jul. 2014.
[39] J. W. Wilson, T. C. Slaba, F. F. Badavi, B. D. Reddell, and A. A. Bahadori, "3DHZETRN: Shielded ICRU spherical phantom," *Life Sci. Space Res.*, vol. 4, pp. 46–61, Jan. 2015.
[40] L. G. Crespo, S. P. Kenny, and D. P. Giesy, "Random predictor models for rigorous uncertainty quantification," *Int. J. Uncertain. Quantif.*, vol. 5, no. 5, 2015.
[41] C. La Tessa, M. Sivertz, I.-H. Chiang, D. Lowenstein, and A. Rusek, "Overview of the NASA space radiation laboratory," *Life Sci. Space Res.*, vol. 11, pp. 18–23, Nov. 2016.
[42] "BNL | About NSRL." [Online]. Available: https://www.bnl.gov/nsrl/about.php. [Accessed: 01-May-2017].
[43] J. Alessi, "Electron Beam Ion Source Pre-Injector Project (EBIS): Conceptual Design Report," Collider-Accelerator Department, Brookhaven National Laboratory, BNL-73700-2005-IR, Sep. 2005.
[44] T. Kurosawa *et al.*, "Measurements of secondary neutrons produced from thick targets bombarded by high-energy helium and carbon ions," *Nucl. Sci. Eng.*, vol. 132, no. 1, pp. 30–57, 1999.
[45] D. Satoh *et al.*, "Reevaluation of secondary neutron spectra from thick targets upon heavy-ion bombardment," *Nucl. Instrum. Methods Phys. Res. Sect. Accel. Spectrometers Detect. Assoc. Equip.*, vol. 583, no. 2–3, pp. 507–515, Dec. 2007.
[46] T. Kurosawa *et al.*, "Measurements of Secondary Neutrons Produced from Thick Targets Bombarded by High Energy Neon Ions," *J. Nucl. Sci. Technol.*, vol. 36, no. 1, pp. 41–53, Jan. 1999.
[47] L. Heilbronn *et al.*, "Neutron-Production Yields from 400 MeV/Nucleon Iron Stopping in Carbon, Aluminum, Copper, and Lead Targets," *Nucl. Sci. Eng.*, vol. 169, no. 3, pp. 279–289, 2011.
[48] T. Kurosawa *et al.*, "Neutron yields from thick C, Al, Cu, and Pb targets bombarded by 400 MeV/nucleon Ar, Fe, Xe and 800 MeV/nucleon Si ions," *Phys. Rev. C*, vol. 62, no. 4, p. 44615, Sep. 2000.
[49] L. Heilbronn *et al.*, "Neutron yields from 155 MeV/nucleon carbon and helium stopping in aluminum," *Nucl. Sci. Eng.*, vol. 132, no. 1, pp. 1–15, May 1999.
[50] K. Gunzert-Marx, H. Iwase, D. Schardt, and R. S. Simon, "Secondary beam fragments produced by 200 MeV/u C-12 ions in water and their dose contributions in carbon ion radiotherapy," *New J. Phys.*, vol. 10, no. 7, p. 21, Jul. 2008.
[51] K. Gunzert-Marx, D. Schardt, G. Fehrenbacher, T. Radon, and F. Gutermuth, "Double differential neutron yields from thick targets induced by relativistic carbon and uranium beams," *PoS*, p. 57, 2006.
[52] Y. Iwamoto *et al.*, "Measurement of thick target neutron yields at 0° bombarded with 140, 250 and 350MeV protons," *Nucl. Instrum. Methods Phys. Res. Sect. Accel. Spectrometers Detect. Assoc. Equip.*, vol. 593, no. 3, pp. 298–306, Aug. 2008.

[53] J. W. Wachter, W. R. Burrus, and W. A. Gibson, “Neutron and Proton Spectra from Targets Bombarded by 160-MeV Protons,” *Phys. Rev.*, vol. 161, no. 4, p. 971, 1967.
[54] S. Yonai, T. Kurosawa, H. Iwase, H. Yashima, Y. Uwamino, and T. Nakamura, “Measurement of neutrons from thick Fe target bombarded by protons,” *Nucl. Instrum. Methods Phys. Res. Sect. Accel. Spectrometers Detect. Assoc. Equip.*, vol. 515, no. 3, pp. 733–744, Dec. 2003.
[55] M. M. Meier, C. A. Goulding, G. L. Morgan, and J. L. Ullmann, “Neutron yields from stopping-and near-stopping-length targets for 256-MeV protons,” *Nucl. Sci. Eng.*, vol. 104, no. 4, pp. 339–363, 1990.
[56] M. M. Meier, W. B. Amian, C. A. Goulding, G. L. Morgan, and C. E. Moss, “Neutron yields from stopping-length targets for 256-MeV protons,” *Nucl. Sci. Eng.*, vol. 110, no. 3, pp. 299–301, 1992.
[57] Y. Iwamoto *et al.*, “Measurement of neutron spectra produced in the forward direction from thick graphite, Al, Fe and Pb targets bombarded by 350MeV protons,” *Nucl. Instrum. Methods Phys. Res. Sect. Accel. Spectrometers Detect. Assoc. Equip.*, vol. 562, no. 2, pp. 789–792, Jun. 2006.
[58] J. W. Wachter, W. A. Gibson, and W. R. Burrus, “Neutron and proton spectra from targets bombarded by 450-MeV protons,” *Phys. Rev. C*, vol. 6, no. 5, p. 1496, 1972.
[59] S. Meigo *et al.*, “Measurements of neutron spectra produced from a thick lead target bombarded with 0.5- and 1.5-GeV protons,” *Nucl. Instrum. Methods Phys. Res. A*, vol. 431, pp. 521–530, 1999.
[60] S. Meigo *et al.*, “Measurements of Neutron Spectra Produced from a Thick Tungsten Target Bombarded with 0.5- and 1.5-GeV Protons,” *J. Nucl. Sci. Technol.*, vol. 39, no. sup2, pp. 1252–1255, Aug. 2002.
[61] R. Madey and F. M. Waterman, “High-energy neutrons produced by 740-MeV protons on uranium,” *Phys. Rev. C*, vol. 8, no. 6, p. 2412, 1973.
[62] L. R. Veeser, R. R. Fullwood, A. A. Robba, and E. R. Shunk, “Neutrons produced by 740-MeV protons on uranium,” *Nucl. Instrum. Methods*, vol. 117, no. 2, pp. 509–512, 1974.
[63] P.-E. Tsai, L. Heilbronn, B.-L. Lai, Y.-C. Hsu, and R.-J. Sheu, “Neutron Production from 100 and 230 AMeV He Interactions in Water, PMMA and Iron,” in *2015 IEEE Aerospace Conference*, Big Sky, Montana, 2015.
[64] P.-E. Tsai, “Study of Secondary Particles Produced from Heavy-Ion Interactions,” Doctoral Dissertation, University of Tennessee, Knoxville, Knoxville, TN, USA, 2015.
[65] R. A. Cecil *et al.*, “Neutron angular and energy distributions from 710-MeV alphas stopping in water, carbon, steel, and lead, and 640-MeV alphas stopping in lead,” *Phys. Rev. C*, vol. 21, no. 6, p. 2471, 1980.
[66] J. Alessi, E. Beebe, C. Carlson, D. McCafferty, A. Pikin, and J. Ritter, “A hollow cathode ion source for production of primary ions for the BNL electron beam ion source,” *Rev. Sci. Instrum.*, vol. 85, no. 2, p. 02C107, Feb. 2014.
[67] “BNL | Tandem Van de Graaff | About.” [Online]. Available: https://www.bnl.gov/tandem/about.php. [Accessed: 01-May-2017].
[68] “PSTAR: Stopping Power and Range Tables for Protons,” *National Institute of Standards and Technology (NIST): Physical Measurements Laboratory*. [Online]. Available: http://physics.nist.gov/PhysRefData/Star/Text/PSTAR.html.

[69] L. A. Castellanos, private communication, Jan. 2017.
[70] MATLAB and Statistics Toolbox Release 2016a, The MathWorks, Inc., Natick, Massachusetts, United States.
[71] "Data Sheet for Fast Timing Plastic Scintillator: EJ-228, EJ-230." Eljen Technology, 29-Jan-2016.
[72] "Data Sheet for General Purpose Plastic Scintillator: EJ-200, EJ-204, EJ-208, EJ-212." Eljen Technology.
[73] F. D. Brooks, "Development of organic scintillators," *Nucl. Instrum. Methods*, vol. 162, no. 1–3, pp. 477–505, 1979.
[74] G. T. Wright, "Scintillation decay times of organic crystals," *Proc. Phys. Soc. Sect. B*, vol. 69, no. 3, p. 358, 1956.
[75] F. D. Brooks, "Organic Scintillators," *Prog. Nucl. Phys.*, vol. 5, pp. 252–313, 1956.
[76] R. B. Owen, "The decay times of organic scintillators and their application to the discrimination between particles of differing specific ionization," *IRE Trans. Nucl. Sci.*, vol. 5, no. 3, pp. 198–201, 1958.
[77] J. H. Heltsley *et al.*, "Particle identification via pulse-shape discrimination with a charge-integrating ADC," *Nucl. Instrum. Methods Phys. Res. Sect. Accel. Spectrometers Detect. Assoc. Equip.*, vol. 263, no. 2–3, pp. 441–445, Jan. 1988.
[78] M. Flaska and S. A. Pozzi, "Identification of shielded neutron sources with the liquid scintillator BC-501A using a digital pulse shape discrimination method," *Nucl. Instrum. Methods Phys. Res. Sect. Accel. Spectrometers Detect. Assoc. Equip.*, vol. 577, no. 3, pp. 654–663, Jul. 2007.
[79] S. Marrone *et al.*, "Pulse shape analysis of liquid scintillators for neutron studies," *Nucl. Instrum. Methods Phys. Res. Sect. Accel. Spectrometers Detect. Assoc. Equip.*, vol. 490, no. 1–2, pp. 299–307, Sep. 2002.
[80] "Data Sheet for EJ-301 Liquid Scintillator." Eljen Technology.
[81] V. V. Verbinski, W. R. Burrus, T. A. Love, W. Zobel, N. W. Hill, and R. Textor, "Calibration of an organic scintillator for neutron spectrometry," *Nucl. Instrum. Methods*, vol. 65, no. 1, pp. 8–25, Oct. 1968.
[82] "Scintillators for the Physical Sciences: Data Sheet for NE-213." Nuclear Enterprises.
[83] "Data Sheet for EJ-309 Liquid Scintillator." Eljen Technology.
[84] G. F. Knoll, *Radiation Detection and Measurement*, 4th ed. University of Michigan, Ann Arbor, MI: John Wiley & Sons, Inc., 2010.
[85] R. Fox, "Data Acquisition and Online Analysis at the NSCL," National Superconducting Cyclotron Laboratory, Michigan State University, Dec-2007.
[86] R. Brun and F. Rademakers, "ROOT—an object oriented data analysis framework," *Nucl. Instrum. Methods Phys. Res. Sect. Accel. Spectrometers Detect. Assoc. Equip.*, vol. 389, no. 1, pp. 81–86, 1997.
[87] K. F. Flynn, L. E. Glendenin, E. P. Steinberg, and P. M. Wright, "Pulse height-energy relations for electrons and alpha particles in a liquid scintillator," *Nucl. Instrum. Methods*, vol. 27, no. 1, pp. 13–17, 1964.
[88] D. L. Smith, R. G. Polk, and T. G. Miller, "Measurement of the response of several organic scintillators to electrons, protons and deuterons," *Nucl. Instrum. Methods*, vol. 64, no. 2, pp. 157–166, 1968.

[89] A. A. Naqvi, H. Al-Juwair, and K. Gul, "Energy resolution tests of 125 mm diameter cylindrical NE213 detector using monoenergetic gamma rays," *Nucl. Instrum. Methods Phys. Res. Sect. Accel. Spectrometers Detect. Assoc. Equip.*, vol. 306, no. 1, pp. 267–271, Aug. 1991.
[90] D. Satoh, S. Kunieda, Y. Iwamoto, N. Shigyo, and K. Ishibashi, "Development of SCINFUL-QMD Code to Calculate the Neutron Detection Efficiencies for Liquid Organic Scintillator up to 3 GeV," *J. Nucl. Sci. Technol.*, vol. 39, no. sup2, pp. 657–660, Aug. 2002.
[91] R. A. Cecil, B. D. Anderson, and R. Madey, "Improved predictions of neutron detection efficiency for hydrocarbon scintillators from 1 MeV to about 300 MeV," *Nucl. Instrum. Methods*, vol. 161, pp. 439–447, 1979.
[92] D. Satoh, T. Sato, N. Shigyo, and K. Ishibashi, "SCINFUL-QMD: Monte Carlo Based Computer Code to Calculate Response Function and Detection Efficiency of a Liquid Organic Scintillator for Neutron Energies up to 3 GeV," Japan Atomic Energy Agency, JAEA-Data/Code 2006-023, Nov. 2006.
[93] S. G. Mashnik, K. K. Gudima, R. E. Prael, A. J. Sierk, M. I. Baznat, and N. V. Mokhov, "CEM03. 03 and LAQGSM03. 03 event generators for the MCNP6, MCNPX, and MARS15 transport codes," *ArXiv Prepr. ArXiv08050751*, 2008.
[94] L. A. Castellanos, private communication, May 2017.
[95] H.-C. Wang, private communication, May 2017.
[96] "MCNPX User's Manual Version 2.7.0," Los Alamos National Laboratory, LA-CP-11-00438, Apr. 2011.
[97] N. Borghi, K. Furutaka, and K. Batkov, *mc-tools*. 2016.
[98] L. Heilbronn, private communication, Jan. 2017.
[99] T. Ogawa, private communication, Feb. 2017.
[100] J. Beringer *et al.*, "Review of Particle Physics," *Phys. Rev. D*, vol. 86, no. 1, Jul. 2012.

APPENDICES

APPENDIX I

Table 14. List of logic unit manufacturer and applicable settings.

Manufacturer	Logic Unit	Settings (if applicable)
Wiener	CC-USB CAMAC Controller with USB interface	-
CAEN	HVPS SY5527 (Geco 2020 software)	12 ch (+/-), 24 ch (-), 3 kV, 1 mA, 1.5 W max. Used with OLS, Vetos, CS, NaI.
Bertan	HVPS Model 323	Used with S1, S2.
CAEN	16 Channel CFD Model N843	30 mV. S1=66 mV with Fe beam.
LeCroy	Multiplicity Logic Unit Model 380A	N = 1. Pulse mode. Power source.
-	Majority Coincidence Model C314/NL	Inputs switched to "IN"
LeCroy	Dual Gate Generator Model 222	G1 width = 200 ns G2 width = 0.2 ms
P/S	Quad Gate/Delay Generator Model 794	width = 200 ns
LeCroy	Logic Fan In/Fan Out Model 429	1 (in) x 16 (out)
LeCroy	Octal Discriminator Model 623	-
LeCroy	Octal Discriminator Model 623B	-
Joerger	Scaler Model S12	-
-	Japanese Module 6 Ch. PSD	-
LeCroy	8 Channel TDC Model 2228A	Common start
LeCroy	12 Channel ADC Model 2249A	Gated
LeCroy	12 Channel ADC Model 2249W	Gated
LeCroy	12 Channel ADC Model 2249W	Gated
BNL	Splitters	-
BNL	Delays	Varied. 16, 50, 100 ns increments.

Table 15. Button source information from BNL.

Source	Date	Test Date	Activity (μCi)	Half-Life (year)	λ (1/year)	A at Test (μCi)	C. Edge E. (keV)	Source Type
Cs-137	Apr, 2007	Mar, 2016	5.0	30.2	0.02295	4.0746	477.30	Beta/ gamma
Co-60	Mar, 2007	Mar, 2016	1.0	5.27	0.13153	0.3061	~1039.31	gamma

Table 16. Adjusted flight paths for high-energy neutrons originating from 400 or 800 AMeV iron, or 400 AMeV helium beams incident on aluminum.

Detector (angle)	Flight paths (cm)								
	20 g/cm^2 Al			40 g/cm^2 Al			60 g/cm^2 Al		
	400 AMeV Fe	800 AMeV Fe	400 AMeV He	400 AMeV Fe	800 AMeV Fe	400 AMeV He	400 AMeV Fe	800 AMeV Fe	400 AMeV He
10°	310.36	309.66	308.39	313.58	312.75	310.22	315.77	315.40	312.82
30°	310.60	309.98	308.87	313.44	312.71	310.47	315.38	315.05	312.77
45°	310.05	309.54	308.63	312.38	311.78	309.94	313.98	313.71	311.83
60°	259.59	259.22	258.58	261.26	260.83	259.51	262.43	262.23	260.87
80°	258.22	258.09	257.86	258.85	258.68	258.19	259.30	259.22	258.70
135°	205.38	205.88	206.78	203.11	203.69	205.48	201.57	201.83	203.64
80% width (cm)	1.28	2.71	5.27	2.16	3.83	8.98	5.11	5.86	11.1

APPENDIX II

Comparisons of experimental double differential thick-target neutron yield data with PHITS and MCNP room geometry simulations

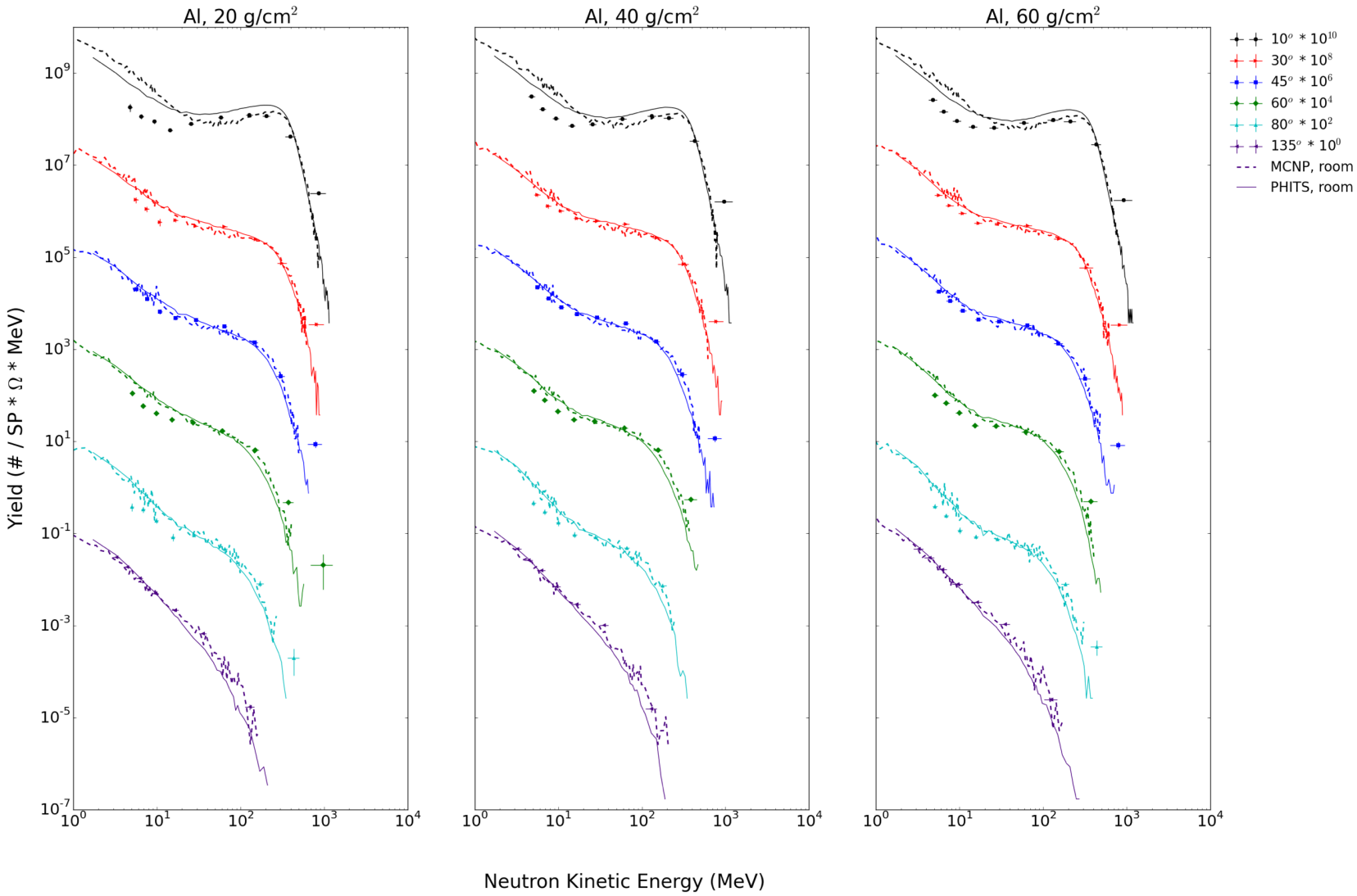


Figure 47. DDTT neutron yields for 400 AMeV iron projectiles on aluminum; PHITS and MCNP room geometries.

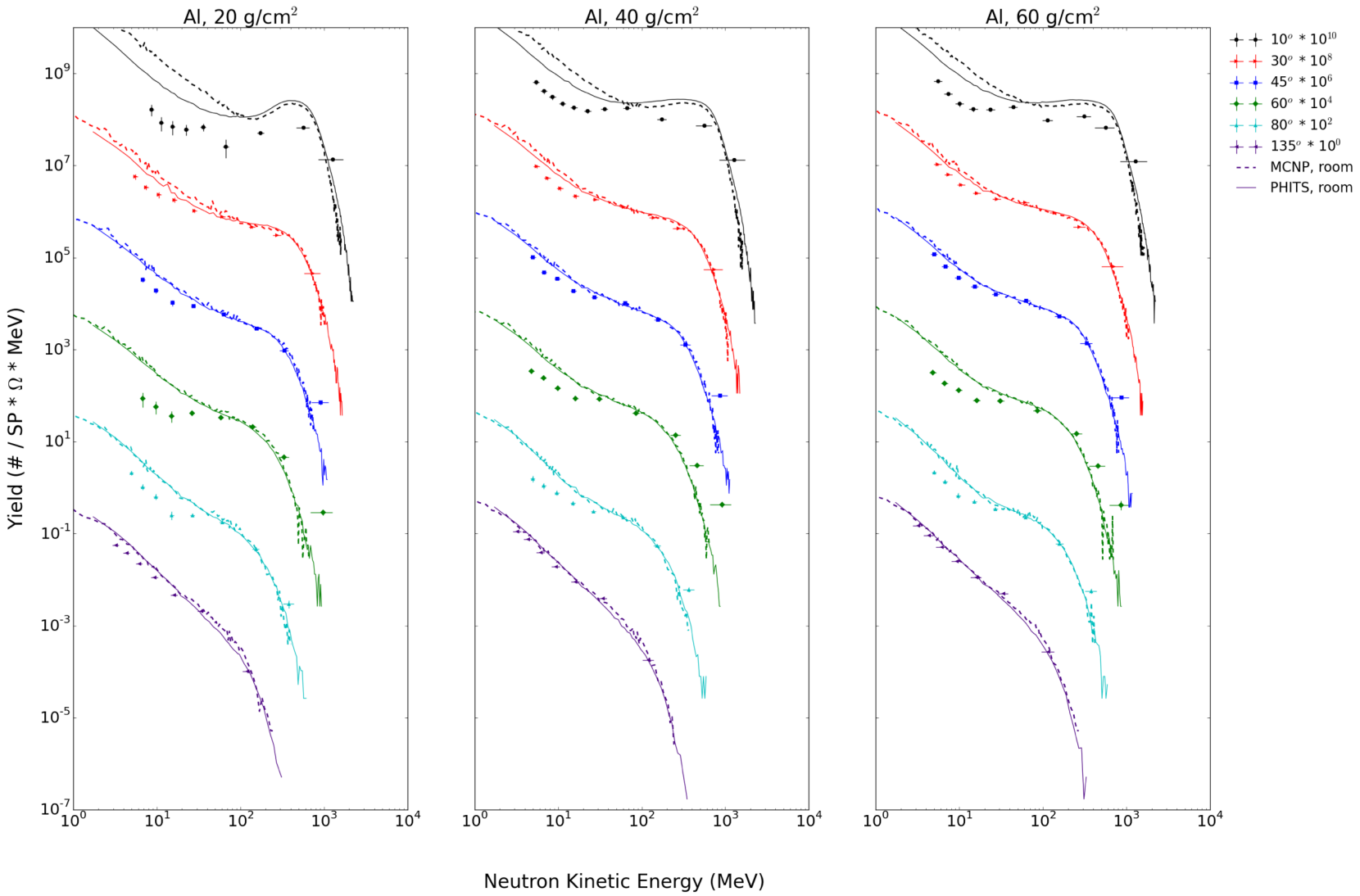


Figure 48. DDTT neutron yields for 800 AMeV iron projectiles on aluminum; PHITS and MCNP room geometries.

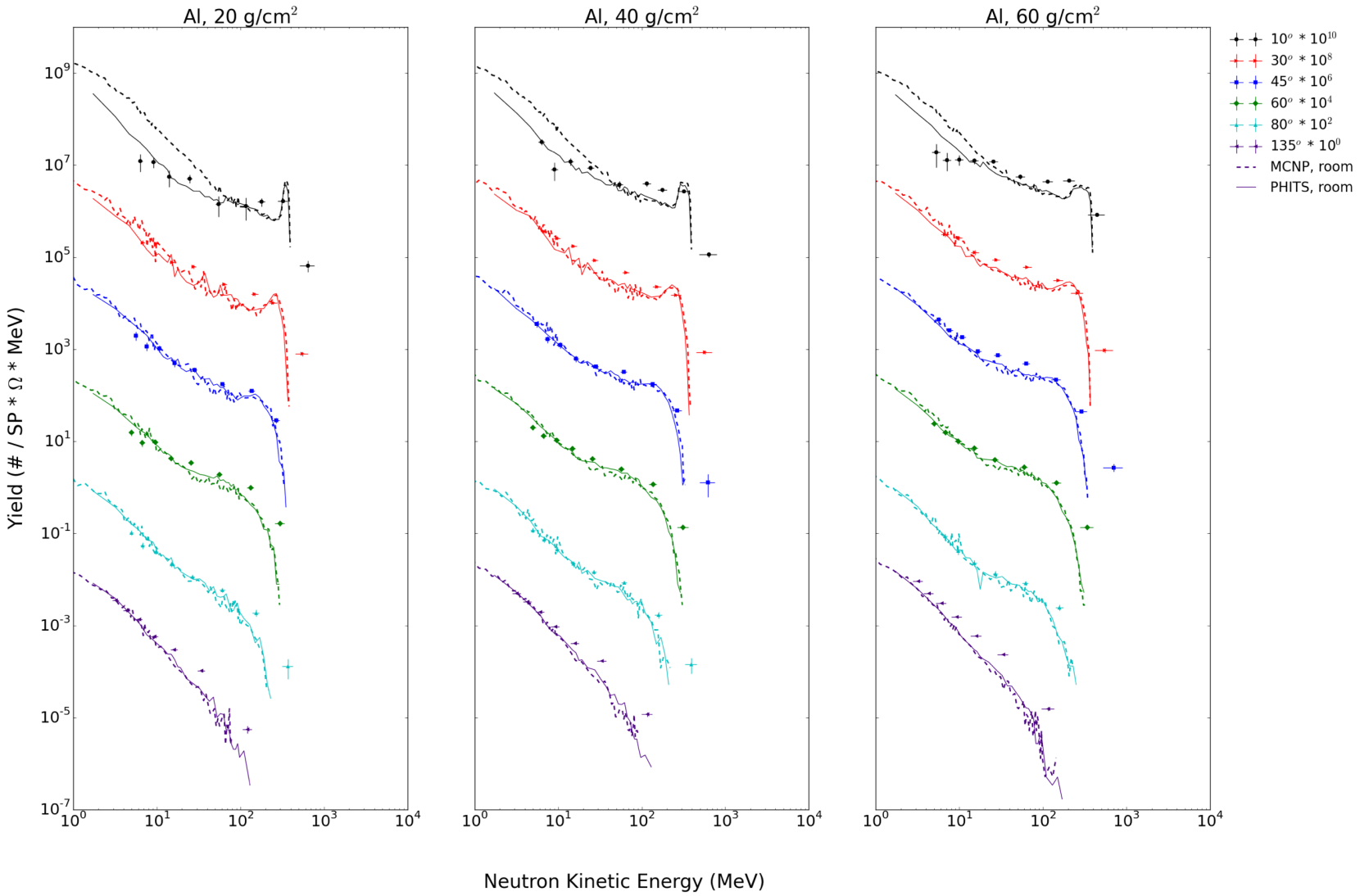


Figure 49. DDTT neutron yields for 400 MeV proton projectiles on aluminum; PHITS and MCNP room geometries.

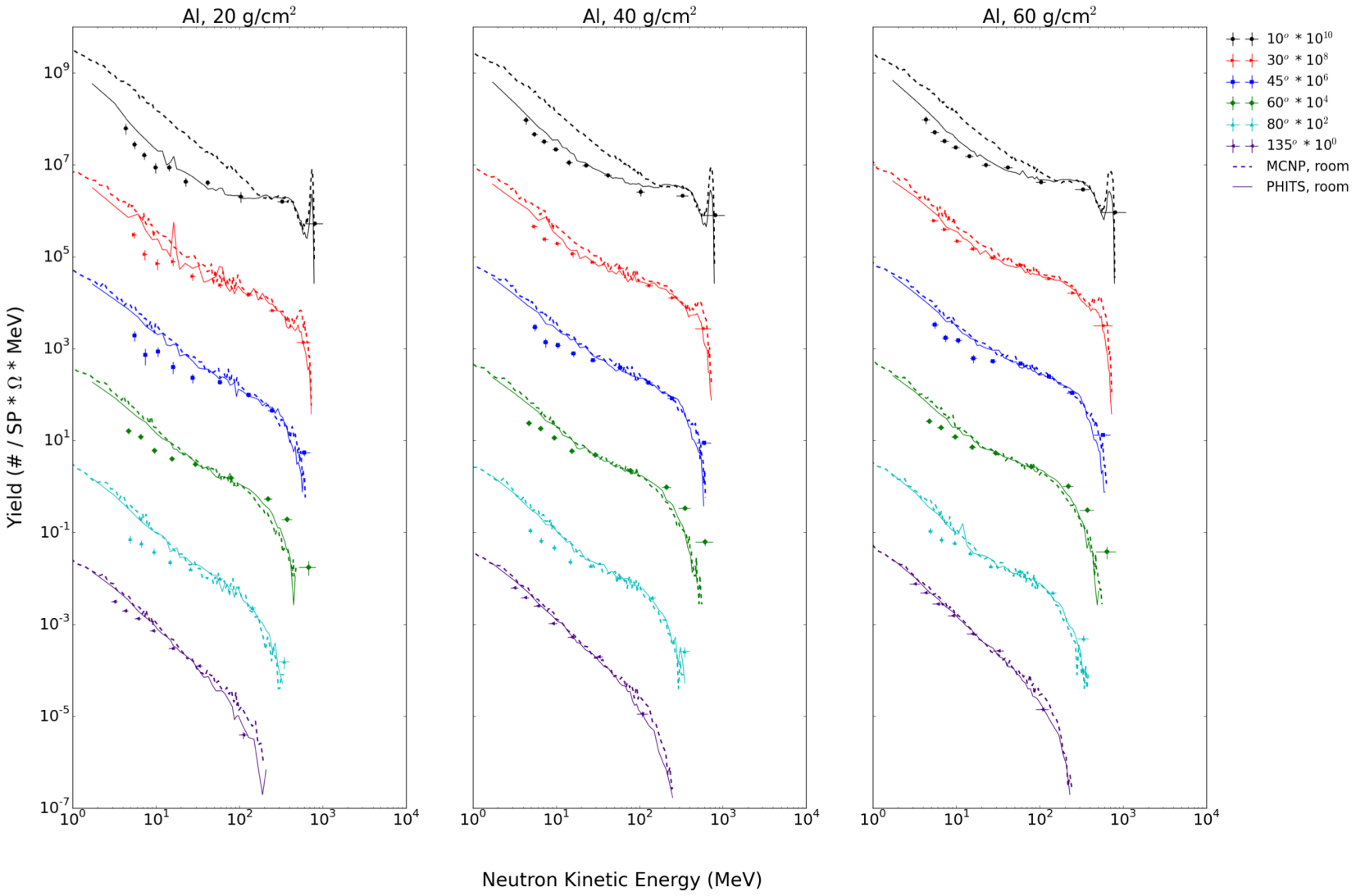


Figure 50. DDTT neutron yields for 800 MeV proton projectiles on aluminum; PHITS and MCNP room geometries.

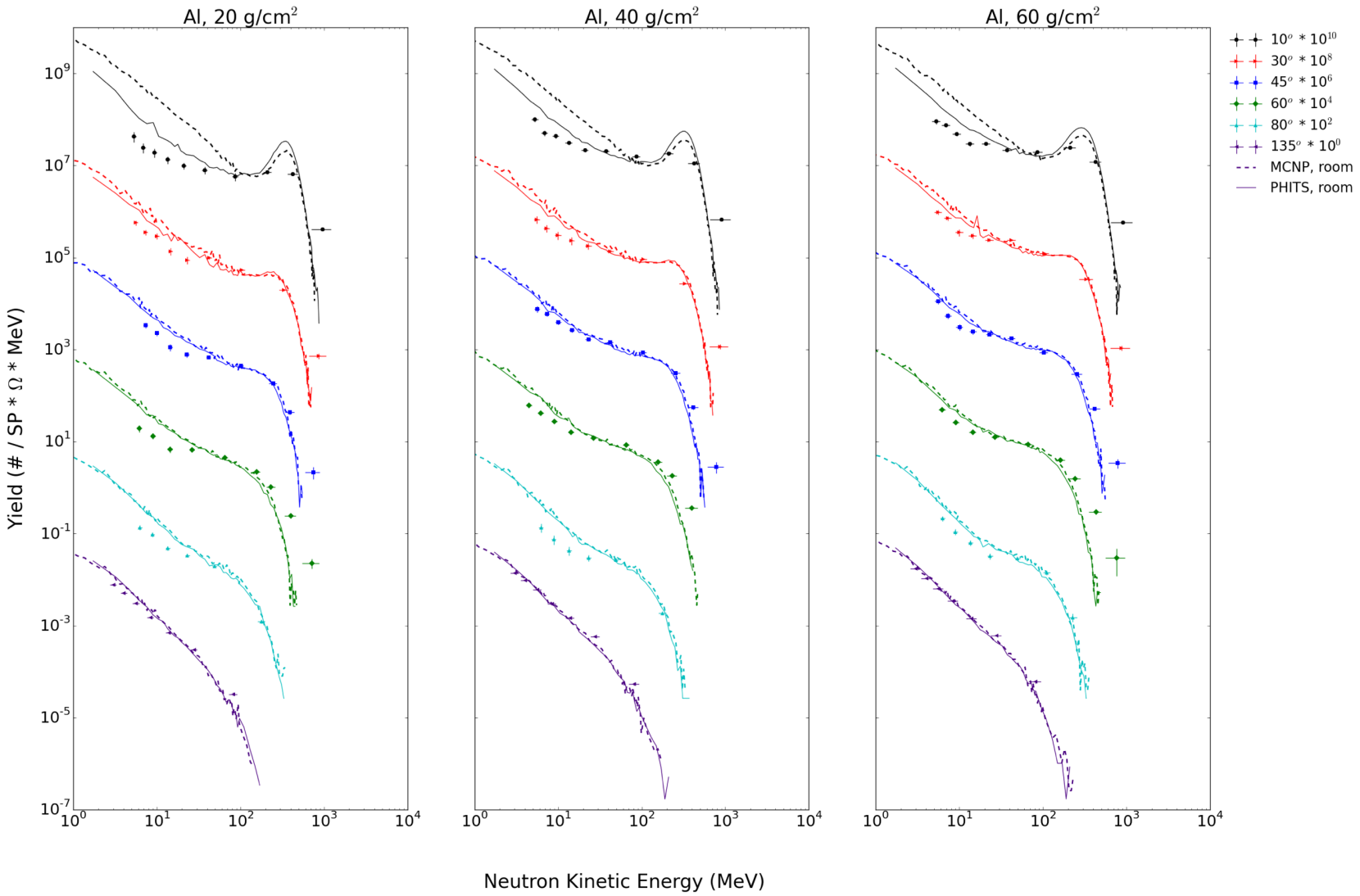


Figure 51. DDTT neutron yields for 400 AMeV helium projectiles on aluminum; PHITS and MCNP room geometries.

Comparisons of experimental double differential thick-target neutron yield data with PHITS ring geometry simulations and MCNP room geometry simulations with the neutron directionality correction

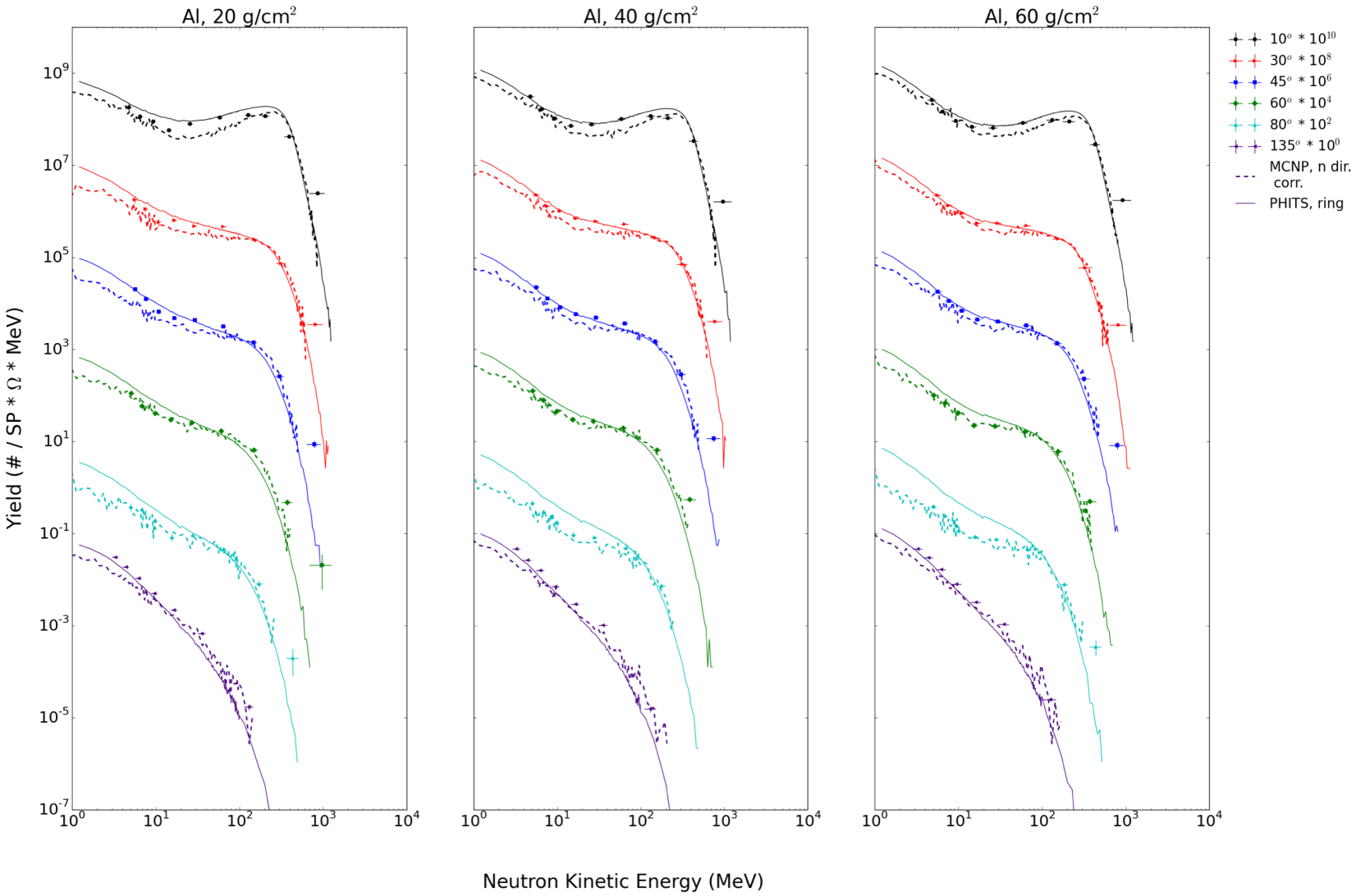


Figure 52. DDTT neutron yields for 400 AMeV iron projectiles on aluminum; PHITS ring geometry and MCNP neutron directionality correction.

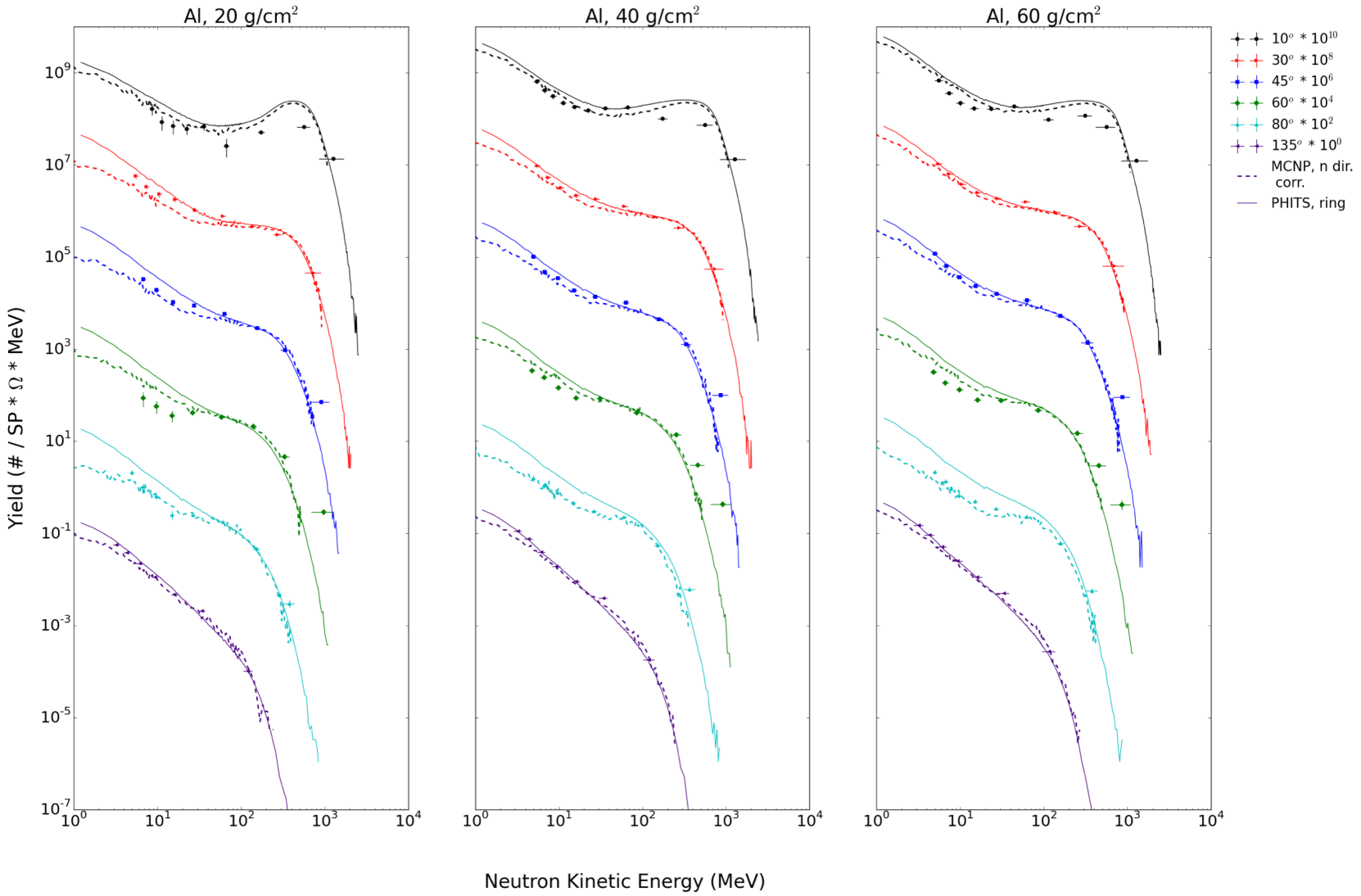


Figure 53. DDTT neutron yields for 800 AMeV iron projectiles on aluminum; PHITS ring geometry and MCNP neutron directionality correction.

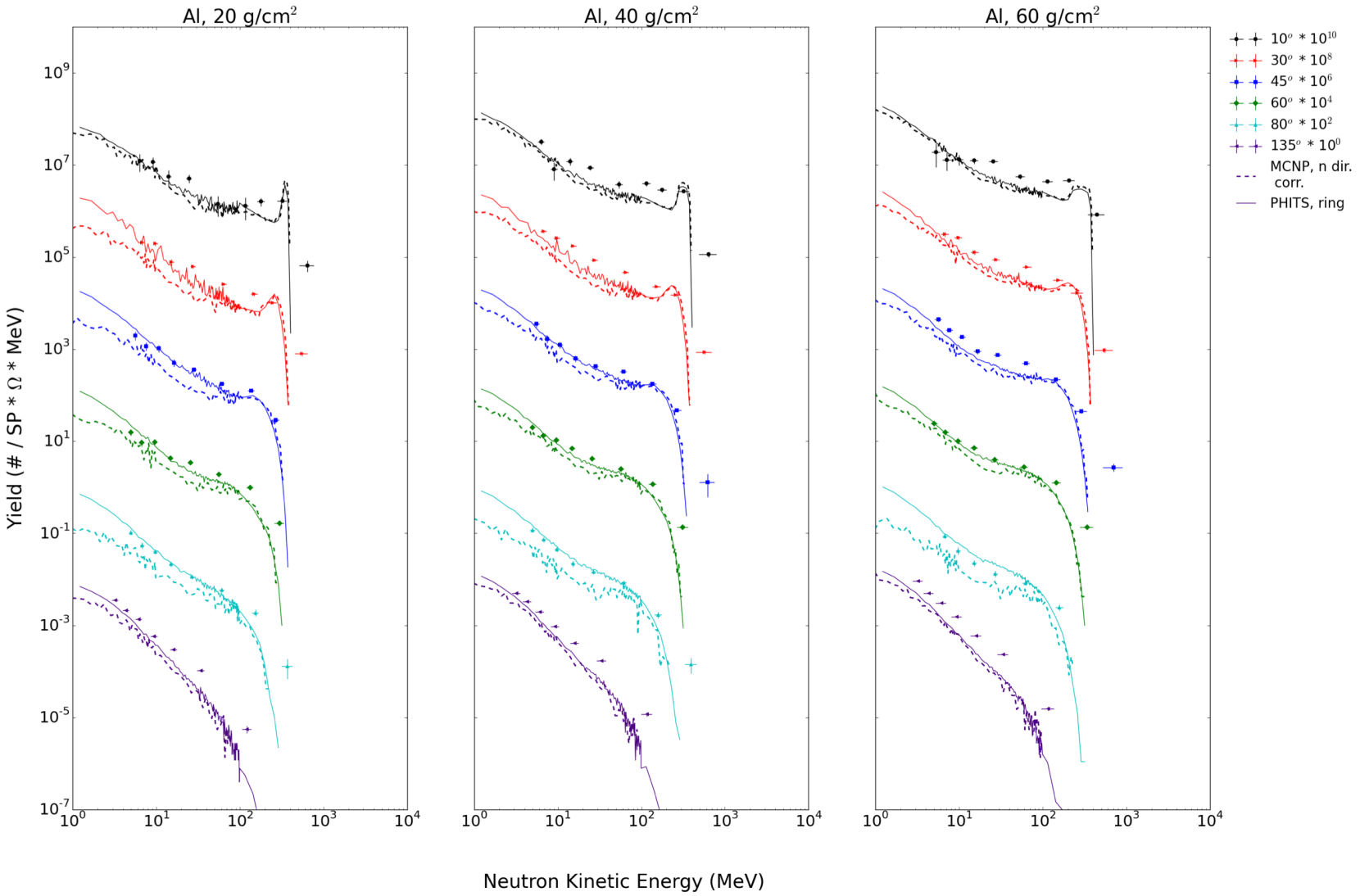


Figure 54. DDTT neutron yields for 400 MeV proton projectiles on aluminum; PHITS ring geometry and MCNP neutron directionality correction.

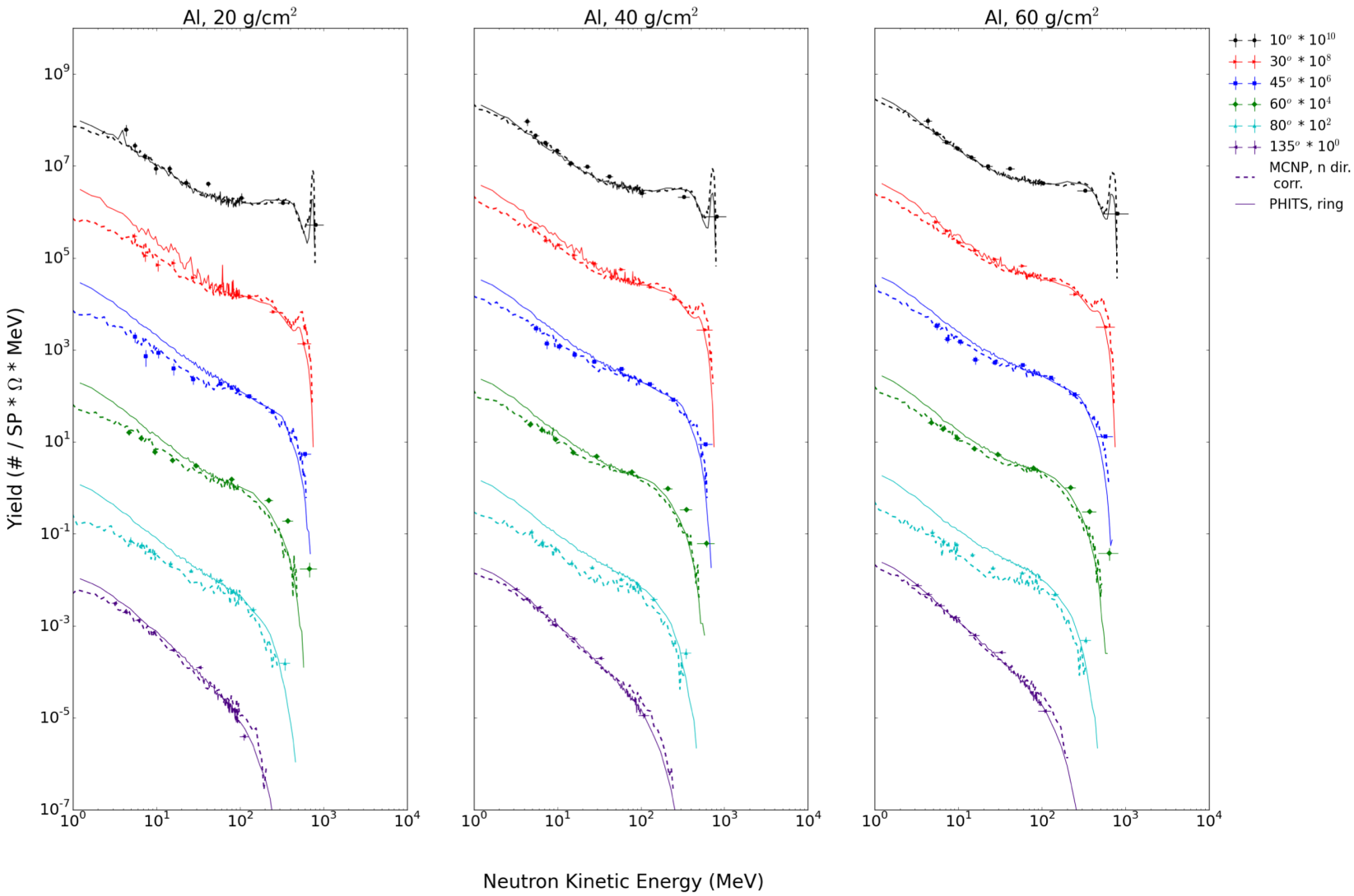


Figure 55. DDTT neutron yields for 800 MeV proton projectiles on aluminum; PHITS ring geometry and MCNP neutron directionality correction.

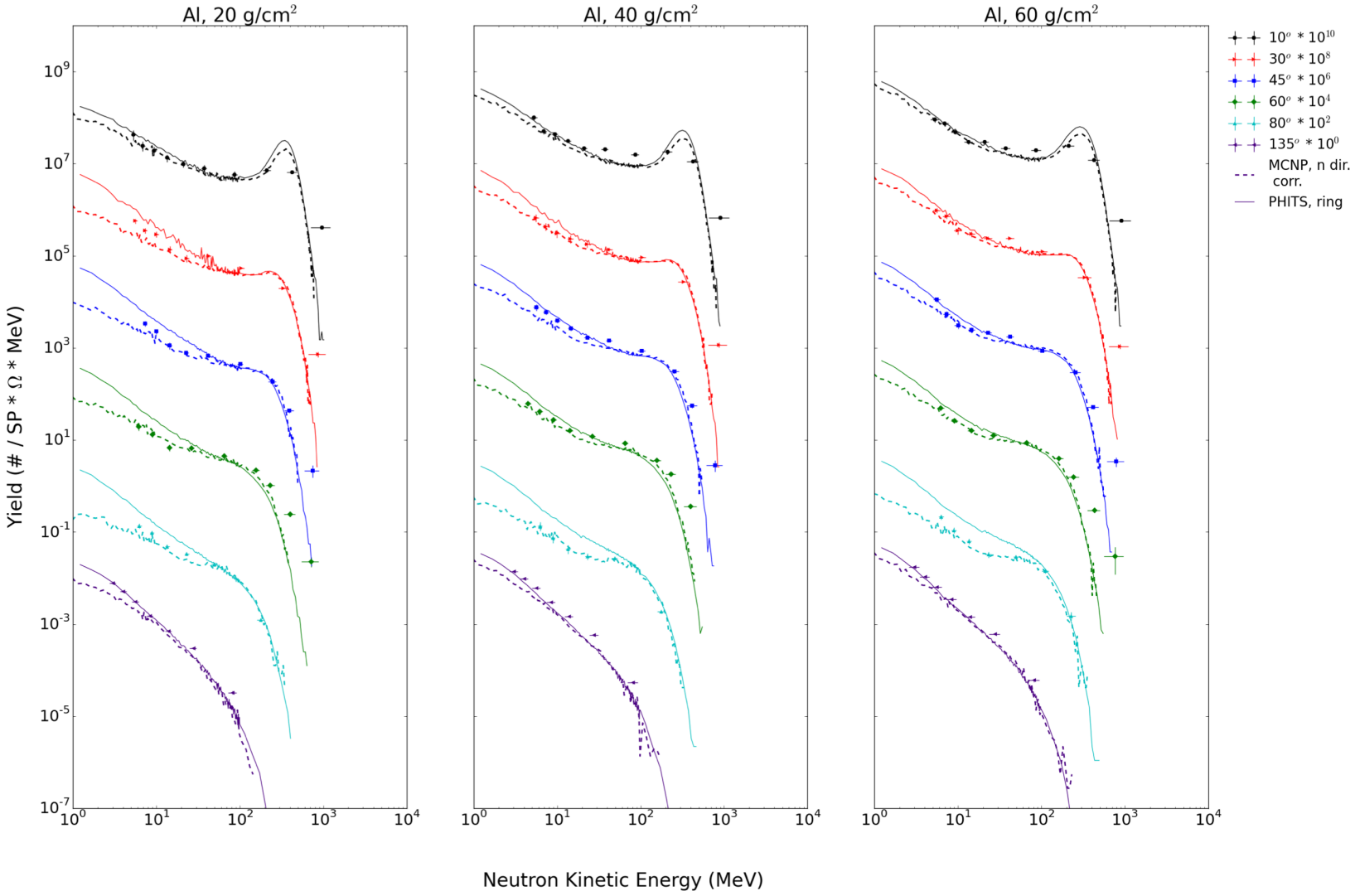


Figure 56. DDTT neutron yields for 400 AMeV helium projectiles on aluminum; PHITS ring geometry and MCNP neutron directionality correction.

APPENDIX III

Comparisons of experimental double differential thick-target neutron yield data with PHITS room and ring geometry simulations

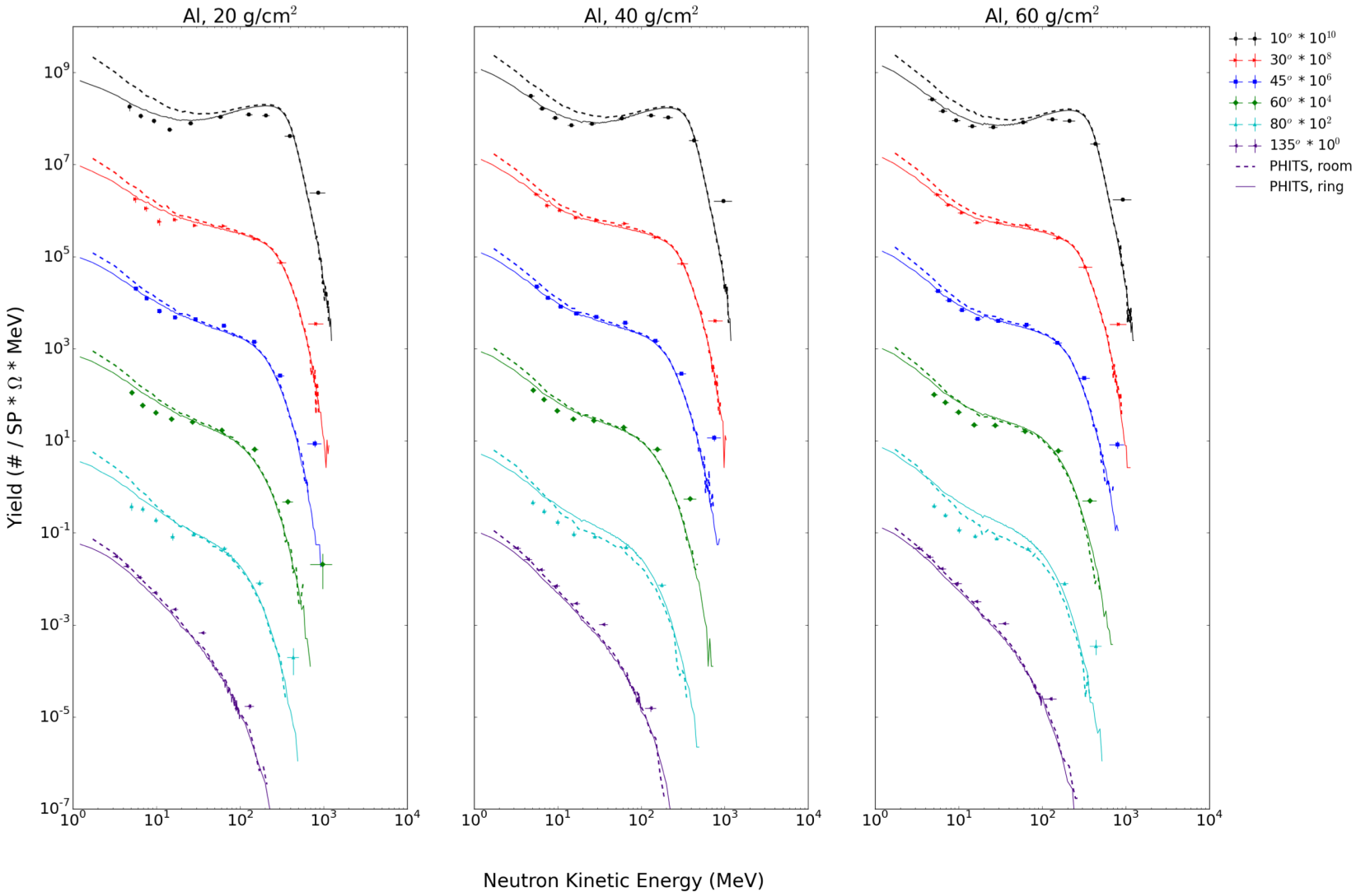


Figure 57. DDTT neutron yields for 400 AMeV iron projectiles on aluminum; PHITS room and ring geometries.

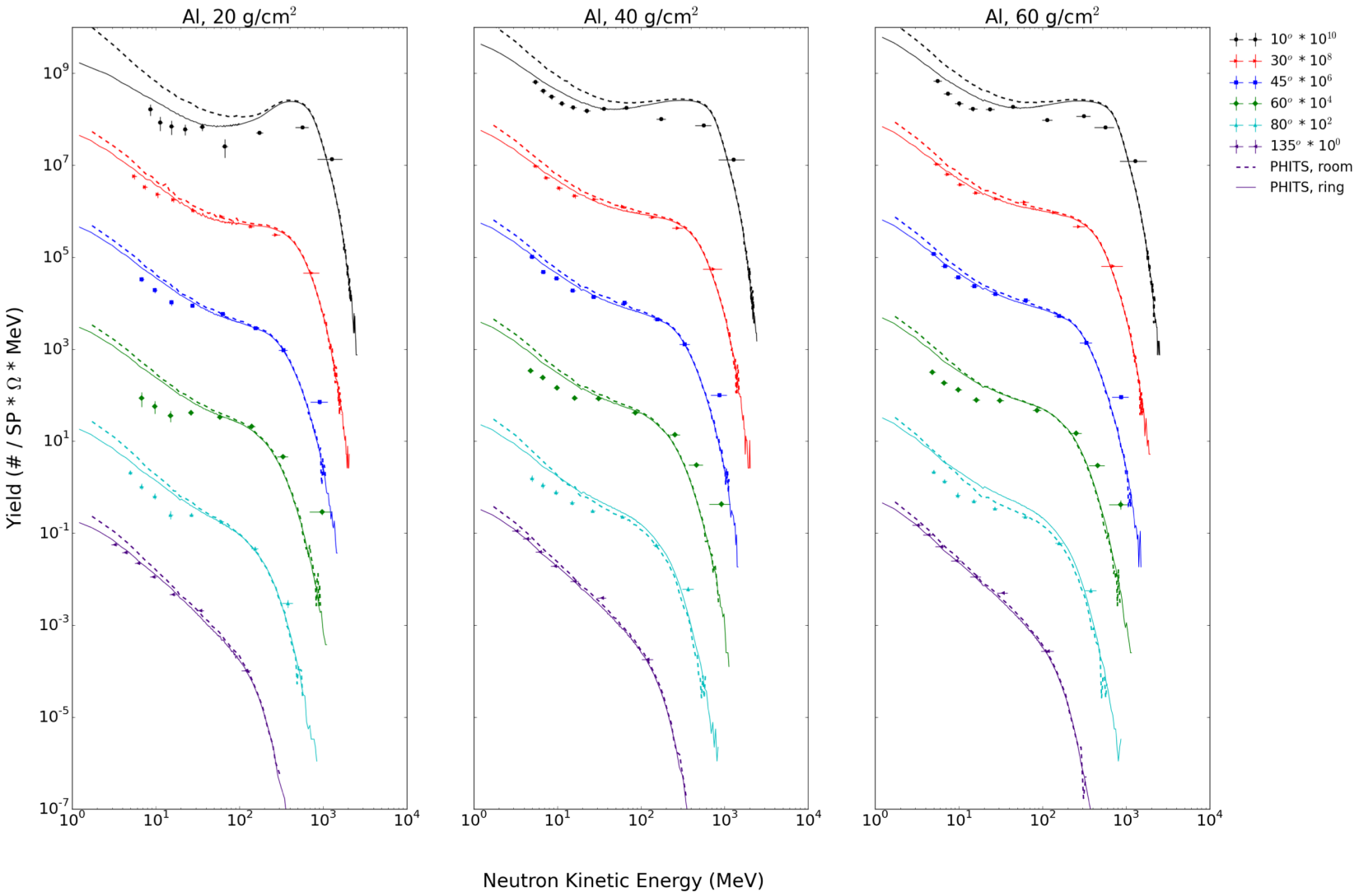


Figure 58. DDTT neutron yields for 800 AMeV iron projectiles on aluminum; PHITS room and ring geometries.

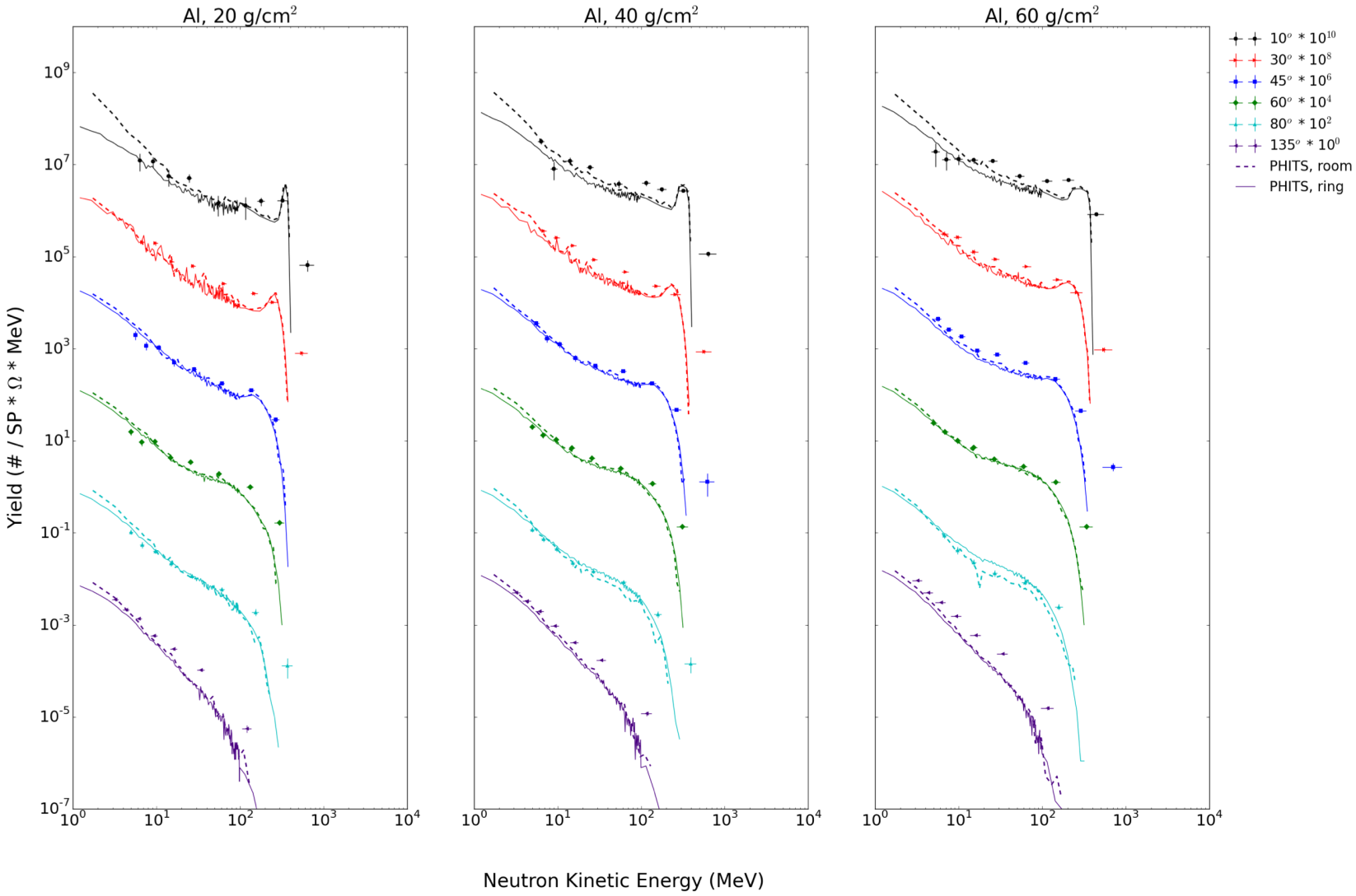


Figure 59. DDTT neutron yields for 400 MeV proton projectiles on aluminum; PHITS room and ring geometries.

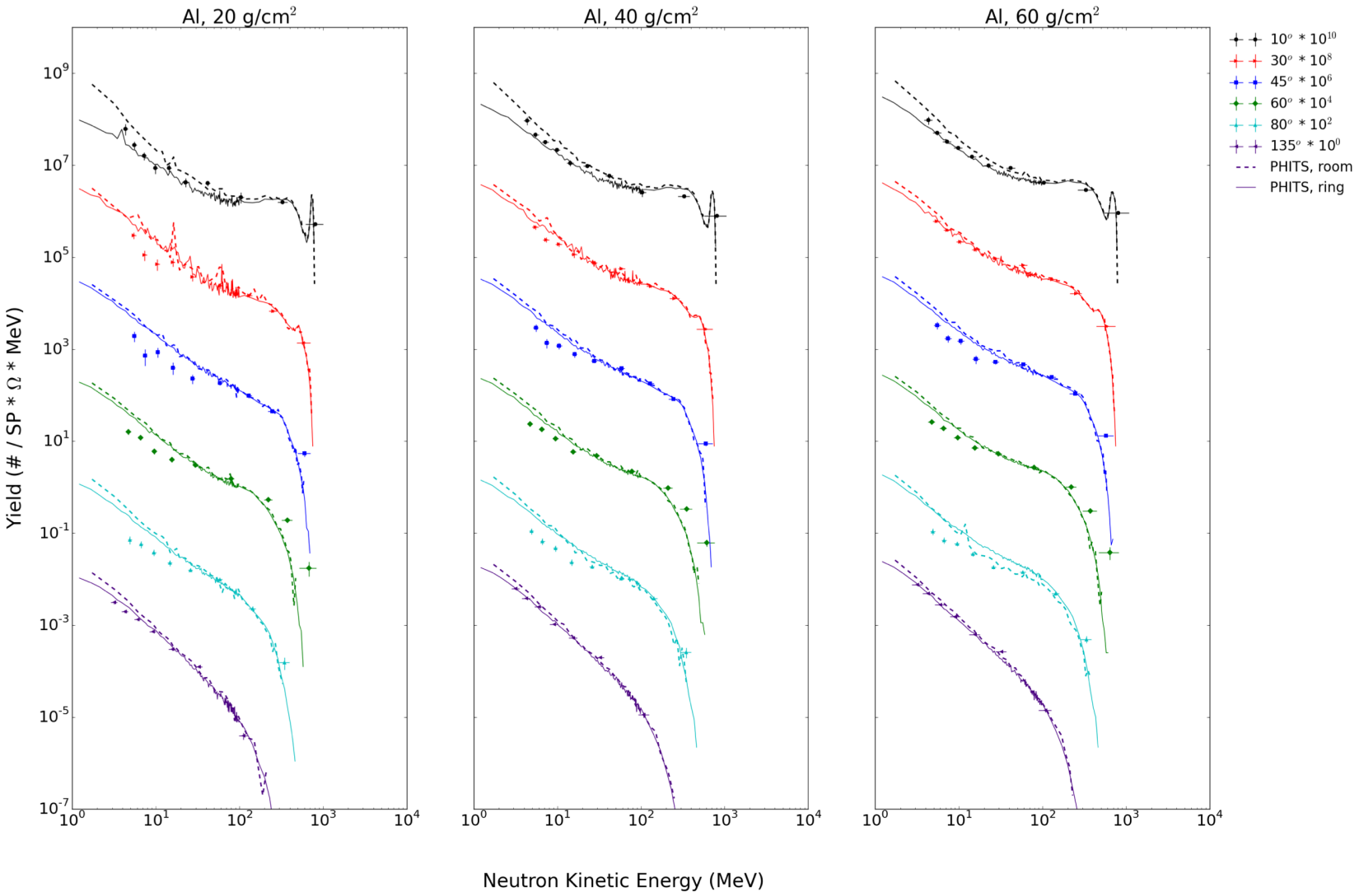


Figure 60. DDTT neutron yields for 800 MeV proton projectiles on aluminum; PHITS room and ring geometries.

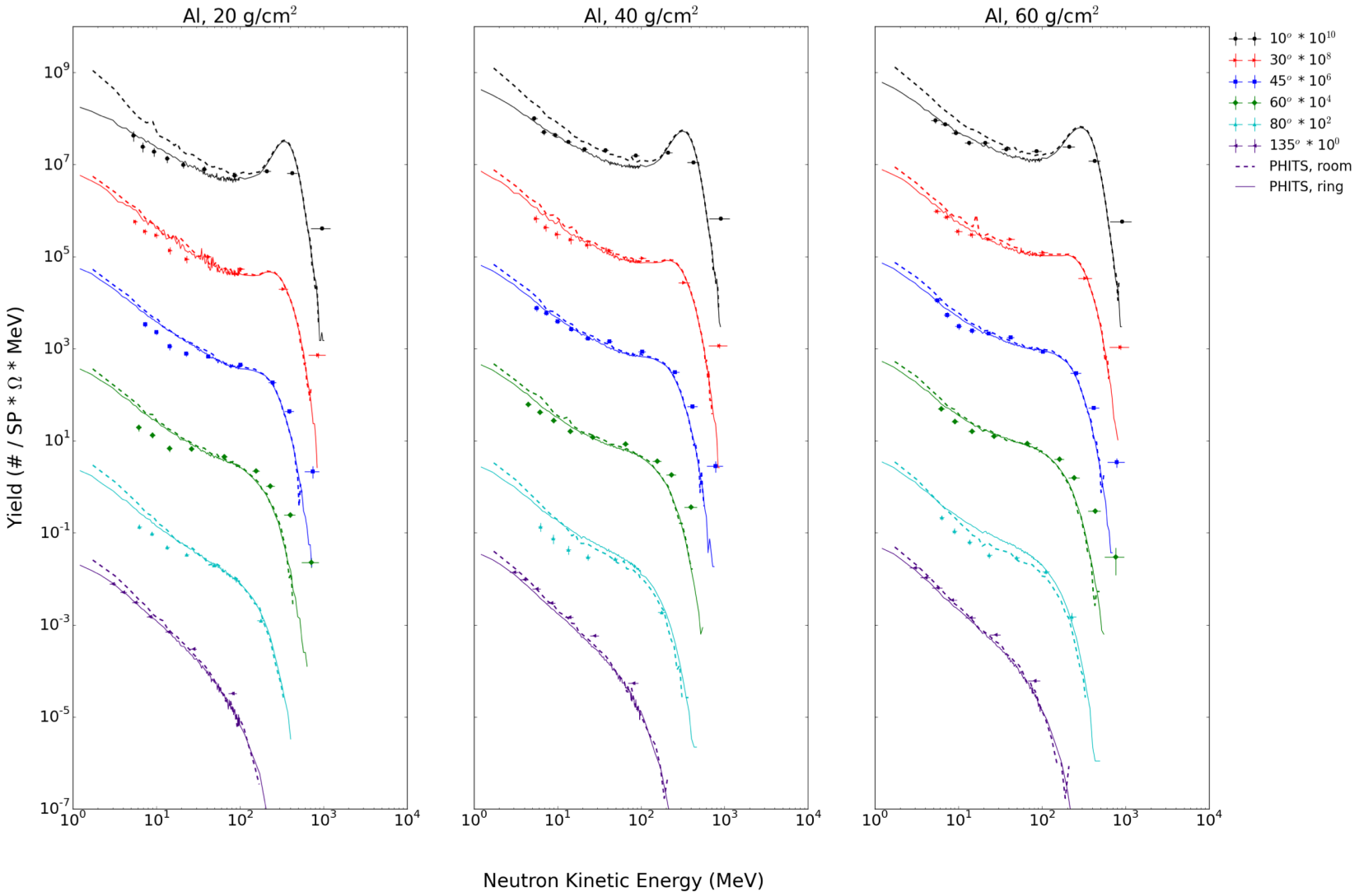


Figure 61. DDTT neutron yields for 400 AMeV helium projectiles on aluminum; PHITS room and ring geometries.

Comparisons of experimental double differential thick-target neutron yield data with MCNP room geometry simulations, with and without the neutron directionality correction

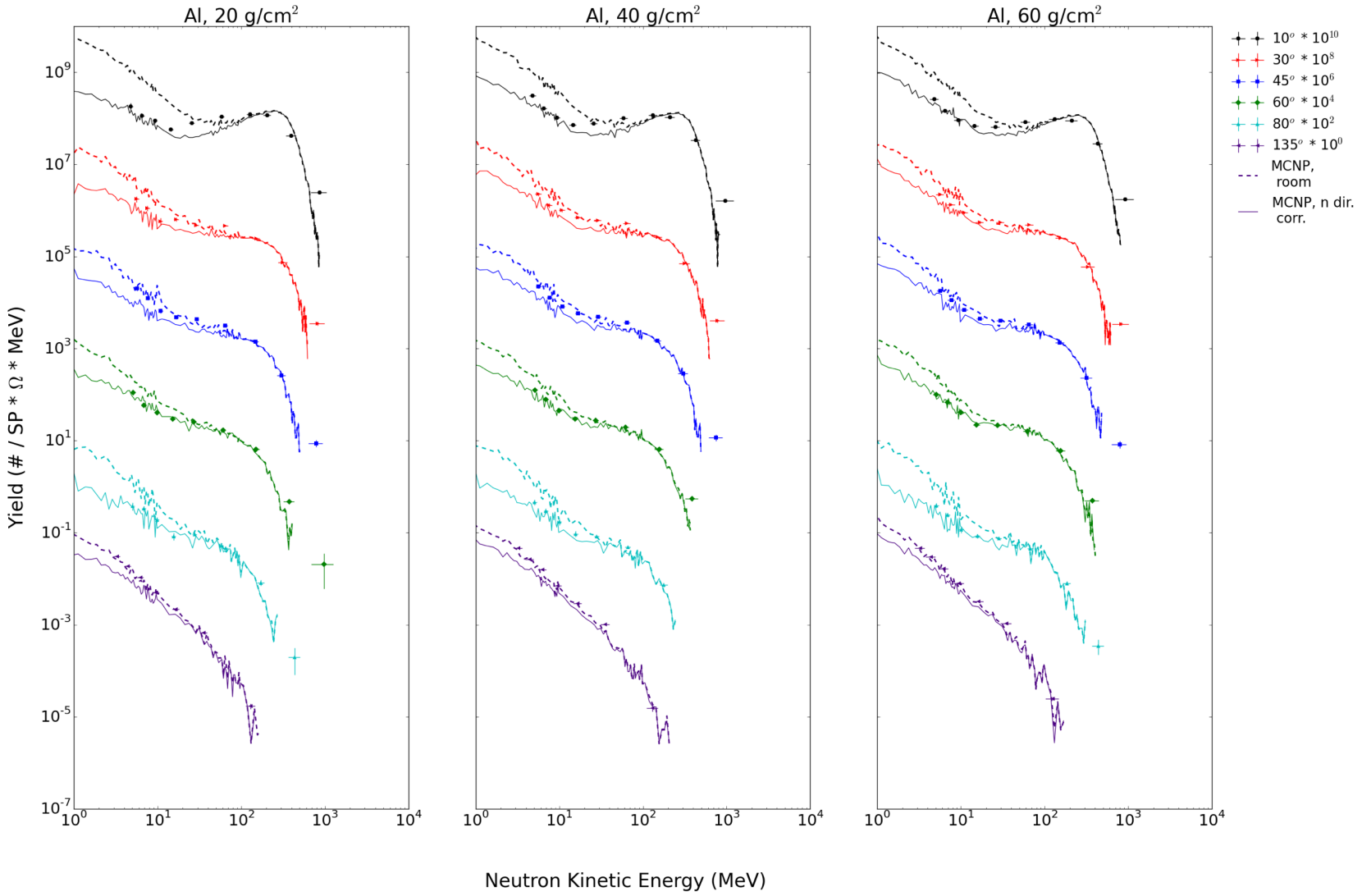


Figure 62. DDTT neutron yields for 400 AMeV iron projectiles on aluminum; MCNP room geometry and neutron directionality correction.

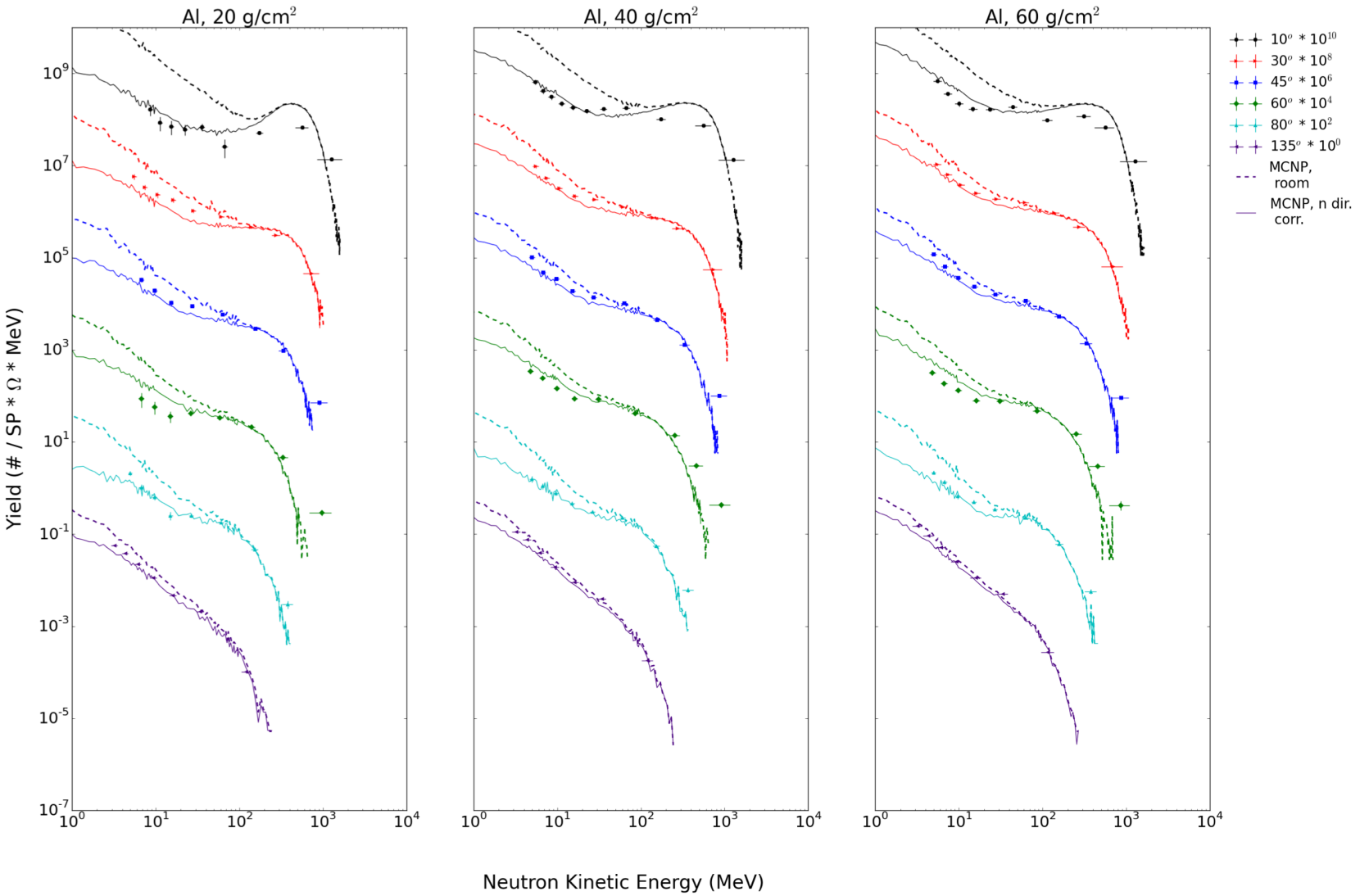


Figure 63. DDTT neutron yields for 800 AMeV iron projectiles on aluminum; MCNP room geometry and neutron directionality correction.

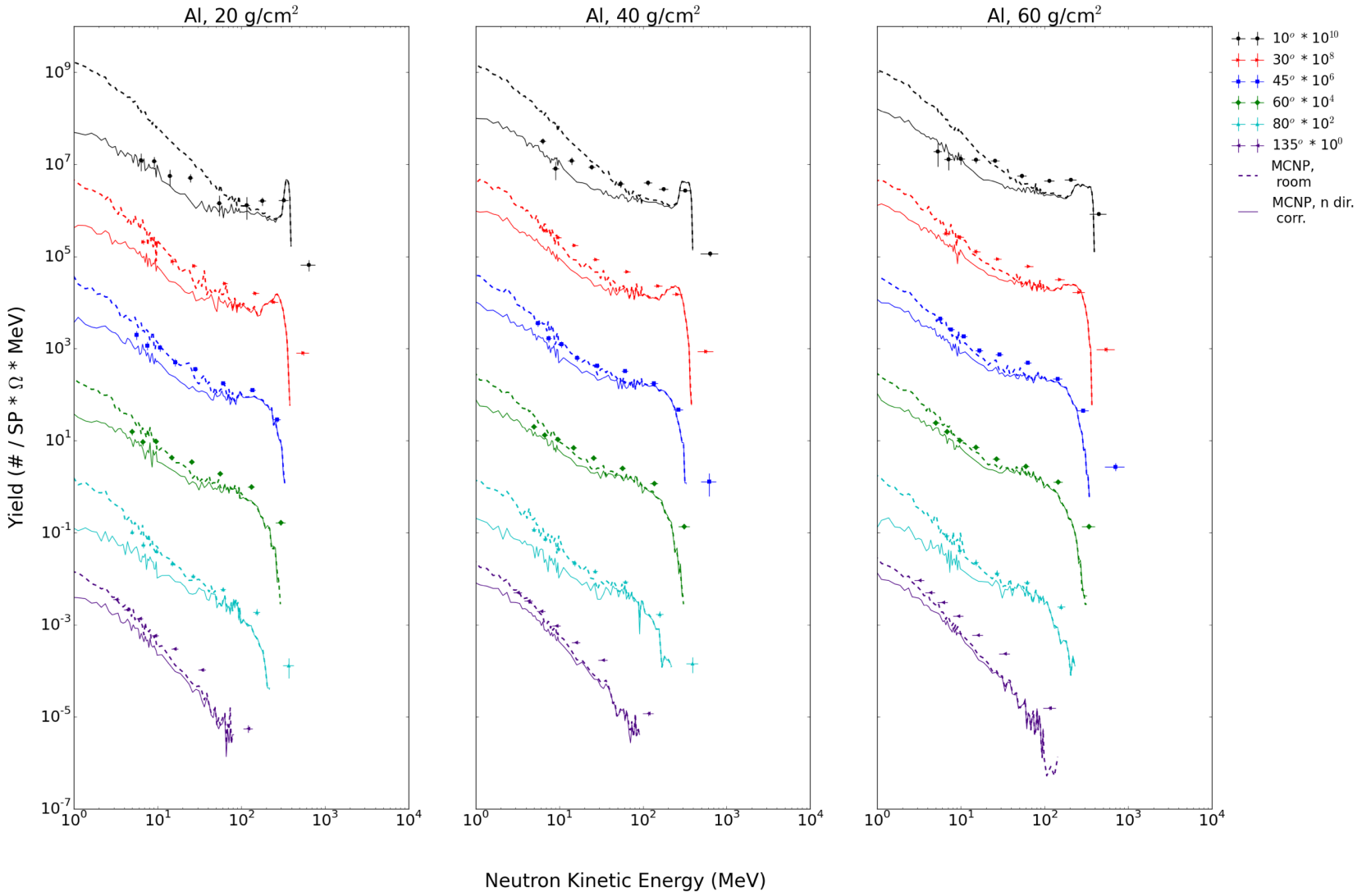


Figure 64. DDTT neutron yields for 400 MeV proton projectiles on aluminum; MCNP room geometry and neutron directionality correction.

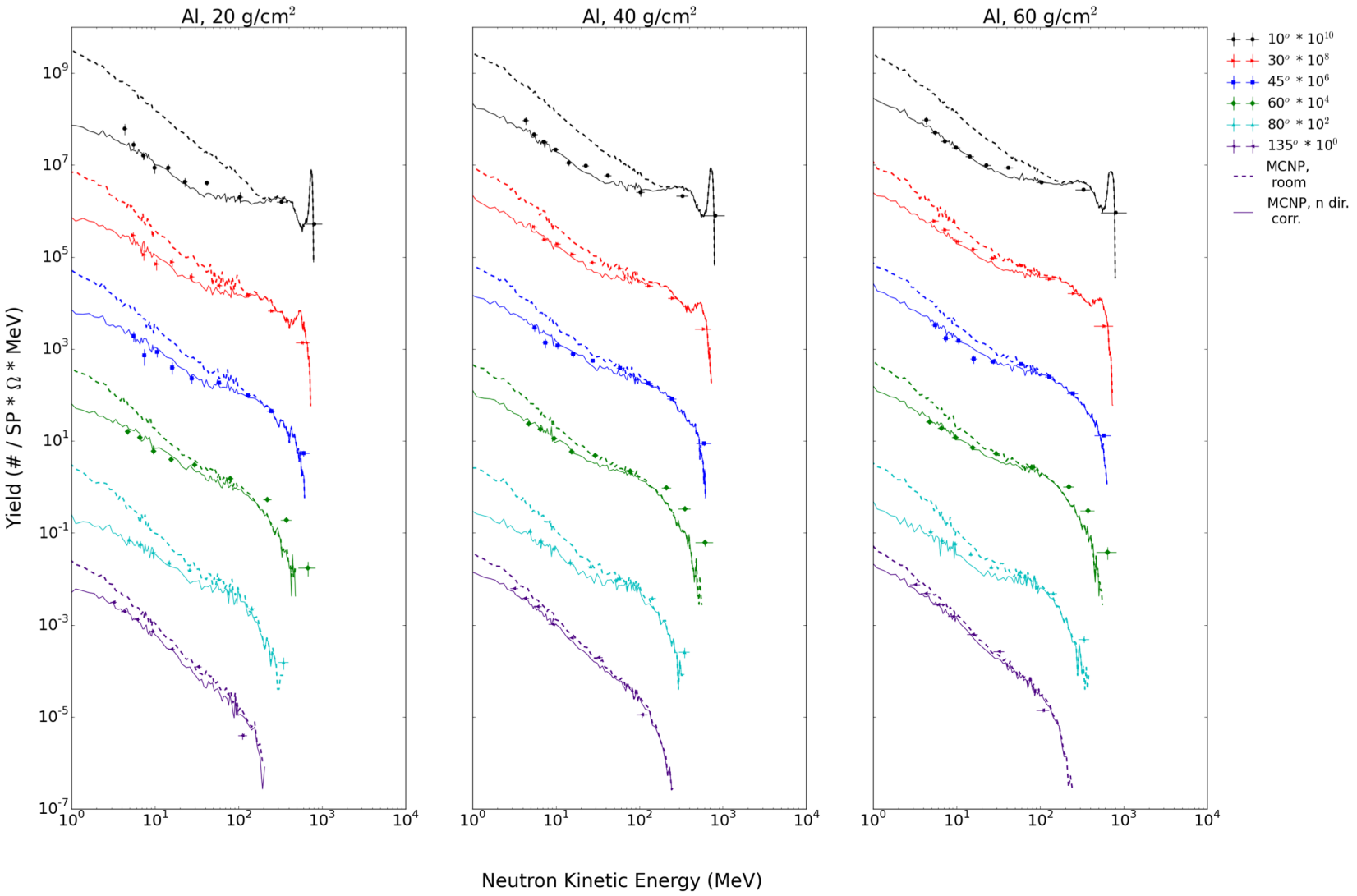


Figure 65. DDTT neutron yields for 800 MeV proton projectiles on aluminum; MCNP room geometry and neutron directionality correction.

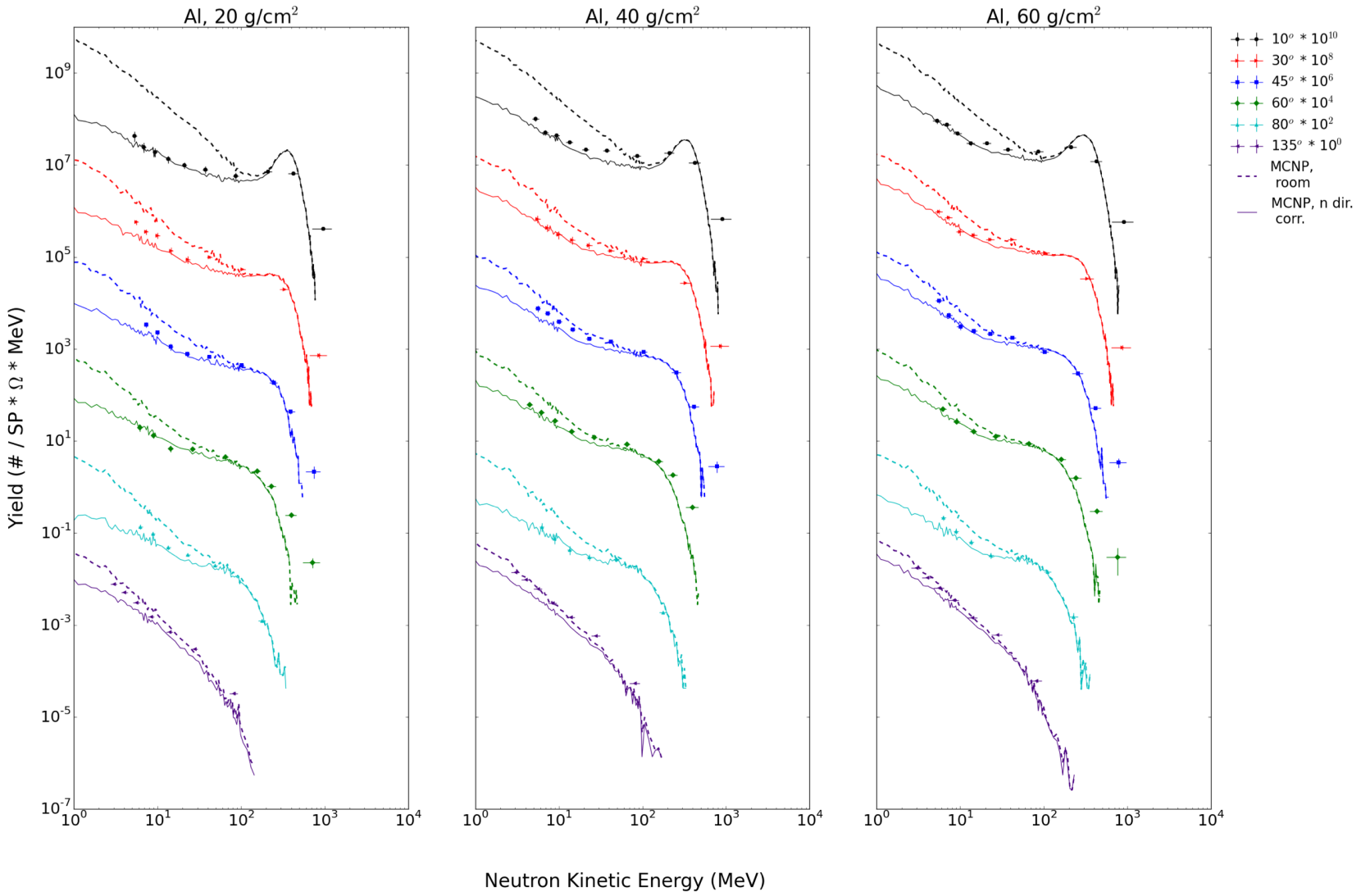


Figure 66. DDTT neutron yields for 400 AMeV helium projectiles on aluminum; MCNP room geometry and neutron directionality correction.

VITA

Natalie Ann McGirl grew up in Chattanooga, Tennessee before moving to Knoxville to attend the University of Tennessee. She graduated with her B.S. in Nuclear Engineering with an Honors Radiological Engineering Concentration in 2013 and her M.S. in Nuclear Engineering in 2014. During her academic career, Natalie worked as an intern for a national laboratory, the federal government, and the nuclear power industry. Since 2015, she has accumulated 318 hours of beam time experience at Brookhaven National Laboratory's NASA Space Radiation Laboratory.